Observatório Nacional

Divisão de Programas
de Pós Graduação

ORBITAL RECORDS SHAPED BY DEPOSITIONAL ARCHITECTURE IN A CONTINENTAL MARGIN: CYCLOSTRATIGRAPHIC–SEISMIC ANALYSIS OF THE MIOCENE ALBACORA OILFIELD (CAMPOS BASIN, BRAZIL)

Mariana Aragão Fernandes

Dissertation presented to the Graduate Program in Geophysics at the National Observatory, as part of the requirements for obtaining the title of Master in Geophysics.

Advisor: Dr. Daniel Ribeiro Franco (ON/MCTI)

Co-advisors: Dr. Natália Braun dos Santos (ON/MCTI) and Dr. Mingsong Li (Peking University)

Rio de Janeiro
May 2026

"ORBITAL RECORDS SHAPED BY DEPOSITIONAL ARCHITECTURE IN A CONTINENTAL MARGIN: CYCLOSTRATIGRAPHIC–SEISMIC ANALYSIS OF THE MIOCENE ALBACORA OILFIELD (CAMPOS BASIN, BRAZIL)"

Mariana Aragão Fernandes

DISSERTAÇÃO SUBMETIDA AO CORPO DOCENTE DO PROGRAMA DE PÓS-GRADUAÇÃO EM GEOFÍSICA DO OBSERVATÓRIO NACIONAL COMO PARTE DOS REQUISITOS NECESSÁRIOS PARA A OBTENÇÃO DO GRAU DE MESTRA EM GEOFÍSICA.

Aprovada por:

Dr. Daniel Ribeiro Franco - (ON) - (Orientador)

Dr. José Alejandro Moreno Alfonzo - (ON)

Dra. Jóice Cagliari - (Universidade do Vale do Rio dos Sinos)

RIO DE JANEIRO – BRASIL

27 DE MAIO DE 2026

Acknowledgments

First and foremost, I thank God, my Father and Creator, whose love is so great that I cannot fully express it in words. During the most difficult moments of this journey, He was with me. I was able to move forward with confidence throughout this entire path because God's hand sustained me. Thank you, Lord.

To my advisor, Daniel Franco, for believing in me from the very beginning. For his patience in teaching and shaping his students, even amid so many responsibilities; for sharing his knowledge, ideas, and experience; and for his sensitivity in understanding the needs of others, always offering support whenever possible. I am deeply grateful for the opportunity to have developed this work under his supervision.

To my co-advisor and friend, Natália Santos, with whom I built such a special partnership throughout this journey, sharing both joyful and difficult moments. Thank you for all the time dedicated to me, for your intellectual and emotional support, for always encouraging me to broaden my horizons and look beyond, and for creating an environment in which I felt comfortable learning, questioning, and growing. You have been fundamental to my academic journey.

To my co-advisor, Minsong Li, for agreeing to be part of this supervision and for the contributions, discussions, and revisions related to this research.

To my colleagues at the National Observatory — Mariane Candido, Raysa Rocha, and Gabriella Fazio — for their willingness to contribute with suggestions, revisions, and analyses throughout the development of this work. To my colleague Ciro Climaco, for all the support related to the data and the studied area. To Mateus Michelon, for his collaboration in analyses and discussions involving seismic data, RGT, INPEFA, and cyclostratigraphy, which were essential contributions to this research. To Daniel Galvão and Sérgio Paim, for the valuable discussions and revisions concerning the depositional system investigated in this study.

To the National Observatory, an institution I deeply admire and where I am proud to be building my academic and professional journey.

To the Brazilian National Agency of Petroleum, Natural Gas and Biofuels (ANP), for providing the data that made this work possible.

To my lifelong friends — Thiago, Renato, Diego, and Ana Cristina — for walking beside me not only during this period, but throughout so many years. It is a great privilege

to have friends who have become true family over the course of life.

To my church, Raiz, for all the prayers and for being a true family to me. Especially to Pastor Renato and his wife, Caroline, for always being available to support and encourage me during difficult times.

To my cat, Jack, who came into my life almost at the beginning of my master's degree and became a source of peace and comfort throughout this journey.

To my love, Richard, for believing in me and for bringing joy and lightness to my days, even throughout the intense final stages of this master’s degree.

To my father, Paulo César, I am deeply grateful for all the care and concern you have shown for my future throughout my life. I know that my achievements bring you joy, and I hope this moment is another reason for your happiness. Thank you for celebrating every step with me.

I offer my deepest gratitude to the person who has guided my steps since the beginning of my life with incomparable love, dedication, and strength. I dedicate this work to my mother, Arlete Edna, who, with God’s help, guided me along good paths to where I am today. I am profoundly grateful for your love, care, and all your prayers. Many times, when I remain standing strong, I know that much of this strength comes from the countless times you were on your knees, praying for me. Thank you for everything, Mom.

“The LORD has done great things for us, and we are filled with joy.”

Psalm 126:3

Agradecimentos

Agradeço, primeiramente, à Deus, meu Pai e Criador, cujo amor é tão grande que não consigo expressar em palavras. Nos momentos mais difíceis desta caminhada, Ele esteve comigo. Pude seguir com segurança ao longo de toda essa trajetória porque a mão de Deus me sustentou. Obrigada, Senhor.

Ao meu orientador, Daniel Franco, por acreditar em mim desde o início. Pela paciência em ensinar e lapidar seus alunos, mesmo em meio a tantas responsabilidades; por compartilhar seus conhecimentos, suas ideias e sua experiência. Pela sensibilidade em compreender as necessidades do outro, oferecendo apoio sempre que possível. Sou grata pela oportunidade de ter desenvolvido este trabalho sob sua orientação.

À minha coorientadora e amiga, Natália Santos, com quem construí, ao longo dessa jornada, uma parceria tão especial, dividindo momentos bons e difíceis. Obrigada por todo o tempo dedicado, pelo apoio intelectual e emocional, por sempre me incentivar a enxergar além e ampliar meus horizontes, e por criar um ambiente em que me senti à vontade para aprender, questionar e crescer. Você tem sido fundamental em minha trajetória acadêmica.

Ao meu coorientador, Minsong Li, por aceitar integrar esta orientação e pelas contribuições, discussões e revisões realizadas.

Às colegas do Observatório Nacional: Mariane Candido, Raysa Rocha e Gabriella Fazio, pela disponibilidade em contribuir com sugestões, correções e análises ao longo do desenvolvimento deste trabalho. Ao colega Ciro Climaco, por todo o suporte relacionado aos dados utilizados e à área estudada. Ao Mateus Michelon, pela colaboração nas análises e discussões envolvendo dados sísmicos, RGT, INPEFA e cicloestratigrafia, contribuições que foram essenciais para esta pesquisa. A Daniel Galvão e Sérgio Paim, pelas valiosas discussões e revisões acerca do sistema deposicional estudado.

Ao Observatório Nacional, instituição que tanto admiro e onde tenho orgulho de estar construindo minha história acadêmica e profissional.

À Agência Nacional do Petróleo, Gás Natural e Biocombustíveis (ANP), pela disponibilização dos dados que tornaram este trabalho possível.

Aos meus grandes amigos de longa data: Thiago, Renato, Diego e Ana Cristina, por caminharem comigo não apenas durante este período, mas ao longo de tantos anos. É um grande privilégio ter amigos que se tornaram verdadeiros irmãos ao longo da vida.

À minha igreja Raiz, por todas as orações e por terem sido uma verdadeira família

para mim. Em especial, ao pastor Renato e à sua esposa Caroline, por estarem sempre disponíveis para me apoiar e sustentar nos momentos de dificuldade.

Ao meu gato, Jack, que chegou à minha vida quase no início do meu mestrado e foi fonte de paz e tranquilidade em tantos momentos.

Ao meu amor, Richard, por acreditar em mim e por trazer alegria e leveza aos meus dias, mesmo em meio à intensidade do final deste mestrado.

Ao meu pai, Paulo César, agradeço imensamente por toda a preocupação com meu futuro ao longo da minha vida. Sei que minhas conquistas lhe trazem alegria, e espero que este momento seja mais um motivo de felicidade para você. Obrigada por celebrar cada passo comigo.

Agradeço profundamente à pessoa que conduziu meus passos desde o início da minha vida, com amor, dedicação e força incomparáveis. Dedico este trabalho à minha mãe, Arlete Edna, que, com a ajuda de Deus, me guiou por bons caminhos até aqui. Sou extremamente grata por seu amor, cuidado e por todas as suas orações. Muitas vezes, quando permaneço firme, de pé, sei que grande parte dessa força vem das vezes em que a senhora esteve de joelhos, intercedendo por mim. Obrigada por tudo, mãe.

Contents

ABSTRACT **1**

RESUMO **3**

List of Figures **5**

List of Tables **7**

List of Abbreviations and Symbols **8**

General Outlines **9**

1 Introduction **10**

2 Objectives **12**

3 Geological Setting **13**

3.1 Campos Basin 13
3.2 Albacora Field 16
3.2.1 General aspects 16
3.2.2 Chronostratigraphy 17
3.2.2.1 Biostratigraphy 17
3.2.2.2 Previous cyclostratigraphic interpretations 18
3.3 Study Area 20

4 Cyclostratigraphy: Theoretical Background **24**

4.1 The climate spectrum 25
4.2 Milankovitch cycles 28
4.3 The astronomical time scale and its contributions to the basin chronostratigraphic frameworks 33

5 Data and Methods **35**

5.1 Data acquisition 35
5.2 INPEFA 35
5.3 Cyclostratigraphic analysis 36
5.3.1 Time-Series Analysis 37
5.3.2 Evolutionary power spectral analysis 37
5.3.3 Definition and filtering of orbital frequency bands 38

5.3.4 Correlation Coefficients analysis (COCO and eCOCO) 38
5.4 Seismic Data and RGT 39

6 Manuscript: "ARCHITECTURE-DRIVEN ORBITAL RECORDS IN A CONTINENTAL MARGIN: CYCLOSTRATIGRAPHIC–SEISMIC INSIGHTS FROM THE MIOCENE ALBACORA OILFIELD (CAMPOS BASIN, BRAZIL)" 41

7 Concluding Remarks 91

8 References 93

Abstract of the Report presented to the National Observatory's Graduate Program in Geophysics as a partial fulfillment of the requirements for the the Master's degree in Geophysics.

ORBITAL RECORDS SHAPED BY DEPOSITIONAL ARCHITECTURE IN A CONTINENTAL MARGIN: CYCLOSTRATIGRAPHIC-SEISMIC ANALYSIS OF THE MIOCENE ALBACORA OILFIELD (CAMPOS BASIN, BRAZIL)

Mariana Aragão Fernandes

Rio de Janeiro

May 2026

This master's dissertation aims to integrate cyclostratigraphy and seismic stratigraphy, together with Integrated Prediction Error Filter Analysis (INPEFA) and the Relative Geological Time (RGT) model, to investigate Miocene deposits in the Albacora Oilfield, Campos Basin, Brazil. Well-log gamma-ray data from six wells, distributed along two dip sections and one strike section, were used as paleoclimatic proxies through spectral analysis to identify periodic components related to Milankovitch cycles. Additionally, 3D seismic data acquired over the Miocene deposits of the Albacora oilfield were used to construct geological sections and to analyze the evolution of the depositional system. Cyclostratigraphic analysis revealed clear evidence of orbital forcing within the records. Spectral and evolutionary harmonic analyses allowed the identification of cycles interpreted as long and short eccentricity, obliquity and precession, most of which exceed the 95–99% confidence levels, consistent with expected orbital ratios for 14 Ma, with long- and short-eccentricity wavelengths of ~145 m and ~47 m. Results from correlation coefficient (COCO) and evolutionary correlation coefficient (eCOCO) analyses confirmed the presence of orbital forcing and indicated maximum sedimentation rates ranging from 30.0 to 45.4 cm/kyr across the wells, consistent with previously reported

values (~30 cm/kyr) for the same region. Seismic stratigraphic analysis reveals a mainly progradational system, with better stratigraphic preservation in the mid-slope domain, where thicker successions and up to three long-eccentricity cycles are recorded, in contrast to only one cycle on the shelf and at the base of the slope. These variations in stratigraphic preservation, reflected in differences in the number of long-eccentricity cycles identified along dip-oriented seismic sections, demonstrate that seismic-supported multi-well correlation is a useful tool for assessing stratigraphic completeness and, consequently, for improving 2D/3D cyclostratigraphic correlation. Hypotheses involving discontinuous sedimentation and/or depositional hiatuses associated with erosional processes were explored to account for the absence of these records in the shelf and base-of-slope settings. The RGT model corroborates a progradational pattern and reveals variability in sedimentation rates along strike sectrion, whereas INPEFA delineates key stratigraphic surfaces linked to hiatuses and erosional events. These findings underscore the need to account for depositional system dynamics when interpreting cyclostratigraphic signals and refining geological time estimates. Estimates of depositional duration accounting with variations in stratigraphic preservation were compared with biostratigraphic constraints, reshaping previous estimates of depositional duration. To our knowledge, this study provides the first systematic investigation of the lateral preservation of astronomical cyclicity within a seismic volume as controlled by depositional architecture, and demonstrates how incorporating this variability can substantially modify geological time estimates.

Resumo de dissertação apresentado ao Programa de Pós-Graduação em Geofísica do Observatório Nacional como parte dos requisitos necessários para a obtenção do título de Mestre em Geofísica.

REGISTROS ORBITAIS MOLDADOS PELA ARQUITETURA DEPOSICIONAL EM UMA MARGEM CONTINENTAL: INTEGRAÇÃO SISMO-CICLOESTRATIGRÁFICA PARA DEPÓSITOS MIOCÊNICOS DO CAMPO DE ALBACORA (BACIA DE CAMPOS, BRASIL)

Mariana Aragão Fernandes

Rio de Janeiro

Maio/2026

A presente dissertação de mestrado teve como objetivo integrar cicloestratigrafia e estratigrafia sísmica, juntamente com a Análise Integrada do Filtro de Erro de Predição (INPEFA) e o modelo de Tempo Geológico Relativo (RGT), para investigar depósitos miocênicos do Campo de Albacora, Bacia de Campos, Brasil. Dados de perfis de raio gama provenientes de seis poços, distribuídos ao longo de duas seções *dip* e uma seção *strike*, foram utilizados como proxies paleoclimáticos por meio de análises espectrais para identificar componentes periódicos relacionados aos ciclos de Milankovitch. Além disso, dados sísmicos 3D adquiridos sobre os depósitos miocênicos do Campo de Albacora foram utilizados para a construção de seções geológicas e para a análise da evolução do sistema deposicional. A análise cicloestratigráfica revelou evidências claras de forçagem orbital nos registros. As análises espectrais e harmônicas evolutivas permitiram a identificação de ciclos interpretados como excentricidade longa e curta, obliquidade e precessão, a maioria excedendo níveis de confiança de 95–99%, consistentes com as razões orbitais esperadas para 14 Ma, com comprimentos de onda de excentricidade longa e curta de aproximadamente ~145 m e ~47 m. Os resultados das análises de coeficientes de correlação (COCO) e coeficiente de correlação evolucionária (eCOCO) confirmaram a

presença de forçagem orbital e indicaram taxas máximas de sedimentação variando entre 30,0 e 45,4 cm/kyr entre os poços, consistentes com valores previamente reportados (~30 cm/kyr) para a mesma região. A análise estratigráfica sísmica revela um sistema predominantemente progradacional, com melhor preservação estratigráfica no domínio da porção central do talude, onde sucessões mais espessas e até três ciclos de excentricidade longa são registrados, em contraste com apenas um ciclo na plataforma e na base do talude. Tais variações na preservação estratigráfica, refletidas nas diferenças no número de ciclos de excentricidade longa identificados ao longo de seções sísmicas *dip*, demonstram que a correlação multi-poços apoiada por dados sísmicos é uma ferramenta útil para avaliar a completude estratigráfica e, consequentemente, para aprimorar a correlação cicloestratigráfica em 2D/3D. Hipóteses envolvendo sedimentação descontínua e/ou hiatos deposicionais associados a processos erosivos foram exploradas para explicar a ausência desses registros nos ambientes de plataforma e base do talude. O modelo RGT corrobora um padrão progradacional e revela variabilidade nas taxas de sedimentação ao longo da seção *strike*, enquanto o INPEFA delimita superfícies estratigráficas-chave associadas a hiatos e eventos erosivos. Esses resultados destacam a necessidade de considerar a dinâmica dos sistemas deposicionais na interpretação dos sinais cicloestratigráficos e no refinamento das estimativas de tempo geológico. As estimativas de duração deposicional considerando as variações na preservação estratigráfica foram comparadas com restrições bioestratigráficas, reformulando a estimativa anterior de tempo de deposição. Este estudo apresenta a primeira investigação sistemática da preservação lateral da ciclicidade astronômica dentro de um volume sísmico controlado pela arquitetura deposicional, demonstrando como a incorporação dessa variabilidade pode modificar substancialmente as estimativas de tempo geológico.

List of Figures

Figure 1. Bathymetric map of the Campos Basin. From Schreiner *et al.*, 2016.....15

Figure 2: Location of the Albacora Field (Campos Basin, southeastern Brazil) and the seismic section. Modified from De Gasperi & Catuneanu (2014).....16

Figure 3. Left: Bathymetric and geomorphological map of the Campos Basin, highlighting the location of the study area. Right: Three-dimensional bathymetric map of the study area showing the wells and the Albacora Field boundary (blue polygon). The study area comprises three seismic sections: the southern dip-oriented section A–A', intersecting wells 1-RJS-297, 4-RJS-330A, and 3-AB-68; the strike-oriented section B–B', crossing wells 3-AB-92, 1-RJS-305, and 3-AB-68; and the northern dip-oriented section C–C', connecting wells 3-AB-92 and 1-RJS-342. These latter three wells were previously analyzed by Santos *et al.* (2023). Wells 3-AB-92, 1-RJS-342, and 1-RJS-305 are outlined in black and represent the newly incorporated wells used to expand the analyzed area. Modified from Santos *et al.* (2023). 21

Figure 4. Stratigraphic chart of the Campos Basin. The study area is enclosed in the red rectangle (modified from Winter *et al.*, 2007).....22

Figure 5: Conceptual landscape of periodicities present in a typical climate signal from the atmosphere at the Earth's surface. The "landscape" at the bottom of the figure represents the responses of the climate system; the colours correspond to the various physical processes driving the variability. The top of the diagram indicates various sources and relative strengths of periodic (orbital) and random (impact/volcanic/solar) forcing variability. Between the landscape and the forcing we indicate the nomenclature of Lovejoy and Schertzer (2013a) for various timescale regimes (von der Heydt *et al.*, 2021).....25

Figure 6: Representation of the elliptical Earth's orbital plane and the astronomical parameters. The Sun occupies one of the two foci, represented by f_1 and f_2. Parameters a and b are the semi-major axis and the semi-minor axis, respectively. The plane of the Earth's orbit is inclined at an angle of I relative to a plane identified as the fixed reference ecliptic. Axis n is the normal to the orbital plan and NP is Earth's rotation axis, "North Pole". The point N is called "ascending

node" and represents the point where orbital and reference ecliptic intersects, with an angle of Ω relative to a fixed vernal point γ_0. P represents the orbital perihelion relative to γ_0. ω is the argument of the perihelion, which measures the angular distance between P and N. γ is a moving vernal point which moves clockwise along the orbit due to the precession of the equinoxes ψ, going at an angle ϖ = Π + ψ. ϕ is the Earth's counterclockwise rotation rate, and ε is the obliquity of the ecliptic that precesses clockwise at a rate ψ (Hinnov, 2013). 27

Figure 7. The variation of the orbit's eccentricity (Weedon, 2003). 29

Figure 8. Spectral analysis of the eccentricity variations. Major periodicities are shown at 400 Kyr and in the 100 Kyr band. The vertical linear scale is arbitrary (Paillard, 2001) 29

Figure 9. The variation of the angle of the tilt of the Earth's axis, relative to a direction at right angles to the ecliptic (Weedon, 2003). 30

Figure 10. Spectral analysis of the obliquity variations. Major periodicity is shown at 41 kyr. The vertical linear scale is arbitrary. (Paillard, 2001) 30

Figure 11. Two factors control the climatic precession: (a) the rotation of the direction of tilt of the Earth's axis; (b) the rotation of the long axis of the Earth's orbit (modified from Weedon, 2003). 31

Figure 12. Spectral analysis of the precession variations. Two groups of periodicities are shown, around 23 and 19 kyr. The vertical linear scale is arbitrary (Paillard, 2001) 32

List of Tables

Table 1: Simplified lithostratigraphic correlation from the Campos Basin (modified from Guardado *et al.*, 1989). 14

Table 2: UTM coordinates, depth range (m), and thickness (m) of the analyzed section for each well. 22

List of Abbreviations and Symbols

AR(1) …… Robust first-order autoregressive red-noise model

ATS .....Astronomical Time Scale

COCO..... Correlation Coefficient

DPSS ..... Discrete Prolate Spheroidal Sequences

eCOCO..... Evolutionary Correlation Coefficient

EHA.....Evolutionary Harmonic Analysis

FFT.....Fast Fourier transform

GR .....Gamma Ray

INPEFA.....Integrated Prediction Error Filter Analysis

LOESS..... Locally Estimated Scatterplot Smoothing

MESA ..... Maximum Entropy Spectral Analysis

MTM.....Multi-taper Method

PEFA .....Prediction Error Filter Analysis

RMS …… Root Mean Square

RGT……..Relative Geological Time

General Outlines

This dissertation is structured in the format of a scientific article in accordance with the guidelines of the Graduate Program in Geophysics at the National Observatory. The work is organized into eight chapters: the initial sections present the introduction, objectives, geological setting of the study area, fundamental concepts of cyclostratigraphy, and a description of the applied methodologies. The final chapters include the manuscript entitled **"ARCHITECTURE-DRIVEN ORBITAL RECORDS IN A CONTINENTAL MARGIN: CYCLOSTRATIGRAPHIC–SEISMIC INSIGHTS FROM THE MIOCENE ALBACORA OILFIELD (CAMPOS BASIN, BRAZIL)"** submitted to the peer-reviewed international journal Marine Geology, as well as the concluding remarks of the dissertation and references.

Chapter 1

Introduction

Cyclostratigraphic analyses enable the identification of variations in the stratigraphic record within a sedimentary sequence, and their interpretation can reveal cyclic alternations in the depositional environment of the rock. These alternations can then be linked to astronomically forced climate changes (Kodama & Hinnov, 2015; Hinnov, 2018). Cyclostratigraphy can also be understood as the study of cyclic stratigraphic records, in which the cycles represent regular and periodic oscillations that may originate from various sources, such as orbital parameter variations, solar activity, or climate fluctuations driven by internal processes within the Earth's climate system (Weedon, 2003). The stratigraphic record influenced by orbital variations reflects changes in Earth's orientation relative to the Sun, driven by the gravitational pull of the Moon, the Sun, and other planets. These variations affect the amount of solar radiation the planet receives (Hinnov, 2018).

Milankovitch cycles are orbital cycles that can shape the depositional record. The correlation between cyclostratigraphy and astronomical models gave rise to astrochronology, which provides highly consistent modern astronomical solutions with well-defined periodicities for the past 50 million years (Hinnov, 2018). Cyclostratigraphic studies based on Brazilian sedimentary records began to emerge in the late 20th century (e.g., Sinito *et al.*, 1981; Ernesto & Pacca, 1981).

Despite being widely exploited by the hydrocarbon industry, the Campos Basin – located on the eastern Brazilian margin, in southeastern Brazil, extending from the northern coast of the state of Rio de Janeiro, near the Cabo Frio Arch, to the southern portion of Espírito Santo State, near the Vitória Arch, and covering an area of approximately 100,000 km² (Osorio, 2017; Bastos & Bastos, 2017) – still requires further efforts to understand its geological and chronostratigraphic evolution. Understanding the evolution of this basin is therefore crucial for optimizing hydrocarbon exploration, and numerous studies have sought to describe its architecture and development (e.g., Linhares et al., 2018; Castro & Picolini, 2014; Figueiredo Jr. et al., 2014; Almeida & Kowsmann, 2014). In this context, cyclostratigraphy represents a powerful tool for establishing high-resolution chronostratigraphic frameworks (Kodama & Hinnov, 2015). However, few cyclostratigraphic studies have focused on the Campos Basin to date (e.g., Castro, 2005;

Santos et al., 2023).

Among the main exploratory areas in the Campos Basin, the Albacora Oilfield stands out as one of the most significant hydrocarbon exploration provinces. Located approximately 110 km offshore (De Gasperi & Catuneanu, 2014), this field has been under investigation for about thirty years. As of 2018, it had an extensive seismic grid and 49 producing wells (ANP, 2018), enabling the integration of seismic stratigraphic, biostratigraphic, and cyclostratigraphic studies in the region. A previous study by Santos *et al.* (2023) combined seismic data, biostratigraphy, and cyclostratigraphic analysis of gamma-ray (GR) logs from three wells in the southern sector of the field. Their results enabled the identification of orbital-scale sedimentary cycles, the estimation of sedimentation rates, and the development of an Astronomical Time Scale (ATS) for the investigated interval. Recently, newly available higher-resolution 3D seismic data for the Albacora Oilfield, released by the Brazilian National Agency for Petroleum, Natural Gas and Biofuels (ANP), have enabled a reassessment and expansion of the chronostratigraphic framework originally proposed by Santos *et al.* (2023).

In this study, we present an updated and expanded chronostratigraphic interpretation of the Miocene succession in the Albacora Oilfield, based on three stratigraphic sections that integrate six GR well-logs with seismic data. These include a strike-oriented section connecting the dip section previously analyzed by Santos *et al.* (2023), as well as a northernmost dip section that incorporates two additional wells. Collectively, these sections form the basis of a chronostratigraphic framework covering an area of approximately 62 km².

Relative to the previous study, the incorporation of higher-resolution seismic data – combined with the integration of cyclostratigraphic results with Relative Geological Time (RGT) volumes and Integrated Prediction Error Filter Analysis (INPEFA) – constitutes a significant improvement. This integrated framework supports a more detailed assessment of stratigraphic preservation by capturing both lateral and vertical variability, and facilitates the identification of better-preserved successions, strengthens stratigraphic correlations, and refines interpretations of the timescales governing depositional processes.

Chapter 2

Objectives

This master's dissertation aims to advance the investigation of the sedimentary evolution of the Miocene succession in the Albacora Oilfield, Campos Basin, Brazil. The study integrates cyclostratigraphic analysis and seismic stratigraphy with INPEFA and the RGT model to investigate the stratigraphic architecture and depositional evolution of the Miocene deposits in the study area.

The specific objectives of this research are as follows:

a) To investigate and interpret the possible occurrence of orbital forcing record in Miocene sedimentary deposits through the analysis of gamma-ray data series from six wells located in the Albacora Oilfield.

b) To conduct an integrated analysis combining cyclostratigraphy and seismic stratigraphy for the stratigraphic correlation of the six analyzed wells.

c) To enhance the chronostratigraphic framework proposed by Santos et al. (2023) through a multi-method approach and the expansion of the study area, integrating the northern, central, and southern transects of the Albacora Oilfield into a single dataset.

d) To estimate sedimentation rates of the studied deposits.

e) To identify areas of enhanced stratigraphic preservation.

f) To investigate the causes underlying the absence or incompleteness of the stratigraphic record in poorly preserved sectors.

g) To assess whether the 2D seismic-cyclostratigraphic correlation proposed by Santos et al. (2023) can be expanded into a 3D interpretation, based on the integration of dip and strike sections from the same area of the Albacora Oilfield, potentially supporting new efforts to define isochronous surfaces at orbital-scale resolution for its Miocene deposits.

Chapter 3

Geological Setting

3.1 Campos Basin

The Campos Basin is located at the East Brazilian Margin (southeastern Brazil), and it extends from the northern coast of the State of Rio de Janeiro to the southern portion of the State of Espírito Santo. It is bounded to the north by the Vitória High, to the south by the Cabo Frio High. Its extension is about 100,000 km² (De Gasperi & Catuneanu, 2014).

The sedimentary evolution of the Campos Basin is related to the rifting process of the Gondwana supercontinent and the subsequent opening of the Atlantic Ocean; the most accepted interpretation for the opening is lithospheric stretching, crustal thinning (McKenzie, 1978) and subsequently a thermal anomaly (Royden & Keen, 1980) with associated subsidence. In weakness zones, the crust's thinning led to the rift's rupture and generated a deposition of the rift section in a regionally uplifted area, with an expressive presence of volcanic rocks at the bottom of the basin, aged between 130 e 120 Ma (Bastos & Bastos, 2017).

According to Winter *et al.* (2007), the Campos Basin stratigraphy can be divided into three big tectonosedimentary units, also called megasequences:

Rift or continental: this sequence was formed under mechanical subsidence regime and is characterized by direct control of the basement structural framework and continental sedimentation dominated by siliciclastic deposits and lacustrine coquinas (De Gasperi & Catuneanu, 2014; Guardado *et al.*, 1989). It is represented by rocks from the Cabiúnas Formation, which includes basalts and volcaniclastic rocks, and the Lagoa Feia Group (135 - 118 Ma). The rift sequence is composed by the Atafona formations (siltstones and sandstones with talc-stevensite), Coqueiros (coquinas and shales) and Itabapoana (conglomerates) (de Castro & Picolini, 2015; Bastos & Bastos, 2017).

Post-rift or transitional: corresponds to the upper part of the Lagoa Feia Group, which was deposited during the Aptian. This unit represents an intermediate phase between thermal and mechanical subsidence, in which continental and marine sedimentation took place (Guardado *et al.*, 1989). The transitional sequence is usually divided in two main units: (i) a lowermost unit, which belongs to the Itabapoana, Gargaú

and Macabu Members and is composed of siliciclastic rocks and carbonates; and (ii) uppermost unit, composed by evaporitic rocks comprised by the Retiro Member (Dias *et al.*, 1990).

Drift or marine: formed by the deposition of the Macaé and Campos Groups, which comprises sedimentary rocks ranging from the Albian to the Holocene (Winter *et al.*, 2007). This sequence consists of marine sediments deposited under a stationary thermal subsidence regime (De Gasperi & Catuneanu, 2014). The Macaé Group is dominated by carbonate sediments and comprises the Goitacás, Quissamã, Outeiro (calcilutitos and shales), Imbetiba (calcilutitos) and Namorado (sandstones) formations. The Campos Group is composed of the Ubatuba (shales), Emborê (carbonates) and Carapebus (sandstones) formations. The latter group is the object of study of this dissertation, and to which the Albacora field is associated (Bastos & Bastos, 2017). The megasequences groups and formations are shown in Table 1.

Table 1. Simplified lithostratigraphic correlation from the Campos Basin (modified from Guardado *et al.*, 1989).

Megasequences	Group	Formations
Drift	Campos	Ubatuba
		Carapebus
		Emborê
	Macaé	Goitacás
		Quissamã
		Imbetiba
		Outeiro
		Namorado
Post-rift	Lagoa Feia	Retiro
		Gargaú
		Macabu
		Itabapoana
Rift		Atafona
		Coqueiros
	-	Cabiúnas
Igneous Basement	Basalts	-

In terms of submarine physiography, the basin can be subdivided into the regions: continental shelf, continental slope, continental rise, and São Paulo Plateau (Fig. 1). The

continental shelf is bounded by the isobaths of 10 and 150 m; it has a low relief, with an average slope around 0.5 degree. The outer limit of this region is approximately 180 meters deep, which represents the break of the platform (Figueiredo Jr. *et al.*, 2015; Borges *et al.*, 2015).

According to Almeida & Kowsmann (2014), the continental slope has an extension of ~ 40km, extending from the shelf break (110m isobath) to 2.000m, where it merges with the São Paulo Plateau; and it shows the highest continental margin slope values (0-25°). These morphological variations are caused by submarine canyons, ravines and furrows, which are the main transport routes of sediments from the platform to the São Paulo Plateau.

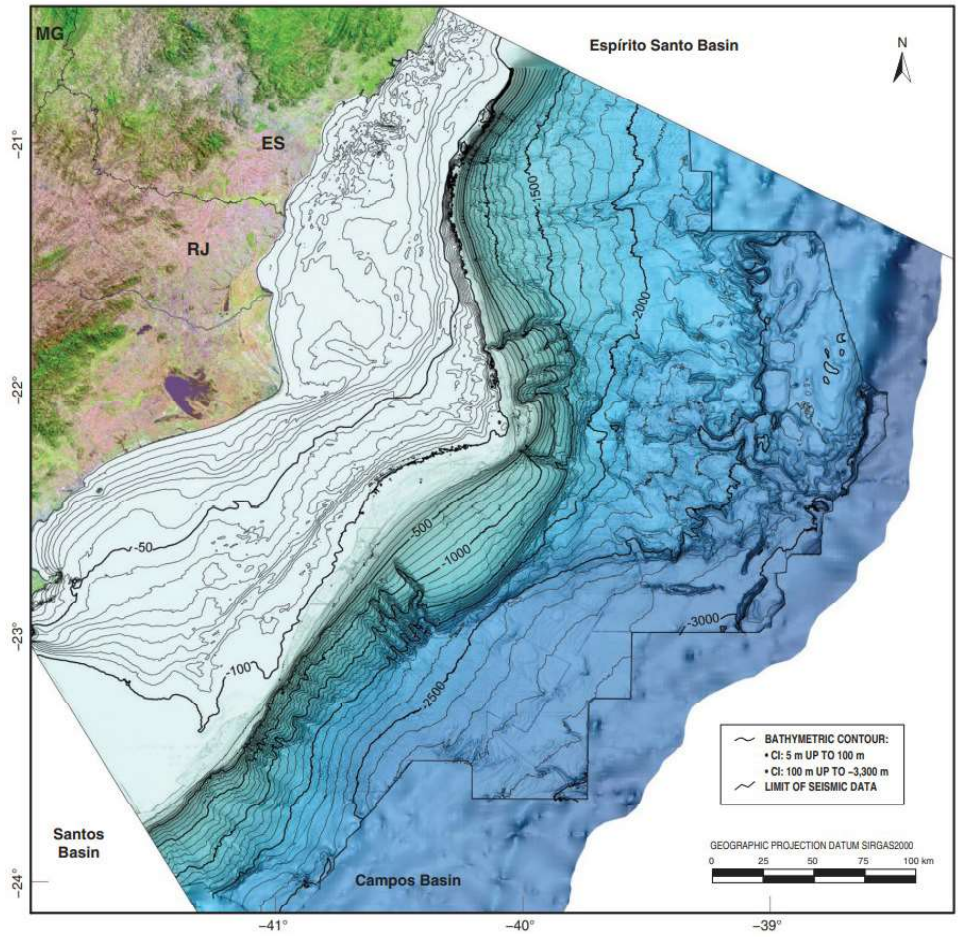


Figure 1. Bathymetric map of the Campos Basin. From Schreiner *et al.*, 2016.

São Paulo Plateau is a marginal plateau that represents an extension of the continental margin slope. Its boundaries at the Campos Basin are gradational; the limit with the foot of slope is located at a depth of 3200 to 3400m eastward. To the west, the limit

with the continental slope occurs at a depth of 2900m. Its width ranges from 180 to 289 km and its slope varies from 0 to 2 degrees. São Paulo Plateau loses almost all its marginal plateau characteristics in the transition to the foot of slope, being characterized by the occurrence of salt diapirs, sometimes buried. (Zembruscki, 1979).

A muddy sediment package (from debris flows and contours) on the salt layer constitutes the São Paulo Plateau. The limit of the province of salt, with or without escarpment, does not coincide with the plateau boundary across the entire extension. In some regions, the plateau boundary of São Paulo is a little further, being established by post-salt sedimentation (Castro, 1993).

3.2 Albacora Oilfield

3.2.1 General aspects

The Albacora field was discovered in the 1980s, during a well drilling campaign (Bastos & Bastos, 2017). It is located approximately 110 km (68 mi) from the coast of the Campos Basin (Fig. 2), in a current continental slope setting; the water depths range from 100 to 1050 m. (De Gasperi & Catuneanu, 2014).

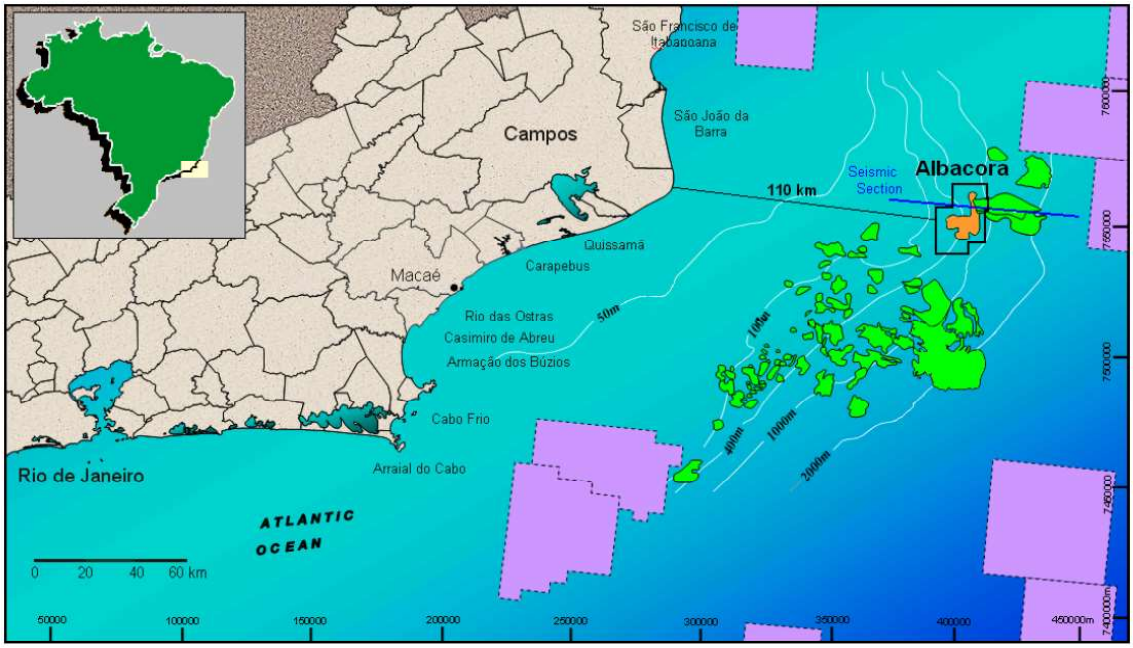


Figure 2. Location of the Albacora Field (Campos Basin, southeastern Brazil) and the seismic section. Modified from De Gasperi & Catuneanu (2014).

The producing intervals of the Albacora Oilfield comprise Cretaceous turbiditic sandstones associated with the Upper Macaé Formation, as well as Paleogene and Neogene turbiditic sandstones - specifically from the Eocene, Oligocene, and Miocene - related to the Campos Formation, Carapebus Member (Souza Cruz *et al.*, 1987). Among these, the Eocene reservoirs are noteworthy for comprising two major packages of deep-water turbiditic sandstones, which are separated by a pelitic interval (Gasperi & Catuneanu, 2014). The Oligocene and early Miocene reservoirs also deserve special attention due to their broad spatial distribution, significant thicknesses, and favorable petrophysical properties, such as high porosity and permeability (de Souza Cruz *et al.*, 1987). The deposition of these turbidites is genetically linked to both relative sea-level variations, as proposed by Vail *et al.* (1977), and to the salt tectonics active in the region. These factors disrupted the balance between sedimentation on the platform and in the basin, resulting in a substantial sediment influx that favored the development of submarine fan systems (Guardado *et al.*, 1986).

3.2.2 Chronostratigraphy

3.2.2.1 Biostratigraphy

Biostratigraphy subdivides geological strata into units based on their fossil content, a process known as biostratigraphic zonation. Through the identification of fossils within a stratigraphic sequence and the analysis of their vertical distribution, it is possible to define key biostratigraphic events, such as the first and last occurrences of a given taxon. A stratigraphic boundary or surface within a sedimentary succession marked by a change in fossil content is referred to as a biohorizon. These boundaries define the base and top of a biozone, which is a body of strata characterized by its fossil assemblage (Agnini *et al.*, 2017; North American Commission on Stratigraphic Nomenclature, 2005; Pearson, 1998).

Calcareous nannofossils are among the most widely used groups of microfossils in marine biostratigraphy. They consist of calcitic skeletal remains, typically smaller than 63 µm, including coccoliths and nannoliths. Their application in studies of basins along the Brazilian continental margin dates back to the 1960s, and they remain extensively used in biostratigraphy due to their good preservation, high abundance, wide geographic distribution, and rapid evolutionary rates (Batiston *et al.*, 2016; Bown & Young, 1998).

The sedimentary interval selected for this study is defined by the presence of two calcareous nannoplankton taxa: *Helicosphaera ampliaperta* (17.95 – 14.9 Ma), which exhibits a nearly oval outline and is of significant stratigraphic importance due to its wide geographic distribution and relatively restricted temporal range; and *Sphenolithus belemnos* (19.01 – 17.75 Ma), a narrow, dart-shaped in side view nannoplankton, rare at high latitudes and easily recognized under an optical microscope (Okada and Bukry, 1980; Gradstein *et al.*, 2018; Bolli *et al.*, 1989; Backman *et al.*, 2012; Bramlette and Wilcoxon, 1967).

3.2.2.2 Previous cyclostratigraphic interpretations

The first cyclostratigraphic study on the Miocene sedimentary deposits of Campos Basin was provided by De Castro (2005), who investigated the interval between the tops of N-550 (18.9 Ma, Mesoburdigaliano) and N-580 (14.4 Ma, Eoserravaliano) nanofossil biozones. Such region is inserted in the Prograding Oceanic Sequence – a region close to our study area, which is discussed by Dias *et al.* (1990) as deposited from Eocene to recent.

De Castro (2005) discussed a possible orbital influence on the basin's Miocene sedimentation, by evaluating the cycles obtained from seismic, well-log data and biostratigraphic dating. The studied sedimentary succession presented a clear rhythmic alternation between shales and marls. The author performed spectral analyzes on the seismic and sonic traces to locate the dominant wavelengths, and a correlation matrix with Milankovitch cycles, in addition to obtaining the corresponding accumulation rate for each wavelength. The intervals between the tops of the biozones were obtained from the sonic curve. Each biozone was divided into segments and different sedimentation rates were obtained for each segment.

The seismic trace shows a clear depth-related trend, with increasing depth leading to progressive amplitude attenuation due to effects such as spherical divergence, energy absorption, and partitioning at interfaces. This effect is considered to have been mitigated by subdividing the biozones into segments. The estimated duration of sedimentation for the interval corresponding to the N-570 biozone is approximately 1.25 Ma, about 15% higher than the 1.2 Ma inferred from biostratigraphy (Azevedo *et al.*, 1992). Assuming no significant hiatuses or erosional truncation, the mean accumulation rate for this biozone is on the order of ~30 cm/kyr. Sedimentation rates, however, show considerable variability, ranging from ~4.5 cm/kyr (N-560a) to ~40 cm/kyr (N-570b). Spectral evaluation of the sonic

log reveals orbital-scale cyclicity, including long and short eccentricity (~410 and ~100 kyr), obliquity (~41 kyr), and precession (~23 and ~19 kyr). Among these, precessional forcing appears to dominate the sedimentary rhythm, except within the interval bounded by the tops of biozones N-570 and N-580, where obliquity-related periodicities are more prominent.

The first published study which proposed an integration of seismic stratigraphy and well-log GR-based cyclostratigraphic interpretation for improvement of the chronostratigraphic framework for the Miocene section of the Albacora Oilfield was given by Santos *et al.* (2023). Specifically, the authors investigated three wells in its southern region along with 2D seismic data, which assisted in the appropriate selection of wells, which were chosen due to its absence of major tectonic faults and erosional surfaces. The seismic interpretation involved mapping horizons, densifying the 3-D seismic interpretation, generating an interpolated 2D section from 3D seismic data to identify clinoforms and erosional surfaces, and conducting a seismic resolution study (Widess, 1973) to refine horizon depths, estimate uncertainties, and assess reflector displacement, which indicated a possible vertical shift of ±15 m from the original position.

Cyclostratigraphic analysis of gamma-ray logs from three wells identified sedimentation cycles using spectral methods. Spectral peaks linked to long and short eccentricity, obliquity, and precession were observed, along with ~60–70 Myr cycles possibly related to eccentricity-precession modulations. Gaussian band-pass filters isolated eccentricity signals, which were compared to the Laskar *et al.* (2011) model for astronomical tuning and ATS construction. Long-eccentricity cycles were identified in all wells, and amalgamated cycle pairs were found in all three wells (E4-E3 in well 3-AB-68; E5-E6 in well 4-RJS-330A and E5-E6 in well 1-RJS-297) and interpreted as resulting from erosional processes common in continental slope settings. Only one of the three wells had associated biozones (well 1-RJS-297); two biozones were used to anchor the ATS. Five clinoforms were identified from the 2D seismic section interpretation. Clinoform CL5 was found at the same depth as the *Helicosphaera ampliaperta* biozone in well 1-RJS-297, allowing its age to be estimated at 14.9 Ma. The proximity of the species *Sphenolithus belemnos* (dated at 17.95 Ma) to the base of cycle E1 and a 405 kyr cycle from clinoform CL1 enabled the age of CL1 to be determined as 17.5 Ma. The estimated ages of clinoforms CL1 and CL5 allowed them to be used to estimate ages for other wells, based on the assumption that the clinoforms have the same estimated age across all wells.

Through COCO and eCOCO analyses, the optimal sedimentation rate and the null hypothesis of absent orbital forcing were investigated and showed sedimentation values

corresponding to 7 orbital cycles (405, 125, 95, 40.4, 23.5, 22.2, and 19 kyr), confirming the influence of Milankovitch cycles. Significant sedimentation peaks found were between ~30 and ~40 cm/kyr throughout the three wells. A 2D ATS was generated for the southern portion of the Albacora Oilfield in the Miocene section, combining cyclostratigraphic and seismic stratigraphic analyses.

3.3 Study Area

Building on the framework established by Santos *et al.* (2023) – in which seismic reflectors, erosional surfaces, orbital imprint, and sedimentation rates were characterized along a dip-oriented transect (line **A–A'**) – the present study expands the analysis toward the northern and central sectors of the Albacora Oilfield. This expansion is achieved by incorporating three additional wells located near the slope break: **3-AB-92** (landward sector), **1-RJS-305** (central sector, farther south), and **1-RJS-342** (outer shelf, more distal). The transects are arranged into three lines: the northern **C–C'** linking wells **3-AB-92** and **1-RJS-342** (5.653 m km apart), the central B–B' crossing wells **3-AB-92**, **1-RJS-305**, and **3-AB-68** (with 5.772 m and 5.167 m inter-well spacing along strike), and the southern **A–A'**, as defined by Santos *et al.* (2023), connecting wells **1-RJS-297**, **4-RJS-330A**, and **3-AB-68** (2,384 m and 4,939 m apart) (Fig. 3; Table 2). These three transects are treated as a unified dataset to enable integrated cyclostratigraphic and seismic correlations across all six wells and to validate the applicability of the integrated approach over a broader spatial scale. Additionally, the three southern wells previously studied by Santos *et al.* (2023) were reanalyzed using updated seismic data and revised cyclostratigraphic approaches to maintain consistency across the dataset.

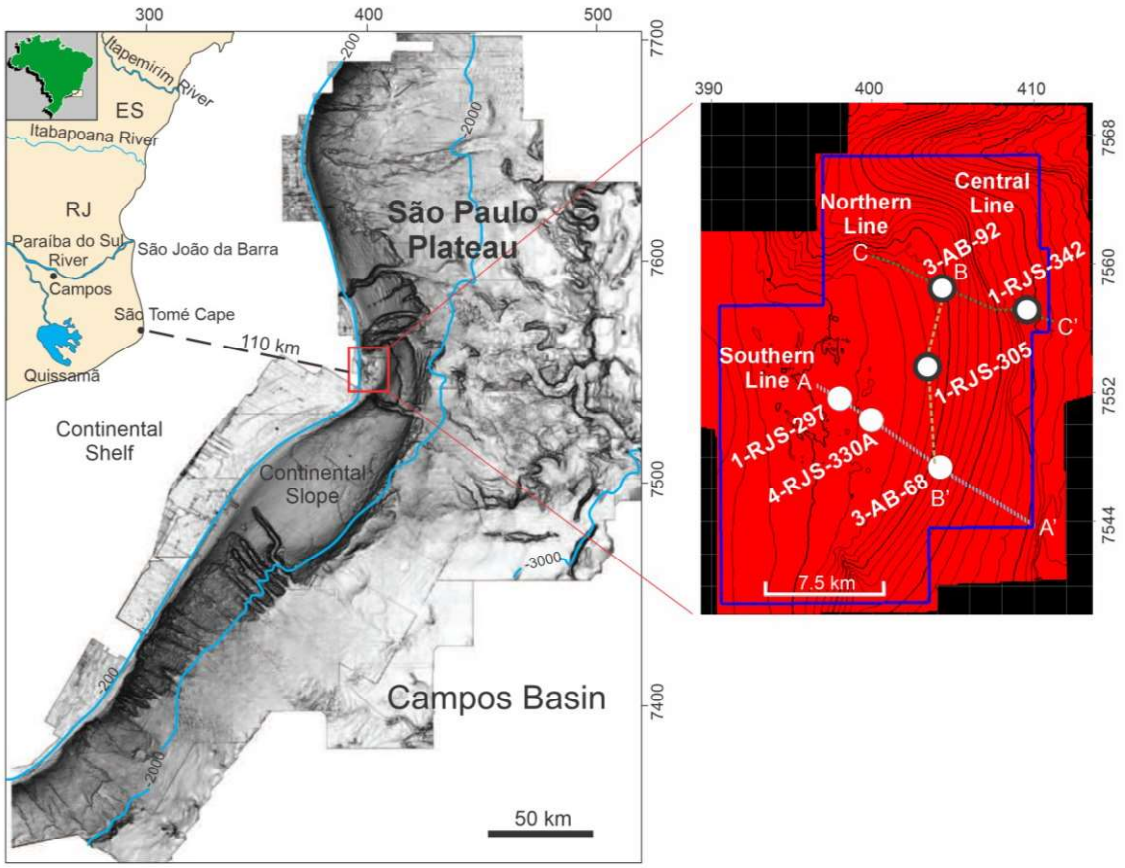


Figure 3. Left: Bathymetric and geomorphological map of the Campos Basin, highlighting the location of the study area. Right: Three-dimensional bathymetric map of the study area showing the wells and the Albacora Oilfield boundary (blue polygon). The study area comprises three seismic sections: the southern dip-oriented section A–A', intersecting wells 1-RJS-297, 4-RJS-330A, and 3-AB-68; the strike-oriented section B–B', crossing wells 3-AB-92, 1-RJS-305, and 3-AB-68; and the northern dip-oriented section C–C', connecting wells 3-AB-92 and 1-RJS-342. These latter three wells were previously analyzed by Santos et al. (2023). Wells 3-AB-92, 1-RJS-342, and 1-RJS-305 are outlined in black and represent the newly incorporated wells used to expand the analyzed area. Modified from Santos et al. (2023).

Table 2: UTM coordinates, depth range (m), and thickness (m) of the analyzed section for each well.

Well	Coordinates (UTM)		Depth Interval (m)		Interval thickness (m)
1-RJS-297	7551625.0	397943.0	802.2	3059.4	2257.2
1-RJS-305	7552641.0	403510.0	899.2	2450.0	1550.8
1-RJS-342	7557373.0	409522.0	1400.0	2350.0	950.0
4-RJS-330	7550283.0	399914.0	814.8	2699.9	1885.1
3-AB-68	7547327.9	404161.6	1612.0	3362.9	1750.9
3-AB-92	7558198.0	404530.6	1550.0	2400.0	850.0

In this work, the sedimentary interval of interest corresponds to the Miocene sediments from the Aquitanian, Langhian and Burdigalian ages (Fig. 4). This package is composed predominantly of sandstones resulting from dense flows and bypass currents, siltstones and shales. Diamictites corresponding to slope base portions and deep-water marshes form the sedimentary record, and the amalgamated sandy bodies form a special layer of rock of the order of hundreds of meters (Winter *et al.*, 2007). The slope is stratigraphically above the reservoir and exhibit a geometry in the form of unusual clinoforms, which causes the rocks of the Miocene age to present a bypass of turbiditic sands and form onlapping geometries rich in diamectite and claystones (De Gasperi & Catuneanu, 2014).

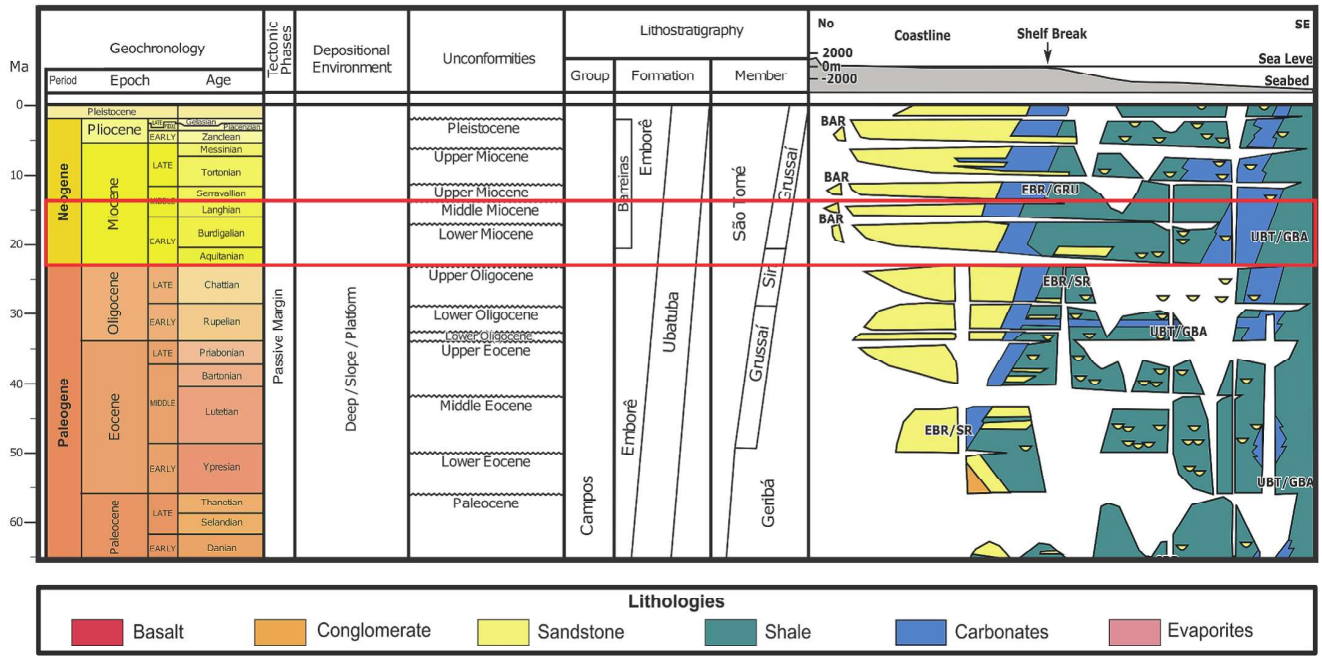


Figure 4. Stratigraphic chart of the Campos Basin. The study area is enclosed in the red rectangle (modified from Winter *et al.*, 2007).

Chapter 4

Cyclostratigraphy: Theoretical Background

The movement of the Earth in Solar System determines day or night, seasons, tidal and other movements (Schwarzacher, 1993). These recurrent variations are reflected in climate and temperature and can be represented in a climatic spectrum, indicating the wide range of temporal and spatial scales of climate variation and the different spectral density between them (von der Heydt *et al.*, 2021).

The climate changes can be recorded in sediments, as first observed by Gilbert (1895) when relating the regular alternations of limestone and shale in the Niobrara chalk, Colorado, with astronomical cycles (Schwarzacher, 1993). Cyclostratigraphy can be defined as the subdiscipline of stratigraphy that is concerned with the identification, characterization, correlation, and interpretation of cyclical variations (periodic or quasi periodic) in the stratigraphic record, and with their applications in geochronology with the purpose to increase accuracy and resolution of temporal stratigraphic structures (Hilgen *et al.*, 2004; Strasser *et al.*, 2006). The study of sedimentary record is performed through astronomical cycles of known periodicities, to interpret repetitive patterns (Strasser *et al.*, 2006).

A sedimentary cycle is a pattern of differences in physical and chemical parameters that repeats itself regularly in a sedimentary sequence. The events that cause the patterns can be produced either by occasional processes or by oscillatory systems, the latter being responsible for the formation of sedimentary cycles. The main concern of cyclostratigraphy are cycles with regular time intervals, and more specifically, time intervals that can be associated with known time periods (Schwarzacher, 1993). The cycles most used in cyclostratigraphy are the Milankovitch cycles, caused by disturbances in the Earth's orbit and in the inclination of its axis.

In this chapter, we will discuss the forces causing climate changes, the climatic cycles present in the climatic spectrum, the Milankovitch cycles and how the astronomical time scale can contribute to chronostratigraphic problems.

4.1 The climate spectrum

The Earth's climate has undergone several changes over time, and the magnitude of such changes is related to the period and place in which they occurred (Berger *et al.*, 1992). Internal natural processes and external influences are responsible for generating annual fluctuations and long-term changes in the Earth's complex climate system, which includes subsystems such as the atmosphere, oceans, ice sheets and biosphere, and interact with each other, producing effects that can expand or reduce the processes involved (Berger *et al.*, 1992). Geological records are the only available documentation of long-term environmental changes and the factors that influence them, such as carbon dioxide, solar radiation and tectonic plates (Meyers, 2019). Such records are most often obtained from sedimentary sections, generating the stratigraphic record (Weedon, 2003).

According to Ruddiman (2001), there are three fundamental kinds of climate forces in the natural world:

- **Tectonic processes** are generated by Earth's internal heat and affects its surface and geography through the movement of tectonic plates. These are slow processes that can occur in the timescale of millions to billions of years.
- **Earth-orbital changes**, caused by the variations in the Earth's orbit around the Sun. These changes affect the amount of radiation received by the Sun; they can occur in a timescale of tens to hundreds of thousands of years.
- **Changes in the strength of the Sun**, as the increase of this strength through the ~4.65 Ga of Earth's existence and the short terms variations that occur over decades or longer. These changes also affect the amount of solar radiation received.

The climate variability over time scales can be represented as a power spectrum. Mitchell (1976) presented an original "Mitchell spectrum" (MS) based on observations available in the mid 1970s, such as paleoclimate records and instrumental observations data of atmospheric variability. The MS spectrum shows an estimate of relative variance of climate over all periods of variation, from those comparable to the age of the Earth to about one hour (Mitchell, 1976). The most common observable proxie used for a climate spectrum is surface temperature (a global average or at a specific location); it is also possible to use precipitation, sea level or ice extend, although these have less dependence on radioactive forces and therefore it would be harder to interpret its influence (von der Heydt *et al.*, 2021).

Von der Heydt *et al.* (2021) presented a modern view of climate variability and discussed their causes and mechanisms, including at the MS spectrum some of the more recent developments in climate variability. The external forcing is shown in the upper part of the diagram in Figure 5. The landscape at the bottom represents the responses and internal variability due to dynamics in various parts of the Earth system. Impact events, solar variability and vulcanism events represent aperiodic forcing of highly variable amplitude.

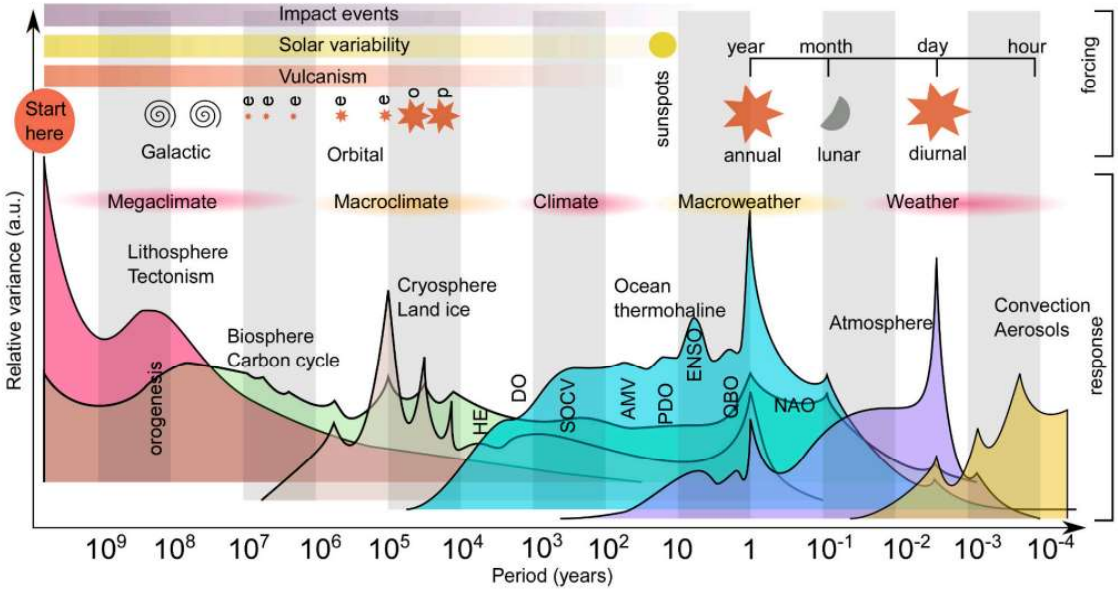


Figure 5. Conceptual landscape of periodicities presents in a typical climate signal from the atmosphere at the Earth's surface. The "landscape" at the bottom of the figure represents the responses of the climate system; the colours correspond to the various physical processes driving the variability. The top of the diagram indicates various sources and relative strengths of periodic (orbital) and random (impact/volcanic/solar) forcing variability. Between the landscape and the forcing we indicate the nomenclature of Lovejoy and Schertzer (2013a) for various timescale regimes (von der Heydt *et al.*, 2021).

According to Mitchell (1976), there are different types of variability. The potential sources of the variability can be internal to the climatic system, external to the climatic system or an interaction of internal variability and external forcing.

a) Internal climate variability

Cycles with an average period of 2500 years are superimposed upon the Quaternary ice-volume cycles related to the Earth's orbital elements in Figure 5 (Pisias *et al.*, 1973; Berger, 1977a). Those cycles have smaller amplitudes and are understood to occur due to the turnover frequency of the deep-ocean thermohaline circulation (Berger, 1979). On the intraseasonal to interannual variability timescale, two modes of variability are shown in Figure 5. The sea surface temperature increases in the equatorial eastern Pacific known as

El Niño-Southern Oscillation (ENSO) occurs usually once every 3-7 years (Philander, 1990). Quase-biennial Oscillation (QBO), an irregular downward propagating zonal wind variation at the tropical lower stratosphere (Wallace, 1973), has an average period of ~28 months (Newman *et al.*, 2016).

On the decadal-to-multidecadal climate variability timescale, the Pacific Decadal Oscillation (PDO), cyclical variations in sea surface temperatures in the Pacific Ocean, may show more energetic fluctuations in two periods - from 15 to 25 years and from 50 to 70 years (Mantua & Hare, 2002); the Atlantic Multidecadal Variability (AMV), a combination of higher and lower temperatures of the North Atlantic basin-wide sea surface, seems not to have a single well-defined periodicity (Ting *et al.*, 2011); first analyses of North Atlantic variability (Schlesinger & Ramankutty, 1994; Kushnir, 1994) indicated a period of 50-70 years based on observed sea-surface temperature; Delworth & Mann (2000) have found a periodicity between ∼40 and 128 years in a historic observation for the last 330 years, with a peak at 42.7 years for the years 1856–1990. The Dansgaard-Oeschger cycles are very abrupt fluctuations that took place at the North Atlantic basin, first observed in Greenland ice core records. The climate shifts were characterized by an abrupt warming from a cold glacial state (stadial) and a warmer (intersadial) state (Petersen, 2013; von der Heydt *et al.*, 2021).

b) External climate variability

The lithosphere tectonism is considered by Mitchell (1976) an external stochastic mechanism of climatic change, as the interior of the Earth is not part of the climatic system. Tectonic processes affect climate through the gradually remodel of the ocean basin over Myr timescale, the height of the continents, mountain ranges, the reach of volcanic activity, submarine interconnections and possibly other geophysical conditions (Mitchell, 1976). Several changes in global climate can be associated with plate tectonics. Zachos *et al.* (2001) list some tectonically driven events that caused a major shift in the dynamics of the global climate system over the last 65 My, such as the North Atlantic rift volcanism in the Late Paleocene and the Tasmania-Antarctic Passage opening.

Other two examples of forcing from outside the climatic system are the deterministic diurnal cycle and annual solar forcing of climate. These forces occur due to the rotation and the inclination of the Earth's rotation axis in the translation movement, respectively (Mitchell, 1976). Sources identified as deterministic also include the long-timescale astronomical forcing (Crucifix *et al.*, 2006), also called Milankovitch cycles.

4.2 Milankovitch cycles

Earth scientists from the 19th century started to understand the relation between sedimentary cycles and the perturbations in the Earth's orbit and rotation, caused by the gravitational interaction of the Earth with the other bodies of the Solar System. The first works relating orbital control to paleoclimate changes were proposed by Jens Esmark in 1824, Agassiz in 1838, Adhèmar in 1842, Croll in 1868 and Gilbert in 1895. The Milankovitch hypothesis, from 1941, linked the climate response mechanisms such as alternation between glacial–interglacial periods to changes in summer insolation at the high latitudes of the Northern Hemisphere and suggested that this climate change is caused by variations in orbital elements – in particular eccentricity, obliquity, and precession (Berger, 2012; Fragoso *et al.*, 2022).

The Earth's climate, as is generally known, undergoes seasonal variations, caused by the movement of the Earth in its orbit around the Sun. These variations occur due to the inclination of the Earth's axis, which causes the northern and southern hemispheres to receive greater or lesser amount of solar radiation, depending on the position of the planet in orbit (Schwarzacher, 1993). If all the parameters that determine the seasons remained fixed, the average climate over the course of a year would remain constant; however, the orbital of all planets go through variations (Schwarzacher, 1993). Spectral analyzes of Quaternary paleoclimatic records provided evidence that, at least in the vicinity of the frequencies of obliquity and precession, a considerable number of climatic variations occurred due to changes in insolation, caused by changes in the Earth's orbit (Berger *et al.*, 1992). The fundamental Earth's orbital elements are schematically represented in Figure 6.

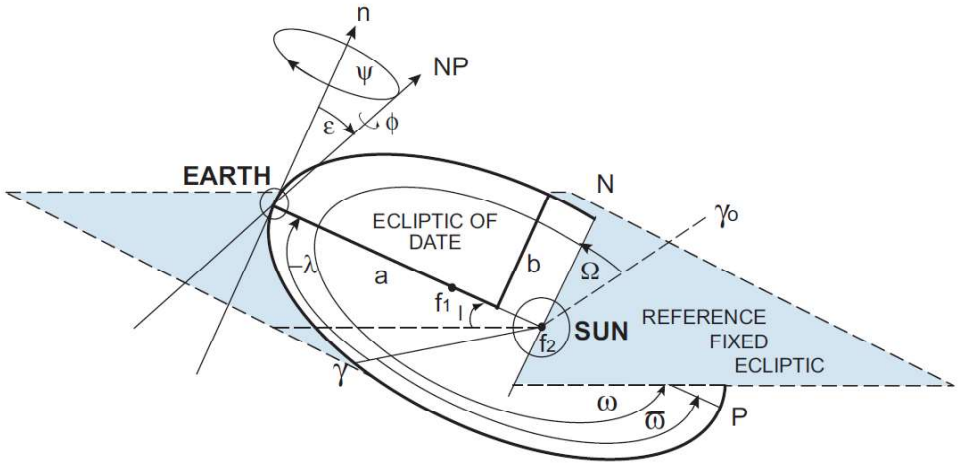


Figure 6: Representation of the elliptical Earth's orbital plane and the astronomical parameters. The

Sun occupies one of the two foci, represented by $\boldsymbol{f_1}$ and $\boldsymbol{f_2}$**.** Parameters **a** and **b** are the semi-major axis and the semi-minor axis, respectively. The plane of the Earth's orbit is inclined at an angle of **I** relative to a plane identified as the fixed reference ecliptic. Axis **n** is the normal to the orbital plan and **NP** is Earth's rotation axis, "North Pole". The point **N** is called "ascending node" and represents the point where orbital and reference ecliptic intersects, with an angle of **Ω** relative to a fixed vernal point $\boldsymbol{\gamma_0}$. **P** represents the orbital perihelion relative to $\boldsymbol{\gamma_0}$. **ω** is the argument of the perihelion, which measures the angular distance between **P** and **N.** $\boldsymbol{\gamma}$ is a moving vernal point which moves clockwise along the orbit due to the precession of the equinoxes **ψ,** going at an angle **ϖ = Π + ψ. ϕ** is the Earth's counterclockwise rotation rate, and ε is the obliquity of the ecliptic that precesses clockwise at a rate **ψ** (from Hinnov, 2013).

Some astronomical parameters can alter the intensity and duration of the receipt of solar radiation at all points on Earth. Variations in the Earth's orbit and its inclination in relation to the Sun cause changes in total, seasonal and latitudinal radiation (Hinnov, 2013). This leads to climatic cycles that occur periodically on time scales of the order of 10^4- 10^5 years (Berger, 1980), comprising the so-called Milankovitch Cycles, which are:

Eccentricity

The eccentricity of the orbit is given by the Equation 6.1 (Berger, 1980):

$$e = \frac{(a^2 - b^2)^{\frac{1}{2}}}{a} \tag{6.1}$$

where a is the semi-major axis and b is the semi-minor axis.

Equation 6.1 represents the ratio between the focal length and the semi-major axis of an ellipse. The Earth's translation varies from quasi-circular orbits (e = 0.001) to more elliptical orbits (e = 0.06) - currently, the eccentricity is estimated to be around 0.017 (Weedon, 2003). The ellipse semi-major axis a determines the size of the ellipse; the eccentricity e measures the shape of the Earth's orbit around the Sun (Berger & Loutre, 1994; Paillard, 2001); the same parameters are responsible for influencing solar heating received by the Earth (Paillard, 2001). The global mean annual radiation received by Earth from the Sun is given by Equation 6.2 (Paillard, 2001):

$$W_A = \frac{S}{4\sqrt{1-e^2}} = \frac{S_0}{4} \tag{6.2}$$

where S is the solar radiation received at a distance a from the Sun, a parameter which depends exclusively on solar activity. S_0 is defined as the solar constant. However,

variations in annual mean radiation are very small, once it depends only on the square of the eccentricity (Paillard, 2001).

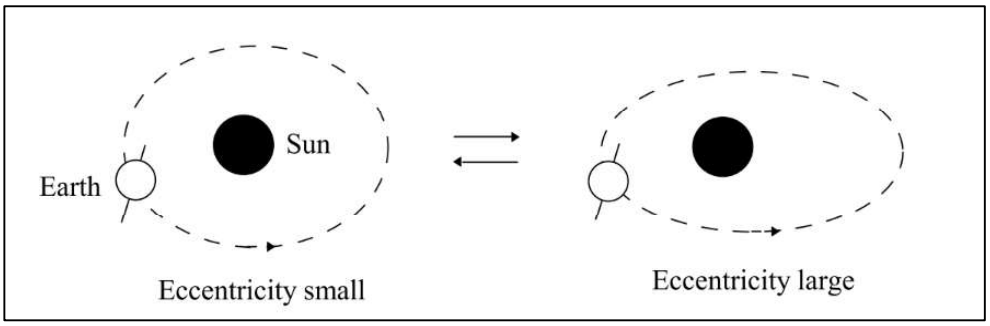


Figure 7. The variation of the orbit's eccentricity (Weedon, 2003).

The main periodicities of the eccentricity cycles are of approximately 100 Kyr and 405 Kyr, calculated over 0–40 Myr (Kodama & Hinnov, 2015; Hinnov, 2013) and practically constant throughout the planet's history (Berger *et al.*, 1992). Figure 8 shows the frequency spectrum of the eccentricity variations. The ~100 Kyr cycle modulates the amplitude of the precession cycle (Lisiecki, 2010).

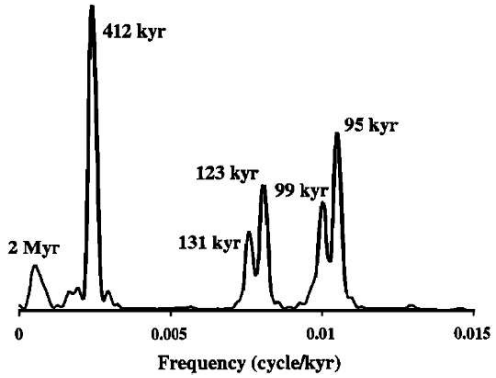


Figure 8. Spectral analysis of the eccentricity variations. Major periodicities are shown at ~400 Kyr and ~100 kyr band. The vertical linear scale is arbitrary (Paillard, 2001).

Obliquity

The obliquity of the Earth's rotational axis is the angle between this axis and the orbital plane (Fig. 9), and its variations oscillates between 22.5° and 24.5° with two amplitude modulations: a large one with a period of 1.2 Myr, originated from orbital inclination variations of Mars and Earth, and a smaller one at 2.35 Myr (Hinnov, 2013). Currently, the angle of inclination of the rotation axis is about 23°27', presenting a current period of about 41 kyr (Berger & Loutre, 2004), as is shown in Figure 10. The inclination of the axis is directly related to seasonal variations in insolation. Its variation alters the distribution of solar radiation between the equator and the poles, and their influence predominates at high latitudes (Hinnov, 2000).

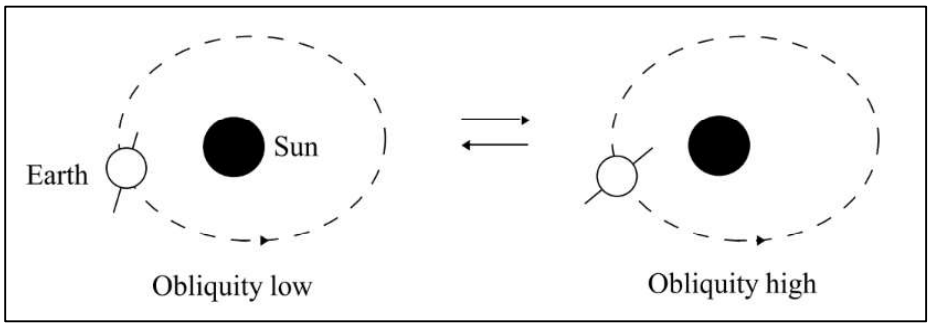


Figure 9. The variation of the angle of the tilt of the Earth's axis, relative to a direction at right angles to the ecliptic (Weedon, 2003).

Obliquity variations have an impact on the local annual mean insolation, different from what occurs with eccentricity changes. As the obliquity increases, polar regions receive more radiation in summer, which makes the annual mean insolation increases at the poles and decreases at the equator (Paillard, 2001). The angle of the tilt influences directly the amplitude of the annual or seasonal cycle, causing an imposed modulation on it (Weedon, 2003). As the tilt changes, the solar incoming radiation changes equally in both hemispheres, although the effect is maximum in high latitudes and small in the tropcs (Berger & Loutre, 2004).

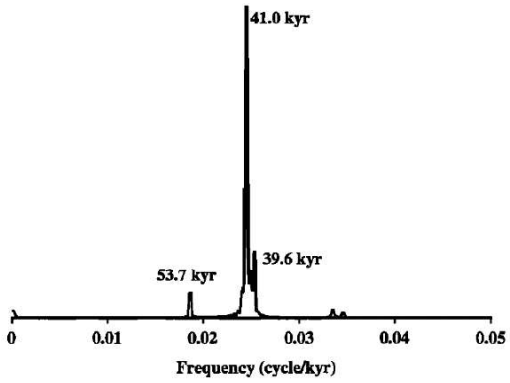


Figure 10. Spectral analysis of the obliquity variations. Major periodicity is shown at 41 kyr. The vertical linear scale is arbitrary (Paillard, 2001).

Precession

Precession comprises two distinct parameters: axial precession (Fig. 11.a) and apsidal precession (Fig 11b). The first one is the "pawn" type movement, which is caused by the effect of lunar and solar attraction on the equatorial region of the planet (Berger & Loutre, 1994). This one movement shifts the equinox and solstice positions in relation to perihelion and aphelion, through the rotation of the Earth's tilt (Weedon, 2003; Berger & Loutre, 1994). Its current periodicity is 26 kyr, in a clockwise direction considering a North Pole down view (Weedon, 2003).

Apsidal precession refers to the counterclockwise movement of the major semi-axis rotation of the Earth's orbit, measured related to the stars. Its current periodicity is approximately 100 kyr, the same as the eccentricity (Berger & Loutre, 2004).

The two effects combined result in the “climatic precession” of the equinoxes, with a mean period of 21 kyr, which is the result of four largest terms with periodicities of 23.716, 22.428, 18.976 and 19.155 kyr (Berger & Loutre, 2004; Berger, 1977b), as shown in Figure 12.

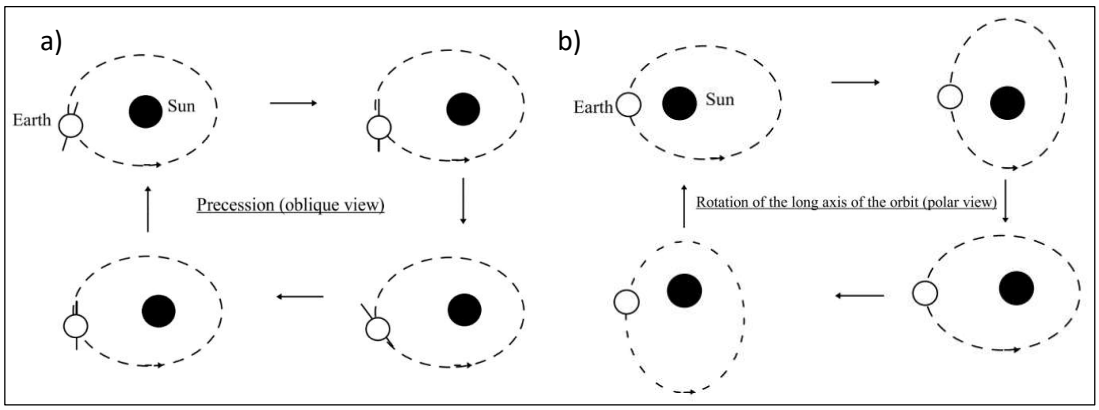


Figure 11. Two factors control the climatic precession: (a) the rotation of the direction of tilt of the Earth’s axis; (b) the rotation of the long axis of the Earth’s orbit (modified from Weedon, 2003).

The precession movement does not cause variation in the annual total insolation, as the hotter days near perihelion are balanced with cooler days near aphelion. At medium-to-high latitudes, the climate evolves as follows: (a) medium summer and winter, (b) short hot summer and long cold winter, (c) medium summer and winter and (d) long warm summer and short cold winter (Weedon, 2003).

The climatic precession cycles control most of the long-term variations of daily insolation. However, the precession cycles are modulated by the eccentricity in terms of amplitudes and frequency, and the Earth is reaching the minimum of the 400 kyr eccentricity cycle, which causes insolation to present small variations in amplitude over the last tens to thousands of years (Berger *et al.*, 1993; Berger & Loutre, 2004).

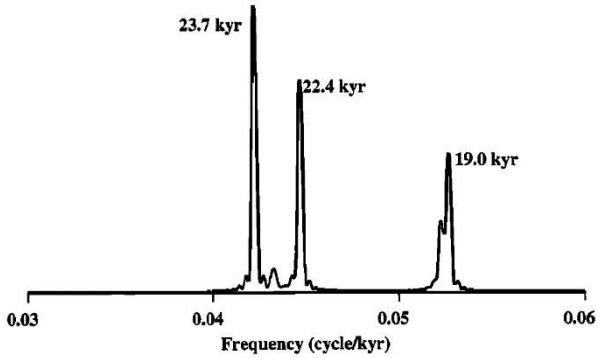


Figure 12. Spectral analysis of the precession variations. Two groups of periodicities are shown, around 23 and 19 kyr. The vertical linear scale is arbitrary (Paillard, 2001).

4.3 The Astronomical Time Scale and its contributions to chronostratigraphic problems

The theory of Milankovitch Cycles is well accepted nowadays, and astronomical forcing signals recorded in cyclostratigraphy can be exploited as a geochronometer, by astronomical signal's quantification and their integration into the global cyclostratigraphy framework. Cyclostratigraphic analyses allows intervals without radioisotope dating to be restored, validated and enhanced with high precision chronology, and astrochronology has become an important tool in Geosciences (Hinnov, 2013).

The Astronomical Time Scale is based on the stratigraphy forced by the cycles of Milankovitch and is very well defined for the Cenozoic and Mesozoic; however, an ATS was not much explored for the Paleozoic era due to the lack of high-precision geochronology (Wu *et al.*, 2012; Wu *et al.*, 2013). Astronomical calibration consists of the procedure of adjusting the time scale of a sedimentary succession to the Milankovitch cycles through the analysis of the proportionality relation of the peaks of a power spectrum (Kruiver *et al.*, 2000; Franco, 2007), assuming sufficient stability of planetary movements through the time to the extent of being identified in the geological age of the data (Hinnov & Hilgen, 2012).

The quality of the results generated by astrochronology depends on the correct identification of the astronomical signals in the record and on the data used to adjust the age (Hinnov, 2013). Another important point is that the recognition of the wavelengths of the Milankovitch Cycles by means of astronomical model solutions is very accurate up to 60 Ma. For older periods, uncertainty increases due to the chaotic movements of the solar system (Laskar, 2008; Dinarès-Turell *et al.*, 2014). As the focus of this dissertation is the Miocene, there will be no problems related to this fact.

Recent advances in the study of forced orbital signals have allowed more accurate results with a better correlation between orbital movements and stratigraphic records. These new insights enable the application of the theory of orbital variations in areas such as geochronology, geodynamics, and astrodynamics (Hinnov, 2000). From the identification of well-preserved astronomical cycles in the stratigraphic record, it is possible to understand the evolution of the Earth System processes and to develop an optimal model for climatic changes and depositional system responses (Meyers, 2019; von der Heydt *et al.*, 2021). The application

in geochronology includes the improvement of the accuracy and resolution of time-stratigraphic frameworks (Meyers, 2019; Hilgen *et al.*, 2004; Strasser *et al.*, 2006). Fundamental problems in Earth Sciences can also be untangled with a high-resolution time scale, such as the level of the chaotic behavior of Solar System (Hinnov, 2000). The combination of orbital forcing estimated from upper Permian marine sections with multiple radioisotopic ages give rise to an important step to construct the ATS through the Palaeozoic (Hilgen *et al.*, 2015).

Chapter 5

Data and Methods

5.1 Data acquisition

3D seismic lines, well logging gamma ray data and biostratigraphic data were provided by ANP. Wells were selected based on seismic interpretation, prioritizing those free of major faults, gas-related disturbances, and significant erosional truncation, and located near the three wells analyzed by Santos *et al.* (2023). The gamma-ray logs have a resolution of 0.2 m.

The intensity of gamma-ray emitted by radioactive elements in sedimentary rocks is related to the amount of ^{40}K, ^{232}Th and ^{238}U, and is recorded in natural gamma-ray logging (Wu *et al.*, 2009). If the sediments are rich in clay, the GR logging data shows high values; if the sediments are quartz-rich sandstone or carbonate rich deposits, the GR logging data shows lower values (Li *et al.*, 2019a; Gong, 2021; Wu *et al.*, 2013). The correlation between GR and the relative abundance of clay turns GR logs into a valuable instrument for paleoclimate and climatic cycles analysis. As sediment content is affected by climatic variations, GR can be used as a physical proxy in cyclostratigraphy analysis to provide measurements that reflect astronomical forcing (Huang, 2020; Li *et al.*, 2019a).

5.2 INPEFA

The Integrated Prediction Error Analysis (INPEFA) curve offers an alternative approach for identifying trends and patterns that are not readily apparent in the original log data, thereby helping to define the structural context of the evolved sequence stratigraphic framework (Nainggolan & Winardhi, 2019; Nio *et al.*, 2005). This procedure starts with an auto regressive calculation from input data (GR curve), deriving the estimated value of maximum entropy spectrum analysis (MESA). The calculated Prediction Error Filter Analysis (PEFA) is then obtained by subtracting the predicted value from the original input (RV) of the logging curve (PEFA = RV – MESA) (Li *et al.*, 2023; Nainggolan & Winardhi, 2019).

The following equation mathematically describes how PEFA is obtained:

$$e_i = x_i - \hat{x}_i = x_i - \sum_{k=1}^{m} C_k x_{i-k}, \qquad i = m+1, \ldots, N$$

In the equation above, e_i is the output filter, called Prediction Error Filter Analysis; x_i is the actual value of the data at the position i, $\hat{x}_i$ is the value predicted by the autoregressive filter, and C_k are the prediction coefficients, determined from previous data. High-magnitude positive or negative values indicate potential stratigraphic discontinuities or cycle boundaries, while spikes of varying sizes correspond to isochronous interfaces at different scales (Nio *et al.*, 2005; Li *et al.*, 2023; Yuan *et al.*, 2018). The coefficient error filter C_k were determined using a least squares approach, in a process known as the Burg algorithm, which is used to optimize the prediction results (Nainggolan, 2019; Qayyum & Smith, 2014).

In order to obtain the synthetic INPEFA curve, the PEFA curve must be integrated. The INPEFA curve captures cumulative variations derived from the integrated PEFA signal, emphasizing directional shifts in the data. Intervals dominated by negative prediction errors exhibit downward (up-to-the-left) trends, while those with predominantly positive errors display upward (up-to-the-right) trends. Smaller-scale trends are superimposed on broader ones, as commonly seen in stratigraphic data (Nio *et al.*, 2005).

A key aspect of this approach is the identification of INPEFA inflection points, which mark changes in the overall trend. Transitions from positive to negative trends are interpreted as an increase in sand supply. These variations are considered potential indicators of stratigraphic discontinuities and reflect significant changes in the depositional regime, potentially driven by climatic influences. In particular, shifts toward a positive trend indicate a reduction or interruption of sediment input and are commonly associated with base-level changes linked to climate variability (Nio *et al.*, 2005; Qayyum and Smith, 2014).

In this study, INPEFA was used to detect inflection points in the signal that may indicate base-level variations and/or shifts in depositional regimes, potentially linked to climate-driven processes (Nio *et al.*, 2005; Qayyum & Smith, 2014). Integrating these INPEFA-derived features with lithological information, Evolutionary Harmonic Analysis (EHA) results, and seismic interpretation allowed the identification of erosional events and changes in depositional regimes, improving the understanding of depositional system dynamics.

5.3 Cyclostratigraphic analysis

5.3.1 Time-series analysis

A sedimentary sequence constituted by successive beds in a particular order, under some conditions, could be used to generate time series. These conditions are: 1) consistent environmental conditions, 2) unambiguous relationship between the variable recorded and some changing aspect of the environment, and 3) thickness–time relationship (Weedon, 2003). As oscillating systems are responsible for producing sedimentary cycles, time series data can be arranged in a new frequency-based configuration through the application of Fourier Transform (Schwarzacher, 1975; Kodama & Hinnov, 2015).

The time-series analysis was developed in Acycle version 2.8 software, a software package designed for the analysis of time series data within the field of paleoclimate research and educational purposes (Li *et al.*, 2019b). The six GR datasets underwent removal of null values. Interpolation function was used to generate uniformly spaced time series, as data might typically present irregular spacing (0.2 m for wells 1-RJS-297, 4-RJS-330A, 3-AB-68, 1-RJS-342 and 1-RJS-305, 0.025 m for well 3-AB-92). The detrending function with LOESS method was then applied to remove secular irregular trends with high amplitudes, with a 400 m window, as this window length eliminated spectral power associated with frequencies below the long-eccentricity band.

The power spectrum was evaluated using the multi-taper method (MTM, Thomson, 1982) approach, a method in which the time series is tapered using discrete prolate spheroidal sequences (DPSS), or Slepian sequences, before applying the Fourier Transform. DPSS are sets of independent functions highly effective in reducing periodogram leakage. The method aims to provide a spectrum that combines smaller side lobes while still achieving high frequency resolution (Weedon, 2003; Kodama & Hinnov, 2015).

The MTM approach was applied using the robust first-order autoregressive (AR (1)) red-noise model; which considers the processes “memory”, where previous behavior influences present behavior. The background noise identification through a statistical model leads to a confidence level estimation of the periodic peaks found, calculated at 90%, 95% and 99% confidence levels (Li *et al.*, 2019b; Kodama & Hinnov, 2015).

5.3.2 Evolutionary power spectral analysis

Sedimentation rate may not remain constant throughout the entire time series, exhibiting variations either with depth or over time, as gaps in records, erosional occurrences

and unequal sediment accumulation rates affect all stratigraphic data series (Meyers *et al.*, 2001, Kodama & Hinnov, 2015). It is possible to investigate the impact that these processes had on data series and to analyze the sedimentation rate variations by applying the Evolutive harmonic analysis (EHA) procedure, (Meyers *et al.*, 2001). If the duration of the time series exceeds the cyclical pattern of interest, power spectra can be created by calculating the spectra of many portions of data, using a moving window that tracks the entire data series (Weedon, 2003; Kodama & Hinnov, 2015). In this study, EHA was performed with the Evolutionary Fast Fourier transform (eFFT) LAH method (Kodama & Hinnov, 2015), with a 250 m for wells 3-AB-92 and 1-RJS-342, 350 m for wells 1-RJS-305 and 3-AB-68, 451.44 m for well 1-RJS-297, and 377 m for well 4-RJS-330A.

5.3.3 Definition and filtering of orbital frequency bands

Using the MTM and EHA results, spectral bands associated with Milankovitch cyclicity were identified through analysis of frequency ratios for the Miocene interval. The expected peak ratios were calculated for 14 Ma (mean Miocene age) yielding approximate values of 405:125:95:40.5:23.6:19.1 kyr, or normalized as 21.2:6.5:5.0:2.1:1.2:1.0 (Laskar *et al.*, 2004).

In paleoclimate analysis, filters are essential tools for isolating specific frequency components within time-series data, allowing the identification of periodic signals associated with orbital forcing. By removing noise and non-relevant frequency ranges, filtering techniques enhance the detection and interpretation of climatically driven cycles preserved in geological records (Li *et al.*, 2019b; Weedon, 2003). In this study, the bandpass-filtering function available in the Acycle 2.8 software was applied to isolate frequency bands corresponding to long and short eccentricity cycles. This approach enables a more robust identification of orbital-scale variability, improving the reliability of cyclostratigraphic interpretations.

5.3.4 Correlation Coefficients analysis (COCO and eCOCO)

Subsequently, the correlation coefficient (COCO) method was employed to evaluate the relationship between the astronomical solution in the time domain and the power spectra derived from the proxy data in the depth domain, across a range of sedimentation rates. The optimal sedimentation rate is inferred from the highest correlation values (Li *et al.*, 2018,

2019b). Additionally, the evolutionary correlation coefficient (eCOCO) approach was applied to assess temporal variations in sediment accumulation rates using a sliding window along the data series.

The COCO/eCOCO analysis was performed by considering a sedimentation rate range of 2.6 to 100 cm/kyr, with step of 0.33 cm/kyr, incorporating 2000 Monte Carlo simulations and a sliding window of 250 m. The target astronomical solutions are from the La2004 solution for a middle data age of 14 Ma. COCO calculations were conducted using the raw power spectra of the GR series after removing the AR(1) background. Furthermore, the null hypothesis of no orbital forcing (H_0) was tested to evaluate the probability that the observed correlation coefficients could arise by chance.

5.4 Seismic data and RGT

Seismic horizon mapping and integration with biostratigraphic data were carried out using Paleoscan™ software on depth-domain datasets. Because no seismic lines directly intersect the wells selected for cyclostratigraphic analysis, a two-dimensional (2D) section was constructed by interpolating the three-dimensional (3D) seismic volume. This section was then used to identify seismic reflectors and erosional surfaces based on reflector terminations, including upper terminations (erosional truncations, toplaps, and conformable terminations) and lower terminations (onlaps, downlaps, and conformable terminations), supporting correlation with the cyclostratigraphic interpretations derived from well data. The presence of chaotic seismic facies also helped identifying the erosional surface. Seismic reflectors, interpreted as well-defined progradational depositional surfaces associated with shallow marine environments, provided key geometries for establishing stratigraphic correlation between the wells.

A seismic resolution analysis following Widess (1973) was performed to improve depth alignment of seismic horizons. This approach quantified depth-related uncertainties and supported adjustments to horizon positions within the wells. The vertical resolution of the seismic reflectors is ~20 m, implying possible offsets of up to ±10 m from their original position.

The Relative Geological Time (RGT) concept was introduced and further developed by Stark (2003; 2004; 2005a; 2005b; 2006). RGT volumes are derived from the correlation of seismic traces; RGT images retain the same spatial dimensions as the original seismic data. They allow seismic horizons to be identified and extracted by following surfaces of constant RGT, effectively treating reflectors as time-equivalent depositional surfaces (Qayyum *et al.*, 2017). Structural

elements such as faults and unconformities are implicitly embedded within the RGT framework, which, when properly constructed, supports the interpretation of key geological features, including horizons, faults, and unconformities (Geng *et al.*, 2020).

Seismic attributes represent quantitative descriptors of geometric, kinematic, dynamic, or statistical properties extracted from seismic data through calculation or interpretation (Liner *et al.*, 2004; Chen & Sidney, 1997). Among these, the root mean square (RMS) amplitude measures the magnitude of seismic amplitudes within a defined time or depth window and is commonly used to highlight anomalously high-amplitude zones. This attribute is particularly useful for detecting lithological contrasts and features such as channels or gas-bearing sands (Bashir *et al.*, 2024a,b).

In this study, the RGT framework was integrated with RMS amplitude analysis across the seismic dataset covering the six wells in the Albacora Oilfield. This integration enabled the extraction of RGT slices tied to key seismic horizons, providing a basis for subsequent analyses.

Chapter 6

Manuscript: "ARCHITECTURE-DRIVEN ORBITAL RECORDS IN A CONTINENTAL MARGIN: CYCLOSTRATIGRAPHIC–SEISMIC INSIGHTS FROM THE MIOCENE ALBACORA OILFIELD (CAMPOS BASIN, BRAZIL)"

The results of this dissertation are presented in the form of a scientific article submitted to the peer-reviewed international journal *Marine Geology*. The study presents the first systematic assessment of how lateral variations in stratigraphic completeness across different marine depositional environments influence cyclostratigraphic interpretations and geological time estimates. Since cyclostratigraphic analyses based solely on isolated well-logs rarely consider lateral changes in stratigraphic preservation, estimates of depositional duration are commonly affected by incomplete sedimentary records. To overcome this limitation, Miocene deposits from the Albacora Oilfield (Campos Basin, Brazil) were investigated through an integrated framework combining cyclostratigraphy, seismic stratigraphy, Integrated Prediction Error Filter Analysis (INPEFA), and Relative Geological Time (RGT) modeling across six wells distributed along two dip-oriented sections and one strike-oriented section. By integrating well-log data with seismic-supported stratigraphic correlations, the study demonstrates that isolated well records tend to underestimate depositional timespans due to stratigraphic incompleteness related to progradation, diachronous preservation, and depositional hiatuses.

ARCHITECTURE-DRIVEN ORBITAL RECORDS IN A CONTINENTAL MARGIN: CYCLOSTRATIGRAPHIC–SEISMIC INSIGHTS FROM THE MIOCENE ALBACORA OILFIELD (CAMPOS BASIN, BRAZIL)

Mariana Aragão Fernandes[1*], Natália Braun dos Santos[1], Daniel Ribeiro Franco[1], Ciro Climaco Rodrigues[2], Mateus Fontana Michelon[2], Mingsong Li[3], Daniel Galvão Carnier Fragoso[2], Paulo Sérgio Gomes Paim[4], Mariane Candido[1], Carolina Gonçalves Leandro[1,5], Gabriella Fazio[1,6], Raysa

de Magalhães Rocha[1,5], Lucio Riogi Tokutake[2], Ana Natalia Gomes Rodrigues[2]

[1] Coordenação de Geofísica, Observatório Nacional, Rio de Janeiro, Brasil;

[2] Petrobras, Rio de Janeiro, Brasil;

[3] Key Laboratory of Orogenic Belts and Crustal Evolution, MOE, School of Earth and Space Sciences, Peking University, Beijing, China;

[4] Programa de Pós-Graduacao em Geologia, Universidade Federal do Paraná;

[5] Instituto de Geociências, Universidade Federal do Rio Grande do Sul, Porto Alegre, Brazil

[6] Centro de Tecnologia Mineral, Rio de Janeiro, Brasil;

[*]E-mail: marianafernandes@on.br

ABSTRACT

Cyclostratigraphic studies based on isolated well-logs rarely account for the lateral variability of stratigraphic preservation, limiting the reliability of geological timespan estimates. We address this problem through the investigation of Miocene deposits in the Albacora Oilfield (Campos Basin, Brazil), using an integrated approach comprising cyclostratigraphy, seismic stratigraphy, Integrated Prediction Error Filter Analysis (INPEFA), and the Relative Geological Time (RGT) model across six wells along two dip and one strike sections. Spectral analyses reveal significant peaks, most of which exceed the 95-99% confidence levels, consistent with expected orbital ratios for 14 Ma, with long- and short-eccentricity wavelengths of ~145 m and ~47 m. Correlation coefficient derived sedimentation rates (30.0-45.4 cm/kyr) supporting orbital forcing. Seismic stratigraphy indicates a predominantly progradational system, with preferential preservation in the mid-slope region, where thicker successions and up to three Long-eccentricity cycles are observed, compared to a single cycle in shelf and base-of-slope settings. The RGT model highlights along-strike sedimentation rate variability, while INPEFA identifies key stratigraphic surfaces associated with hiatuses and erosional processes. Taken together, these results show that stratigraphic completeness cannot be assessed from isolated well-logs and that seismic-constrained multi-well correlation is essential for robust cyclostratigraphic interpretations. To our knowledge, this is the first study to systematically examine the lateral preservation of astronomical cycles within a seismic volume as a function of depositional architecture, and to show how properly accounting for this preservation reshapes estimates of geological time.

Keywords: Cyclostratigraphy; Seismic stratigraphy; Chronostratigraphic framework;

Stratigraphic preservation; Milankovitch Cycles.

1. Introduction

Stratigraphic analyses inherently involve complex spatial and temporal assessments, making the accurate interpretation of both the sedimentary record and its depositional timing a central methodological challenge. Multi-well cyclostratigraphic studies integrated with seismic interpretation and independent geochronological constraints offer a means to overcome these limitations, enabling more robust chronostratigraphic frameworks and a more faithful reconstruction of depositional dynamics across broader areas. Santos *et al.* (2023) demonstrated the applicability of this integrated approach in a deep-water setting, proposing a high-resolution 2D chronostratigraphic framework for the southern sector of the Albacora Oilfield (Campos Basin, Brazil) through the integration of cyclostratigraphy, biostratigraphy, and seismic interpretation using gamma-ray (GR) logs from three wells. Their results revealed orbital control on sedimentation, constrained the ages for the deposits, and linked the analysed Miocene interval to the Miocene Climatic Optimum.

The Campos Basin, one of the most productive oil and gas-producing sedimentary basins along the Brazilian margin, has been the focus of numerous geological studies; however, relatively few have incorporated a cyclostratigraphic perspective (e.g., Castro, 2005; Filho & Perlmutter, 2005; Santos *et al.*, 2023). Among the basin's key exploratory areas, the Albacora Oilfield stands out as one of the most significant hydrocarbon provinces (De Gasperi & Catuneanu, 2014). Owing to its economic importance, the field is characterised by an extensive dataset of seismic and well-log data (ANP, 2018), providing an excellent opportunity for a multidisciplinary approach and a more comprehensive understanding of its stratigraphic framework and depositional evolution.

Recently, additional higher-resolution 3D seismic data for the Albacora Oilfield were made available by Brazilian National Agency for Petroleum, Natural Gas and Biofuels (ANP), enabling a reevaluation and expansion of the chronostratigraphic framework proposed by Santos *et al.* (2023). Such reevaluation is particularly relevant for refining the chronostratigraphic framework of the field, as higher-resolution seismic data allow a more accurate identification of key stratigraphic surfaces, depositional stacking patterns, and lateral variability of stratigraphic preservation, ultimately leading to a better understanding of the sedimentary evolution of the Albacora system. Therefore, we present a revised and extended chronostratigraphic interpretation of the Miocene section of the Albacora Oilfield based on three stratigraphic sections integrating six GR well-log datasets and seismic data: a strike section

linking the dip section previously investigated by Santos *et al.* (2023), and a northernmost dip section incorporating two additional wells. Taken together, these sections provide the basis for a chronostratigraphic framework spanning approximately 62 km².

Compared to the earlier study, the availability of higher-resolution seismic data - together with the expanded well dataset and the integration of cyclostratigraphic results with Relative Geological Time (RGT) volumes and Integrated Prediction Error Filter Analysis (INPEFA) - represents a substantial advance. Derived from the correlation of seismic traces, RGT volumes allow seismic reflectors to be represented as laterally continuous depositional surfaces, thereby facilitating the recognition of major geological features, including horizons, faults, and unconformities. Meanwhile, the INPEFA technique provides a numerical means of emphasizing cumulative and directional trends within the dataset. This integrated approach enabled a more detailed investigation of stratigraphic preservation, accounting for both lateral and vertical variability, and allowed the identification of areas with better-preserved successions, more robust stratigraphic correlations, and a more refined understanding of the timescales involved in depositional processes.

2. Geological settings

2.1. Campos Basin

The Campos Basin is a divergent margin-type basin located at the East Brazilian Margin (southeastern Brazil), and it extends from the northern coast of the State of Rio de Janeiro to the southern portion of the State of Espírito Santo. It is bounded to the north by the Vitória High, to the south by the Cabo Frio High. Its extension is about 100,000 km² (De Gasperi & Catuneanu, 2014; Castro & Picolini, 2015; Figueiredo Jr. *et al.*, 2015).

The sedimentary evolution of the Campos Basin is related to the rifting process of the Gondwana supercontinent and the subsequent opening of the Atlantic Ocean; the most accepted interpretation for the opening is lithospheric stretching, crustal thinning (McKenzie, 1978) and subsequently a thermal anomaly (Royden & Keen, 1980) with associated subsidence. According to Winter *et al.* (2007), the Campos Basin stratigraphy can be divided into three large-scale tectono-sedimentary units, also called megasequences: (1) Rift or continental, formed under mechanical subsidence regime and characterized by direct control of the basement structural framework and continental sedimentation dominated by siliciclastic deposits and lacustrine coquinas (Guardado *et al.*, 1989; De Gasperi & Catuneanu, 2014). It is represented by rocks of the Cabiúnas Formation and the Lagoa Feia Group. (2) Post-rift or transitional:

represents an intermediate phase between thermal and mechanical subsidence, when continental and marine sedimentation took place; and corresponds to the upper part of the Lagoa Feia Group, which was deposited during the Aptian (Guardado *et al.*, 1989). (3) Drift or marine: formed by the deposition of the Macaé and Campos Groups, which comprises sedimentary successions ranging from the Albian to the Holocene (Winter *et al.*, 2007). This sequence consists of marine sediments deposited under a stationary thermal subsidence regime (De Gasperi & Catuneanu, 2014) and includes the Miocene deposits comprised by the Albacora Oilfield, the target of our study.

2.2. Study Area - Albacora Oilfield: dip and strike sections and seismic profiles

The Albacora Oilfield was discovered in the 1980s during a well drilling campaign (Bastos & Bastos, 2017). It is located approximately 110 km from Cabo de São Tomé, in the northeastern part of the Campos Basin, in a present-day continental slope setting; water depths range from 100 to 1,050 m (De Gasperi & Catuneanu, 2014). Albacora hosts the second-largest oil and gas accumulation in Brazil, surpassed only by the Marlim Field, also situated in deep waters of the Campos Basin. The reservoir system extends over an area of approximately 235 km^2 and comprises an original in-place volume of 711.9 × 10^6 m^3 of oil and 67.8 × 10^6 m^3 of associated gas. During the drift phase of the Campos Basin, Upper Cretaceous to Paleogene turbiditic systems account for the majority of hydrocarbon production. A considerable fraction of the hydrocarbons is produced from Oligocene-Miocene turbiditic sandstones in the Albacora Oilfield, which were deposited in response to relative sea-level falls. These events, originally outlined by Vail *et al.* (1977), took place between the Late Oligocene and the Early Miocene (Bastos & Bastos, 2017; Cândido, 1990; de Souza Cruz *et al.*, 1987).

As previously discussed, Santos *et al.* (2023) established the first published framework integrating seismic interpretation with cyclostratigraphic analyses in the Albacora Oilfield. Using gamma-ray logs from three wells in the southern sector – provided by ANP – alongside 3D seismic data, that study identified seismic reflectors and erosional surfaces along a dip-oriented transect (line A-A'), recognized orbital cycles, dated stratigraphic columns, and estimated sedimentation rates.

Building on this framework, the present study extends the investigation northward and into the central sector by incorporating three additional wells located in the northern and central portions of the Albacora Oilfield (Fig. 1; Table 1), near the slope break. It allowed us to provide a cyclostratigraphy-based, 3-D chronostratigraphic framework containing six wells and distributed in two dip- and one strike-oriented transect lines, encompassing Miocene deposits

of Aquitanian, Burdigalian, and Langhian age (Fig 1; right): dip line A-A'(comprising the same wells analysed by Santos *et al.*, 2023: wells 1-RJS-297, 4-RJS-330A, and 3-AB-68, spaced 2,384 m and 4,939 m apart, respectively); northern dip line C-C' (comprising the wells 3-AB-92 (landward sector) and 1-RJS-342 (seaward, outer shelf), spaced 5,653 m apart; and strike line B-B' (wells 3-AB-92, 1-RJS-305 (central sector) and 3-AB-68; with inter-well distances of 5,772 m and 5,167 m, respectively). The overarching goal is to treat the northern (C-C'), central (B-B'), and southern (A-A') lines as a single integrated dataset, enabling cyclostratigraphic and seismic correlation across all six wells and validating the applicability of this integrated methodology over a broader spatial domain. It is important to highlight that all three wells previously investigated by Santos *et al.* (2023) were also re-evaluated in light of the newest seismic dataset, which ensured consistency for all six investigated wells in this work.

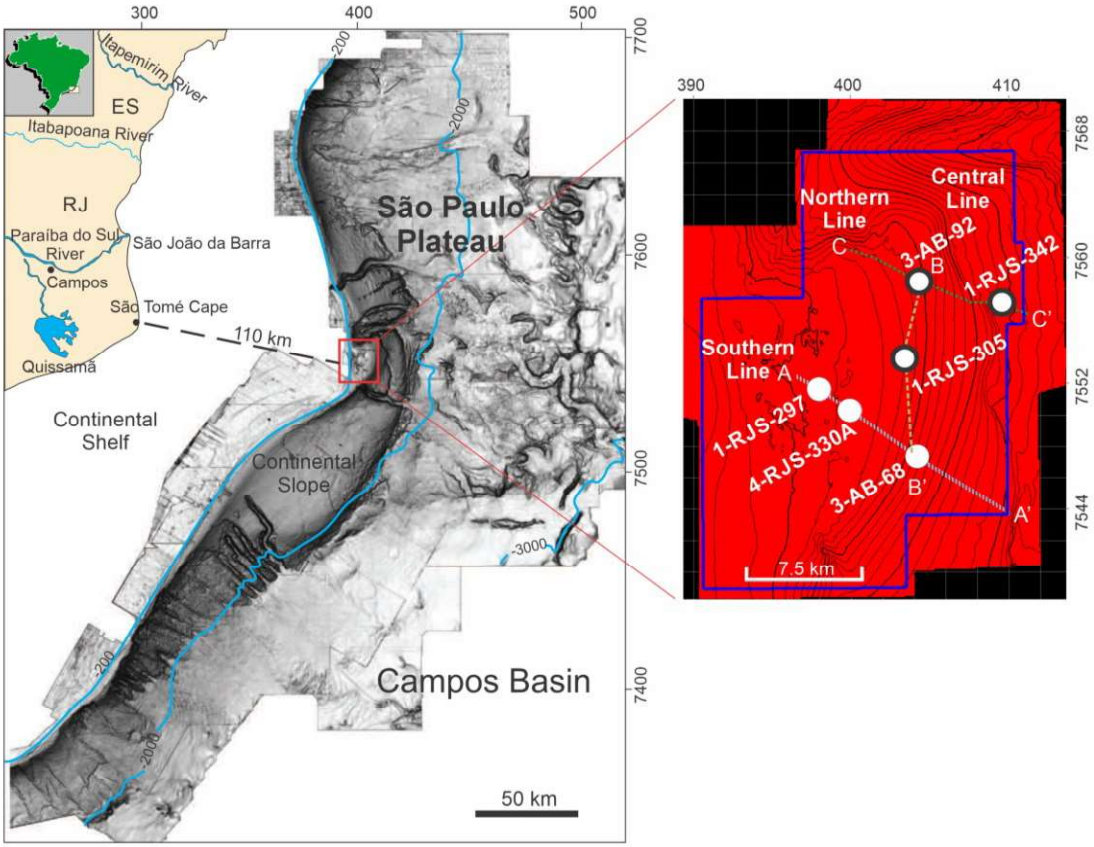


Figure 1: Left: Bathymetric and geomorphological map of the Campos Basin, highlighting the location of the study area. Right: Bathymetric map of the study area showing the wells and the Albacora Field boundary (blue polygon). The study area comprises three seismic sections: the southern dip-oriented section A–A', intersecting wells 1-RJS-297, 4-RJS-330A, and 3-AB-68; the strike-oriented section B–B', crossing wells 3-AB-92, 1-RJS-305, and 3-AB-68; and the northern dip-oriented section C–C', connecting wells 3-AB-92 and 1-RJS-342. These latter three wells were previously analyzed by Santos *et al.* (2023). Wells 3-AB-92, 1-RJS-342, and 1-RJS-305 are outlined in black and represent the newly incorporated wells used to expand the formerly analyzed area. Modified from Santos *et al.* (2023).

Table 1: *UTM coordinates, depth interval (m), and thickness of the analyzed interval (m) for each well.*

Well	Coordinates (UTM)		Depth Interval (m)		Thickness of the analyzed interval (m)
1-RJS-297	7551625.0	397943.0	802.2	3059.4	2257.2
1-RJS-305	7552641.0	403510.0	899.2	2450.0	1550.8
1-RJS-342	7557373.0	409522.0	1400.0	2350.0	950.0
4-RJS-330	7550283.0	399914.0	814.8	2699.9	1885.1
3-AB-68	7547327.9	404161.6	1612.0	3362.9	1750.9
3-AB-92	7558198.0	404530.6	1550.0	2400.0	850.0

3. Material and Methods

3.1 Gamma-ray datasets

Well logging GR data – as well as biostratigraphic data and 3D seismic lines – were provided by ANP. The selection of the most suitable wells for this work was made through seismic analysis, considering wells away from tectonic faults, gas leakage, and with no significant erosive surfaces that could compromise the stratigraphic record, as well as their proximity to the three wells originally analyzed by Santos *et al.* (2023). The resolution of the gamma-ray logs is 0.2 m.

Natural gamma-ray (GR) logs record the radiation emitted by isotopes such as ^{40}K, ^{232}Th and ^{238}U in sedimentary rocks (Wu *et al.*, 2009). The measured signal reflects the concentration of these radioactive elements: clay-rich sediments typically produce higher GR values, whereas quartz sandstone and carbonates yield lower readings (Li *et al.*, 2019a; Gong, 2021; Wu *et al.*, 2013). Because GR intensity is closely linked to clay content, these logs are widely used as proxies in paleoclimate studies and for identifying climatic cycles. As sediment composition and sea-level are influenced by climate variability, GR data can be applied in cyclostratigraphic analyses to track signals associated with astronomical forcing (Huang, 2020; Li *et al.,* 2019a).

3.2 Integrated Prediction Error Filter Analysis (INPEFA)

The INPEFA curve was employed in this study as an auxiliary tool for identifying patterns in the GR signal, as well as its inflection points. As described in the literature, these features are not easily recognizable directly in GR data series, but become more evident with the application of the INPEFA technique (Nainggolan & Winardhi, 2019; Nio *et al.*, 2005). The procedure begins with an autoregressive calculation of the input data (GR curve) to estimate the Maximum Entropy Spectrum Analysis (MESA). The Prediction Error Filter Analysis (PEFA) is obtained by subtracting the predicted values from the Raw Values (RV) (PEFA = RV − MESA) (Li *et al.*, 2023; Nainggolan & Winardhi, 2019). Integration of the PEFA yields the Integrated Prediction Error Filter Analysis (INPEFA) curve, which highlights cumulative and directional trends in the data. In this study, the average value of the GR signal was removed prior to INPEFA application in order to minimize background trends in the dataset. Intervals dominated by negative prediction errors exhibit downward (up-to-the-left) trends, while those with predominantly positive errors display upward (up-to-the-right) trends. Smaller-scale trends are superimposed on broader ones, as commonly seen in stratigraphic data (Nio *et al.*, 2005).

INPEFA inflection points represent one of the most significant features identified in this approach. Transitions from a negative to a positive trend suggest a reduction or cessation in sand supply, likely associated with base-level changes driven by climatic variations. Conversely, shifts from a positive to a negative trend indicate an increase in sand supply. These changes constitute potential stratigraphic breaks and reflect significant variations in the depositional regime, possibly linked to climate-driven processes (Nio *et al.*, 2005; Qayyum & Smith, 2014).

In this study, INPEFA analysis was applied to identify inflection points in the signal, which may reflect base-level fluctuations and/or changes in depositional regimes, potentially associated with climate-driven processes (Nio *et al.*, 2005; Qayyum & Smith, 2014). The integration of INPEFA inflection-point analysis with lithological data, Evolutionary Harmonic Analysis (EHA) patterns, and seismic interpretation enabled the recognition of erosional episodes and shifts in depositional regimes, thereby enhancing the interpretation of depositional system dynamics. The complete annotated Python script used for the INPEFA analyses is provided in the Supplementary Material S1.

3.3 Cyclostratigraphy

Cyclostratigraphic analyses were performed through the implementation of methods available in the Acycle version 2.8 software (Li *et al.*, 2019b). All six GR datasets underwent

removal of null values before linear interpolation (0.2 m for wells 1-RJS-297, 4-RJS-330A, 3-AB-68, 1-RJS-342 and 1-RJS-305, 0.025 m for well 3-AB-92) for obtaining evenly-spaced data. Detrending was performed using a LOESS (Locally Estimated Scatterplot Smoothing) regression with a 400 m window, as this window length effectively removed spectral peaks associated with frequencies lower than the long-eccentricity frequency. The power spectrum was evaluated with the multi-taper method (MTM; Thomson, 1982), using the robust first-order autoregressive (AR (1)) red-noise model, which considers the processes "memory", where previous behavior influences present behavior. The background noise identification through a statistical model leads to a confidence level estimation of the periodic peaks, calculated at 90%, 95% and 99% confidence levels (Li *et al.*, 2019b; Kodama & Hinnov, 2015). Given potential variations in sedimentation rates, the EHA was conducted using the Evolutionary Fast Fourier Transform (eFFT) LAH method (Kodama & Hinnov, 2015). Different moving-window sizes were applied to each well according to the characteristics of the data series: 250 m for wells 3-AB-92 and 1-RJS-342, 350 m for wells 1-RJS-305 and 3-AB-68, 451.44 m for well 1-RJS-297, and 377 m for well 4-RJS-330A. This approach allowed the evaluation of temporal variations in sedimentation rates along the studied intervals (Meyers *et al.*, 2001; Kodama & Hinnov, 2015). Based on these analyses, the identification of the spectral bands related to Milankovitch cyclicity was derived from the analysis of frequency ratios calculated for the Miocene interval. The expected spectral peak ratios for 14 Ma (mean Miocene age) are approximately 405:125:95:40.5:23.6:19.1 kyr, corresponding to normalized ratios of 21.2:6.5:5.0:2.1:1.2:1.0 (Laskar *et al.*, 2004). The bandpass-filtering function in the Acycle 2.8 software was used to isolate long and short-eccentricity frequency bands.

As a further step, the correlation coefficient (COCO) was applied, which is a measure of the correlation coefficient between the astronomical solution model (time domain) and the power spectra of the proxy data series (depth domain), over a range of sediment rates. The highest value of correlation coefficient probably corresponds to the most favorable sedimentation rate (Li *et al.*, 2018, 2019b). In addition, we applied the evolutionary sedimentation rate (eCOCO), which evaluates the variable sediment accumulation rates by a sliding window over the data series. The test ranged from 2.6 to 100 cm/kyr with a step of 0.33 cm/kyr, 2000 Monte Carlo simulations, and sliding window of 250 m. The COCO analyses use the raw power spectra of the GR series removing the AR (1) background spectrum. The null hypothesis of no orbital forcing (H_0) was also tested to assess the probability that the correlation coefficient could occur by chance. All parameters used for Acycle time-series analysis are provided in Supplementary Table S1, following the recommendations of Li (2026).

3.4 Seismic Data and Relative Geologic Time (RGT)

Seismic horizon mapping and biostratigraphic data integration were performed using Paleoscan™ software, based on depth-domain data. As no seismic lines directly intersect the wells selected for the cyclostratigraphic analysis, a two-dimensional (2D) seismic section was generated through interpolation of three-dimensional (3D) seismic data. This section was used to identify seismic reflectors, and erosional surfaces based on reflector terminations, including both upper (erosional truncation, toplap, and conformable) and lower (onlap, downlap, and conformable) terminations, thereby supporting correlation with well-based cyclostratigraphic interpretations. A seismic resolution analysis based on Widess (1973) was also carried out, estimating a vertical seismic resolution of approximately 20 m at the center of the interval of interest, with potential vertical offsets of up to ±10 m from the original position. It provided a higher-resolution seismic framework compared to the ~30 m seismic data used by Santos *et al.* (2023).

The RGT concept was originally introduced and subsequently expanded by Stark (2003; 2004; 2005a; 2005b; 2006). The RGT volume is generated from correlation of seismic traces. RGT images share the same spatial dimensions as seismic images and allow the identification and extraction of seismic horizons (and surfaces) by tracking constant RGT contours. The RGT, then, interprets seismic reflectors as if they were continuous depositional surfaces (snapshots of geologic times) (Qayyum *et al.*, 2017). Structural features such as faults and unconformities are implicitly represented in the RGT volume. When accurately constructed, the RGT volume enables the interpretation of key geological structures, including horizons, faults, and unconformities, within the seismic data (Geng *et al.,* 2020).

Seismic attributes are quantitative measures of geometric, kinematic, dynamic, or statistical properties derived from seismic data through direct calculation or interpretative analysis (Liner *et al.,* 2004; Chen & Sidney, 1997). Among these, the root mean square (RMS) amplitude quantifies the magnitude of seismic amplitudes within a defined time (or depth) window and is used to highlight isolated or anomalously high-amplitude responses. This attribute is widely applied to identify lithological variations and geological features, including deltaic channels and gas-bearing sands (Bashir *et al.*, 2024a, b).

The RGT model integrated with the RMS amplitude attribute was applied to the seismic data covering the area where the six wells are located in the Albacora Oilfield. This approach enabled the extraction of RGT slices corresponding to the seismic horizons required for the subsequent analyses.

4. Results

4.1 Data features and INPEFA

Gamma-ray data, lithology, seismic data, and INPEFA are presented in Fig. 2. The seismic section presented corresponds to a composite 2D line designed to intersect all analyzed wells. As the wells are distributed across three distinct alignments within the Albacora Oilfield (southern, central, and northern sectors), the section follows a non-linear trajectory rather than a single straight profile.

The lithology of the five wells is predominantly composed of interbedded marls and shales, with sandstone layers, mostly occurring below the delineated erosional surface and above the INPEFA trend marker. These sands could represent deposits formed by a mixture of turbidite-contourite systems, as these wells are located at the edge of the shelf (Mutti & Carminatti, 2012; Pandolpho *et al.*, 2021; Santos *et al.*, 2023), which indicates that there may have been an increase in energy and, consequently, mass transport. The turbidite-contourite sequence is interpreted to have developed in response to a relative sea-level fall during the middle Miocene (Pandolpho *et al.*, 2021).

In this study, the application of the INPEFA method enabled the identification of shifts in depositional regimes. The INPEFA results indicate that, below the erosional surface, the curves are predominantly characterized by trend inflections (Fig. 2). Wells 1-RJS-297, 3-AB-92, and 1-RJS-342 display a positive trend followed by a negative trend, whereas wells 3-AB-68 and 1-RJS-305 exhibit a negative-positive-negative trend pattern. Well 4-RJS-330A does not show a significant INPEFA curve below the erosional surface because the available data do not extend far below this level.

From a geological perspective, the alternation between positive and negative trends below the erosional surface indicates a stratigraphic break, possibly caused by base-level changes (Nio *et al.*, 2005; Qayyum, F., & Smith, D., 2014). Owing to the base-level fluctuations observed below the erosional surface, together with the presence of sand and diamictite lithologies in most wells beneath this interval and GR trends characterized by increasing amplitudes suggestive of higher-energy depositional conditions, cyclostratigraphic analysis of this portion may lead to uncertain interpretations. For this reason, the dataset used for cyclostratigraphic analysis was truncated at the erosional surface, and only data above this surface were considered at first. However, in the southern section, truncation significantly reduced the spectral peak amplitudes, making the identification of spectral bands more difficult. Therefore, the interval below the erosional surface was retained for the analyses in the southern

section, whereas only the data truncated at the erosional surface were considered for wells 1-RJS-342, 3-AB-92, and 1-RJS-305.

Approximately at the erosional surface, another inflection point is observed in the INPEFA curves, where the negative (sanding-up) trend changes to a positive (shaling-up) trend in all wells. Above the erosional surface, the INPEFA analysis no longer shows pronounced variations in the curves across the wells. In the upper portion of the dataset for all wells, except for well 3-AB-68, which lacks data in this interval, between approximately 1100 m and 1700 m depth, the INPEFA curves display an inflection, above which a negative trend is observed. Above this inflection point, the lithology is characterized by the presence of fine-grained siliciclastic deposits (shale and claystone) and marls, which may be interbedded with higher-energy deposits (sandstones; wells 1-RJS-297, 4-RJS-330A, and 1-RJS-305) and fine-grained carbonate deposits (calcilutite and calcisiltite; wells 1-RJS-297 and 1-RJS-305).

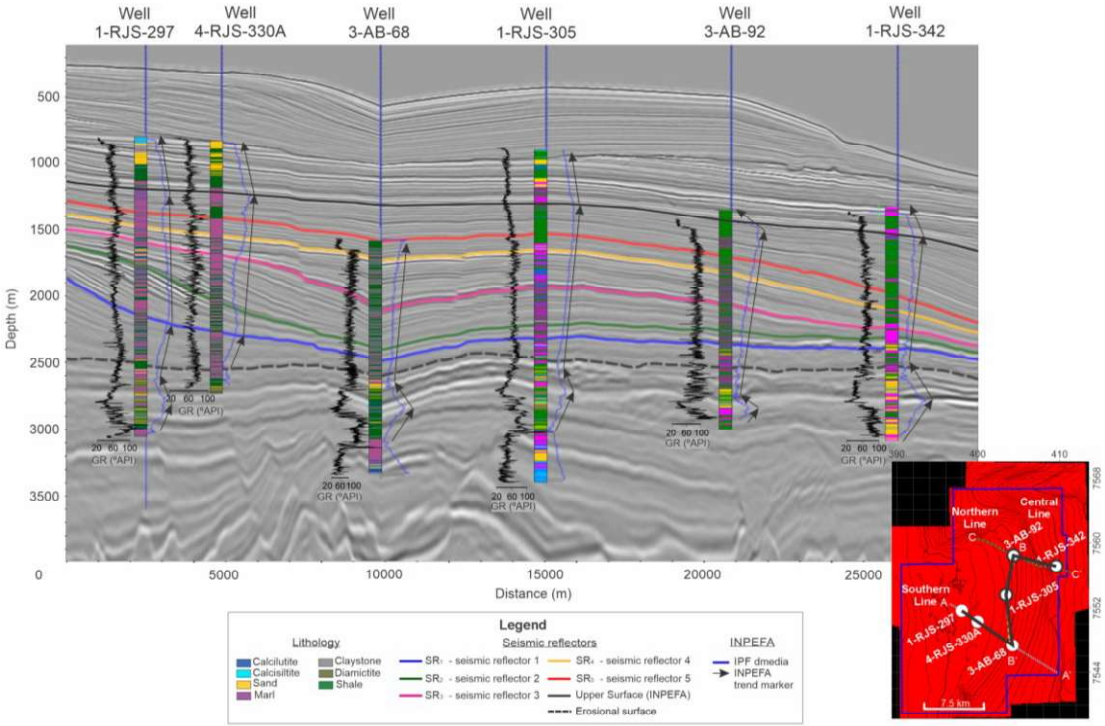


Figure 2: Seismic profile along an arbitrary section (highlighted in black on the bathymetric map) intersecting wells 1-RJS-297, 4-RJS-330A, 3-AB-68, 1-RJS-305, 3-AB-92 and 1-RJS-342, together with their corresponding raw gamma-ray (GR) logs, lithological data, and INPEFA curves.

4.2 Cyclostratigraphic analysis

Spectral analysis was performed using detrended GR data after removing intervals characterized by abrupt trend shifts. In addition to the truncation at the erosional surface

described previously, the upper portions of wells 3-AB-68, 3-AB-92 and 1-RJS-342 were truncated at 1612 m, 1550 m and 1400 m, respectively, to remove intervals exhibiting significant trend variations (see Fig. 2).

The 2π-MTM power spectra of the detrended GR series display peaks exceeding the 99% confidence level for all long (E) and short (e) eccentricity, obliquity (O), and precession (P_1 and P_2) signals across the wells. Exceptions include the obliquity signal in wells 4-RJS-330 and 3-AB-68, which exceed the 95% confidence level, and in well 3-AB-92, where obliquity was not identified above the 90% confidence level (Fig. 3). The ratios between the observed spectral peaks are consistent across wells and are presented in Table 2, together with the expected Milankovitch cycle ratios (Laskar *et al.*, 2004). Long-eccentricity peaks occur at approximately 145 m, whereas short-eccentricity peaks are observed at around 47 m.

The COCO and eCOCO analyses conducted for all wells reveal high values of correlation coefficient (ρ) and low values of significance level (H_0) associated with average sedimentation rates of 33.7 cm/kyr, ranging from 30.0 to 45.4 cm/kyr (Fig. 4). The statistical assessment indicates the influence of seven orbital parameters (405, 125, 95, 40.4, 23.5, 22.2 and 19 kyr). These results are fully consistent with our spectral interpretations across all analyzed wells.

The combined MTM and EHA analyses enabled the identification and tracking of spectral bands related to the expected Milankovitch spectral peaks ratios for the Miocene age (14 Ma, Table 2). For well 3-AB-92, the EHA shows tracks corresponding to short-eccentricity and precession that are more visible below 2000 m depth. The long-eccentricity trace, in turn, is more clearly expressed in the shallower intervals of the well (Fig. 3a). Well 1-RJS-342 exhibits a bifurcation in the EHA trace associated with the long-eccentricity cycle between approximately 1450 m and 1600 m depth. A disruption in this same long-eccentricity trend is evident between 1700 m and 1900 m for this well. Furthermore, discontinuities in the short-eccentricity signal are recognized both above 1600 m and below 2100 m depth (Fig. 3b). The same bifurcation pattern is observed in well 1-RJS-305, associated with the long-eccentricity cycle, between approximately 2200 m and 1900 m depth. For this well, the short-eccentricity signal is more apparent between 1900 and 2100 m depth, whereas the obliquity signal is more pronounced between 1000 and 1250 m and again between 1800 and 2300 m depth (Fig. 3c).

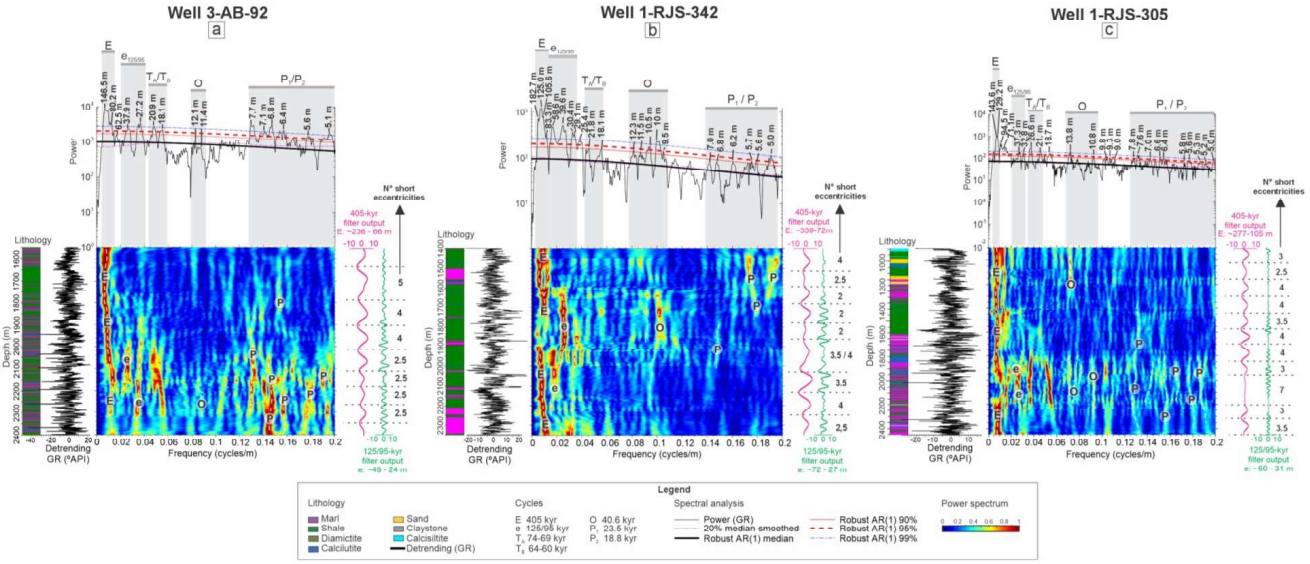


Figure 3: North section: 2π MTM power spectrum with significant peaks and defined bands for: Long-eccentricity (E), short eccentricity (e), obliquity (O) and precession (P_1/P_2/, corresponding to axial and apsidal precession); Bottom left: raw GR data, the 400-LOESS detrending data and the lithostratigraphy for all wells; Bottom right: Evolutionary Harmonic Analysis (EHA). Wells: (a) 3-AB-92 (step 1.2 m, window 250 m), (b) 1-RJS-342 (step 1.4 m, window 250 m) and (c) 1-RJS-305 (step 2.6 m, window 350 m).

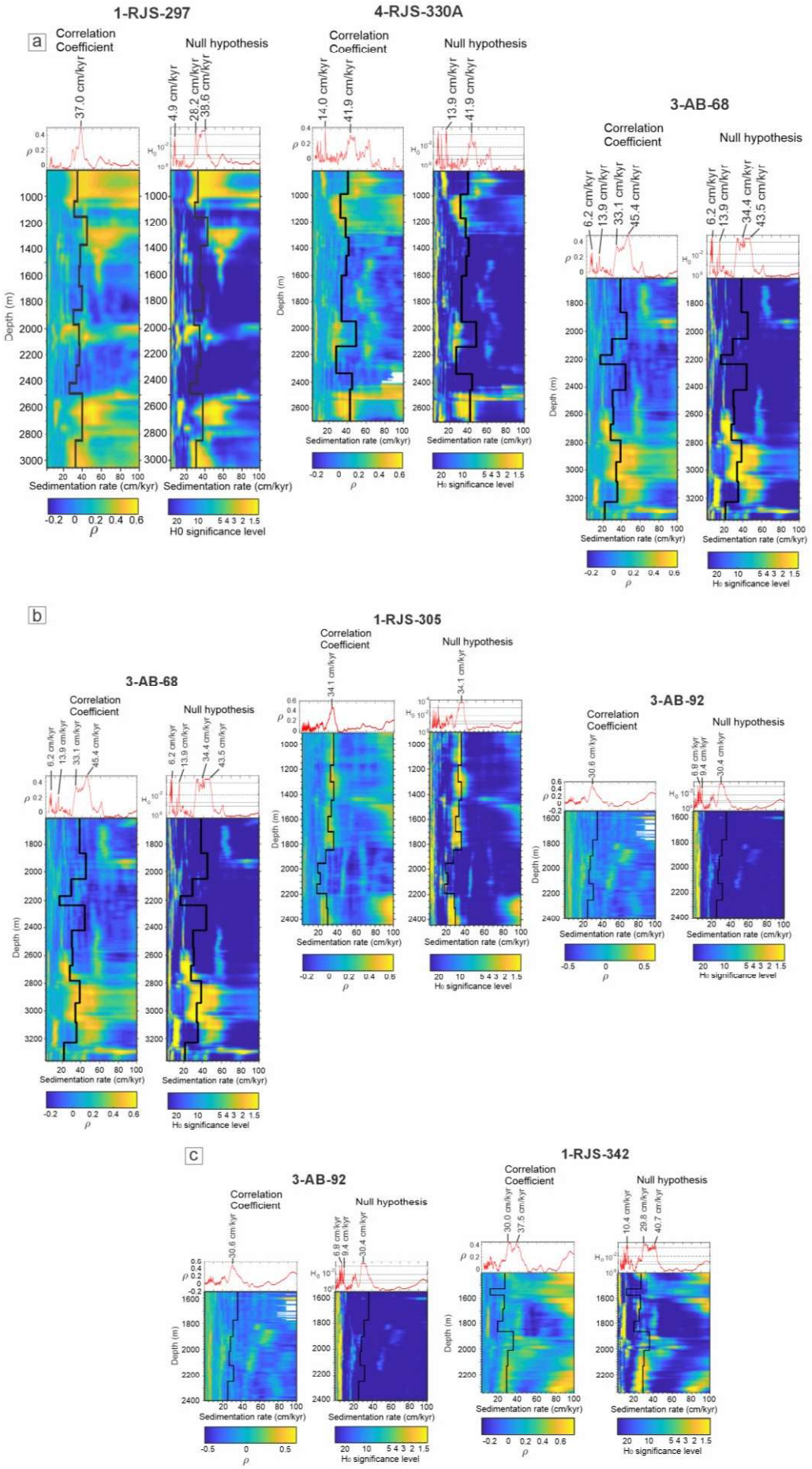

a
1-RJS-297
Correlation Coefficient
Null hypothesis
37.0 cm/kyr
4.9 cm/kyr
28.2 cm/kyr
38.6 cm/kyr
4-RJS-330A
14.0 cm/kyr
41.9 cm/kyr
13.9 cm/kyr
41.9 cm/kyr
3-AB-68
6.2 cm/kyr
13.9 cm/kyr
33.1 cm/kyr
45.4 cm/kyr
34.4 cm/kyr
43.5 cm/kyr
Depth (m)
Sedimentation rate (cm/kyr)
ρ
H0 significance level
b
1-RJS-305
34.1 cm/kyr
3-AB-92
30.6 cm/kyr
6.8 cm/kyr
9.4 cm/kyr
30.4 cm/kyr
c
1-RJS-342
30.0 cm/kyr
37.5 cm/kyr
10.4 cm/kyr
29.8 cm/kyr
40.7 cm/kyr

Figure 4: The COCO and eCOCO analysis of the GR series for a) Southern line b) Central line and c)Northern line. Left: evolutionary correlation coefficient; right: evolutionary H_0 significance level. The top plot is the correlation coefficient. The target astronomical solutions are from the La2004 solution for a middle data age of 14 Ma, where the tested SARs range from 2.6 to 100 cm/kyr with steps of 0.33 cm/kyr and the number of Monte Carlo simulations was 2.000. The bottom top is the eCOCO-generated sedimentation rate. The sizes of the sliding window are 250 m for wells. Seven astronomical parameters are considered for the three wells. The black curve illustrates variations in sediment accumulation throughout the stratigraphic interval, as derived from the cycle-ratio method.

The power spectra from all three wells also exhibit significant peaks at wavelengths ranging from 18.1 to 29 m, which were labeled T_A and T_B. and could be related to the ~70 - 80 kyr periodicities which have been reported for sedimentary records - for Miocene deposits, it has been particularly discussed for marine isotope archives, Asian monsoon reconstructions, and deltaic depositional systems (e.g., Drury et al., 2016; Marshall et al., 2017; Gao et al., 2021). Distinctive mechanisms have been discussed for their occurrence, as double/multiple obliquity responses (e.g., Huybers and Wunsch, 2005; Huybers, 2009; Drury et al., 2016), combination tones generated by interactions among precession components (e.g., Berger et al., 2005), nonlinear resonance associated with combination tones (e.g., Rial and Anaclerio, 2000; Mitsui et al., 2025), temporal variations in the expression of the short-eccentricity band (e.g., Hennebert, 2012), and stratigraphic distortion linked with changes in sedimentation rate, compaction and hiatuses (e.g., Meyers and Sageman, 2007; Hinnov, 2000).

4.3 Revision of cyclostratigraphic evaluation: wells 1-RJS-297, 4-RJS-330 and 3-AB-68

The expansion of the study area of the Albacora Oilfield, combined with the integrated analysis of the six wells, enabled a reassessment of the cyclostratigraphic interpretations of wells 1-RJS-297, 4-RJS-330, and 3-AB-68, previously investigated by Santos *et al.* (2023). In this revision, the frequency bands of the orbital cycles were reanalyzed and subjected to minor adjustments. The precession bands were broadened based on the band proportionality analysis, and the 95 kyr and 125 kyr short-eccentricity bands were merged to align with the interpretations from wells 1-RJS-342, 3-AB-92, and 1-RJS-305 (Fig. 5 and Table 2).

Well 1-RJS-297 was located at the edge of the seismic survey used by Santos *et al.* (2023), which may have introduced distortions in the seismic data. This condition also motivated the analysis of a new seismic survey available to the region. This updated dataset was obtained by combining two surveys – the original OBC survey from Santos *et al.*, (2023) and an additional

acquisition that provided improved spatial resolution. The merged volume was processed using the more advanced Full Waveform Inversion (FWI) technique, resulting in a higher-resolution seismic dataset. This new seismic volume provided by ANP formed the basis for the well-to-well correlations, and the construction of the RGT. The depths of two biozones were re-evaluated and used as tie points for well 1-RJS-297: *Helicosphaera ampliaperta* and *Sphenolithus belemnos* (extinction ages of 14.90 Ma at 1523.4 m and 17.95 Ma at 2270.5 m, respectively; Okada and Bukry, 1980; Gradstein *et al.*, 2018).

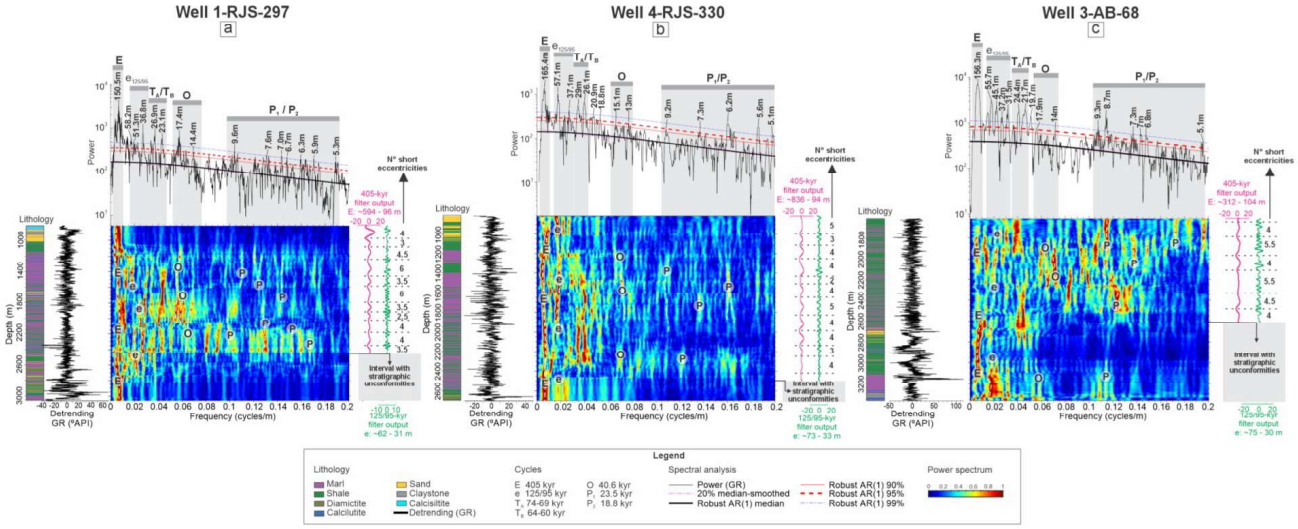


Figure 5: South section: 2π MTM power spectrum with significant peaks and defined bands for: Long-eccentricity (E), short eccentricity (e), obliquity (O) and precession (P_1/P_2/, corresponding to axial and apsidal precession); Bottom left: raw GR data, 400-m LOESS detrending curve and the lithostratigraphy for all wells; Bottom right, Evolutionary Harmonic Analysis (EHA). Wells: (a) 1-RJS-297 (step 3.6 m, window 451.44 m), (b) 41-RJS-330 (step 3.0 m, window 377 m) and (c) 3-AB-68 (step 2.8 m; window 350 m).

Well	Spectral Bands (m)								Spectral Peaks Ratios	
	E		e125/95		O		P1/P2		(E:e125:e95:O:P1:P2) (m)	
1-RJS-342	339	72	72	28	13	8	7	5	125.0:39.6:30.4:10.0:5.7:5.0	**25.0:11.7:7.9:2.0:1.1:1.0**
3-AB-92	236	66	49	24	13	11	8	5	146.5:37.9:27.2:12.1:7.7:6.8	**21.5:5:6:4.0:1.8:1.1:1.0**
1-RJS-305	277	105	50	31	15	10	8	5	143.6:37.3:32.8:13.8:7.6:6.6	**21.8:5.7:5.0:2.1:1.2:1.0**
1-RJS-297	594	96	62	31	19	13	10	5	150.5:58.2:36.8:17.4:9.6:7	**21.5:8.3:5.3:2.5:1.4:1.0**
4-RJS-330A	471	94	73	33	16	12	10	5	165.4:57.1:37.1:13.0:9.2:7.3	**22.7:7.8:5.1:1.8:1.3:1.0**
3-AB-68	312	104	75	30	19	13	10	5	156.3:55.7:31.5:17.9:8.7:6.8	**23.0:8.2:4.6:2.6:1.3:1.0**
La2004									**405:125:95:40.5:23.6:19.1**	**21.2:6.5:5.0:2.1:1.2:1.0**

Table 2: Spectral bands and peak ratios for all wells, together with the reference spectral peak ratios from Laskar *et al.* (2004) for ~14 Ma.

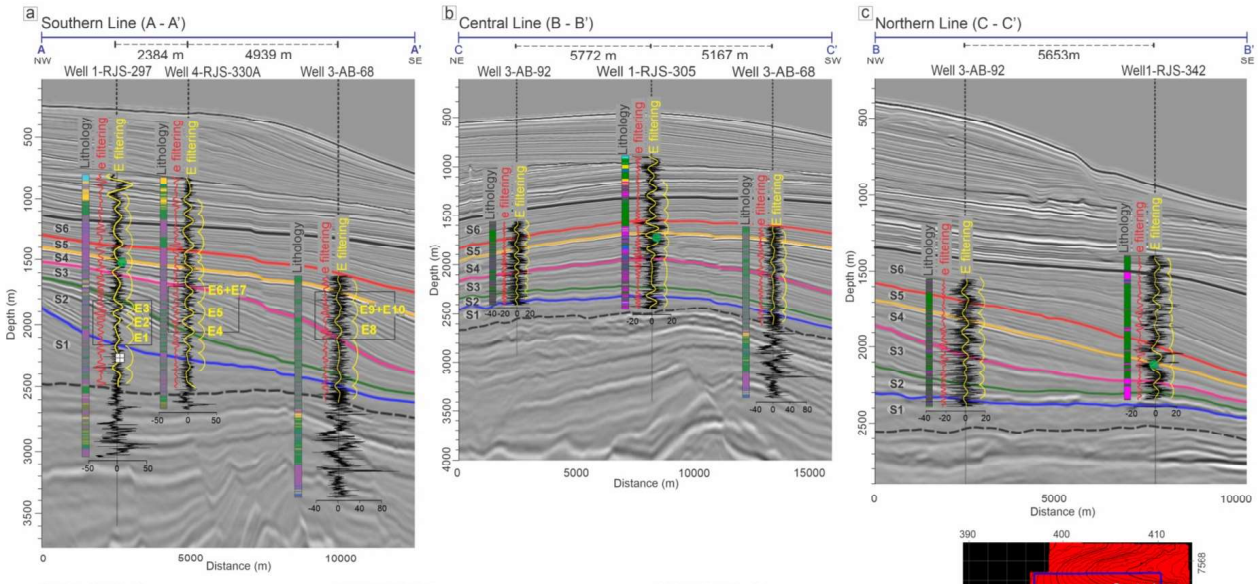
4.4 Seismic analysis and RGT Model

Seismic analysis involved reflector mapping and the construction of three seismic sections. Section A–A′ (southern line) is a dip-oriented profile crossing wells 1-RJS-297, 4-RJS-330A, and 3-AB-68; Section B–B′ (central line) is a strike-oriented profile crossing wells 3-AB-92, 1-RJS-305, and 3-AB-68; and Section C–C′ (northern line) is a dip-oriented profile crossing wells 3-AB-92 and 1-RJS-342. The seismic sections are presented in Figure 6, together with the biostratigraphic framework based on the occurrence of *Helicosphaera ampliaperta* and *Sphenolithus belemnos*, both identified in well 1-RJS-297, as previously described. *Helicosphaera ampliaperta* was also used as a temporal marker in wells 1-RJS-305 (1719 m) and 1-RJS-342 (2124 m) (Fig. 6b,c).

Based on geometry and termination of the reflectors, and their acoustic impedance contrasts, seven major, high-impedance seismic reflectors were identified and correlated among

all seismic lines (Fig. 6). They include the lower erosional unconformity (dashed black line), which is overlain by chaotic or massive to partially deformed reflectors, and six non-erosional unconformities (and associated correlative conformities) including the upper surface (solid black line) and five internal reflectors bounded by both black lines. With the exception of the lower boundary (dashed black line), all other major reflectors display a sigmoidal geometry migrating towards the depocenter in a dip view (a and c on Fig. 6) and a slightly convex-upward, arcuate geometry in a strike view (b in fig. 6).

Between these major reflectors, which actually record unconformities as well as local correlative conformities, a series of less continuous reflectors, with low impedance contrasts, records the superposition of depositional surfaces (or time lines) that register no major break and show how deposition took place within each analysed depositional sequence (S1 to S5 in Fig. 6). Landwards, they present a parallel, sub-horizontal disposition that grade to steeper reflectors at their mid portions and ends as parallel, low-angle surfaces seawards. The sigmoidal geometry seen in the dip direction records, from left to right, the shelf, slope and base of slope depositional settings whereas the overall lobate geometry of the studied package seen in a strike view indicates an overall radial distribution of the sedimentary input into the sea. The less continuous, low impedance reflectors record progradational pulses that include aggradation on the shelf, slope and base of slope. They exhibit onlap terminations, initially onto the slope and later onto the shelf, associated with downlap terminations toward the basin developed at different stages of each depositional sequence evolution. This issue ultimately controls distinct depositional ages and rates at the different settings, as will be later detailed. Therefore, these depositional surfaces, recording shallow- to deep-marine depositional processes, are key features for establishing high-resolution stratigraphic correlation between the wells.



Southern Line (A - A')

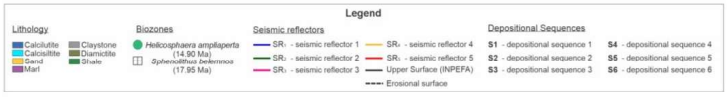
Depositional sequence	Number of E- cycles (thickness)		
	1-RJS-297	4-RJS-330A	3-AB-68
S2	3 (360 m)	1.5 (200 m)	~1 (80 m)
S3	2 (178 m)	~3 (350 m)	2.5 (275 m)
S4	~1 (114 m)	~1 (130 m)	3.5 (374 m)

Central Line (B - B')

Depositional sequence	Number of E-cycles (thickness)		
	3-AB-92	1-RJS-305	3-AB-68
S2	1 (100 m)	~1 (87 m)	~1 (80 m)
S3	2.5 (200 m)	2.5 (300 m)	2.5 (300 m)
S4	2 (200 m)	2 (250 m)	2 (400 m)

Northern Line (C - C')

Depositional sequence	Number of E-cycles (thickness)	
	3-AB-92	1-RJS-342
S2	1 (100 m)	-
S3	2.5 (200 m)	~1 (70 m)
S4	2 (250 m)	1 (130 m)



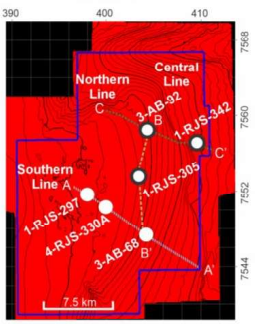


Figure 6: Top: Correlation of seismic interpretation, biostratigraphic data, detrended gamma-ray (GR) logs, and long- and short-eccentricity filters along (a) the southern dip-oriented section, highlighting the long-eccentricity cycles identified within depositional sequences S2, S3, and S4; (b) the central strike-oriented section; and (c) the northern dip-oriented section. Bottom: Summary tables showing the number of cycles identified within each depositional sequence, together with a bathymetric map of the study area.

The seven reflectors were extracted from the RGT model, including the erosional surface, reflectors SR1 to SR5, and the upper surface defined by the stratigraphic break identified through INPEFA analysis. The results obtained (Figure 7) enabled the plan-view analysis of the reflectors within a chronostratigraphic domain, highlighting depositional patterns.

The slice corresponding to the erosional surface reveals elongated and sinuous geometries, interpreted as submarine channels, predominantly located in the northern portion of the study area, in proximity to wells 3-AB-92 and 1-RJS-342.

Between SR1 and SR3, the RGT model highlights a progressive basin infill, marked by the attenuation of channel-related relief and increased lateral continuity of reflectors. This pattern suggests successive depositional events contributing to channel infilling.

In the slice corresponding to SR4, a significant variation in RMS impedance is observed in the central-southern portion of the area, encompassing wells 1-RJS-297, 4-RJS-330A, 1-RJS-68, and 1-RJS-305. This variation indicates a sedimentary pulse with distinct characteristics, possibly associated with the input of coarser-grained deposits (e.g., sandy-rich intervals) into the system, suggesting an increase in depositional energy. In the SR5 slice, the continuity of deposition is observed, marked by a more homogeneous reflector pattern, indicating a return to more stable depositional conditions and lower lateral facies variability.

Finally, the upper surface slice displays greater heterogeneity in the seismic pattern, with more abrupt lateral variations. This pattern is interpreted as a shift in the depositional regime, potentially related to changes in sediment supply, base level fluctuations, or reorganization of the depositional system.

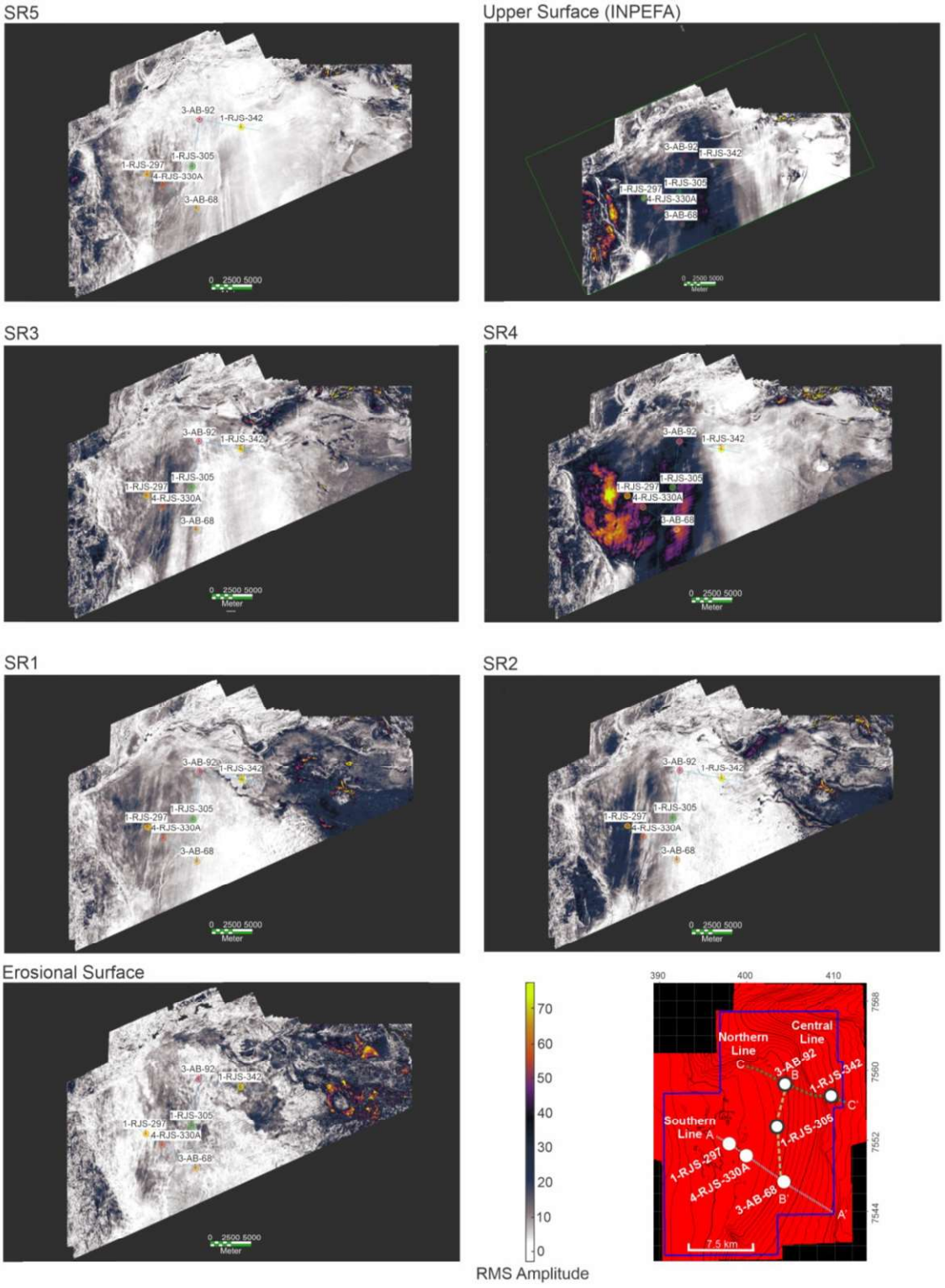


Figure 7: RMS (Root Mean Square) amplitude attribute of the RGT slice for the following horizons: the erosional surface, seismic reflectors SR1, SR2, SR3, SR4 and SR5, and the upper surface from the INPEFA curve. Right bottom: bathymetric map of the study area.

5. Discussion

5.1 Astronomical forcing and sedimentation

The cyclostratigraphic analyses of the GR data from the six studied wells display similar peak patterns and proportions in the 2π-MTM spectral analysis (Figs. 3 and 5 and Table 2). The COCO and eCOCO statistical analyses corroborated the interpretation of the orbital cycle bands (Fig. 4). COCO analysis results indicated that peak sedimentation rates ranged from 30.0 to 45.4 cm/kyr across the three wells, with no significant variations observed between them (Fig. 4). These results are also consistent with the sedimentation rates (~30 cm/kyr) reported in previous studies conducted in the same region (Castro, 2005; Almeida & Kowsmann, 2014; Santos *et al.*, 2023).

5.2 Geological Interpretation Through Data Integration

In this section, we present and discuss three geological sections based on the integration of seismic data, RGT model, and cyclostratigraphic and INPEFA analyses.

5.2.1 Southern dip line (1-RJS-297, 4-RJS-330, and 3-AB-68)

This dip-oriented, 7,323 m long line includes three wells (1-RJS-297, 4-RJS-330, and 3-AB-68). As discussed previously, this study reinterprets the dataset using higher-resolution seismic data, increasing the seismic resolution from approximately 30 m in Santos *et al.* (2023) to approximately 20 m. (Fig. 6). In addition to seismic and cyclostratigraphic data, we used the auxiliary INPEFA tool (Fig. 2) and RGT model (Fig. 7), which provided new insights and supported an integrated interpretation of the dataset.

Seven seismic reflectors were mapped across all seismic profiles (Fig. 6) and used in the construction of the RGT model (Fig. 2). The dashed black reflector at the base of the profile records the erosional surface ascribed by Santos *et al.* (2023) to the eustatic fall that occurred at ~17 Ma and marks the onset of the Miocene Climatic Optimum. The top of the section is delineated by a sigmoidal reflector with an almost planar geometry and low dip (solid black line – Fig. 6) that corresponds to an inflection point in the INPEFA data of all analyzed wells (Fig. 2). Both surfaces separate six, well-defined sigmoidal depositional bodies present along the three sections herein investigated (Southern, Northern and Central line) that constitutes the focus of this work. Each of these sigmoidal bodies, limited by five colored reflectors, records a similar

depositional pattern and is related to a high-frequency depositional sequence; therefore, they were labeled S1, S2, S3, S4, S5, and S6 in Figure 6.

The six sigmoidal depositional bodies display a sigmoidal geometry and migrate toward the basin depocenter, characterizing an overall progradational stacking pattern (Fig. 6a). The analysis of the internal reflectors within each sigmoidal unit reveals the presence of onlap, initially onto the slope and later onto the shelf, always associated with downlap terminations towards the basin, defining high-frequency depositional sequences. Within each sequence, typically the lower / older reflectors are progradational and display erosional to slightly aggradational upper limits. On the other hand, the upper / younger strata show well-defined prograding and aggrading trends onto the basinal and shelfal deposits, respectively.

The number of long-eccentricity cycles recorded in the three wells within each depositional sequence varies downdip along the southern section (Fig. 6a and corresponding table). The most pronounced difference occurs between reflectors SR1 and SR2, within depositional sequence S2, where discrepancies of up to two cycles are observed, whereas smaller variations characterize the remaining intervals.

Depositional sequences S2 in well 1-RJS-297, S3 in well 4-RJS-330A, and S4 in well 3-AB-68 preserve the most complete stratigraphic records. In sequence S2 (well 1-RJS-297), the cycle count spans from approximately the lower trough of cycle E1 to the upper trough of cycle E3, totaling three cycles. In sequence S3 (well 4-RJS-330A), the interval extends from the crest of cycle E4 to approximately the crest corresponding to cycles E6–E7, also totaling about three cycles. Finally, in sequence S4 (well 3-AB-68), the interval ranges from the lower trough of cycle E8 to approximately the crest above cycles E9-E10, totaling about 3.5 cycles.

These well-preserved intervals allow the recognition of continental shelf, slope, and base-of-slope environments, as well as the quantification of 405-kyr cycles within each setting. In general, one 405-kyr cycle is preserved on the continental shelf, three cycles along the slope, and one cycle at the base of the slope. This distribution indicates that high-frequency depositional sequences are thicker and preserve a more complete orbital record in the steeper mid-slope region, where progradation is more pronounced.

The depositional sequence S5, bounded by reflectors SR4 and SR5, comprises only continental shelf deposits (Fig. 6a). As the thickest and most complete depositional record occurs along the mid-slope region, and this portion is not registered in the analyzed section, this unit does not provide sufficient information to constrain the duration of its deposition. It is worth noting that additional depositional units may exist above S5; however, it was not possible to distinguish them by our study.

5.2.2 Northern dip line (3-AB-92 and 1RJS-342)

The 5,653 m long, dip-oriented seismic section includes two wells (3-AB-92 and 1RJS-342). The reflectors display planar to slightly concave-upward geometries dipping offshore (Fig. 6c). This likely reflects the oblique orientation of the seismic line relative to the main progradational axis situated to the south (Fig. 6a).

The geometry of the seismic reflectors indicates a progradational trend, although within lower progradation rates than those observed in the southern section. This difference is associated with the lateral location of the seismic line relative to the overall lobate geometry of the shelf and associated slope. The down-dip stratal terminations of the internal reflectors within the depositional packages are characterized by downlap, whereas their up-dip terminations are not seen in this seismic line.

A progressive thinning of the depositional bodies is observed toward well 1RJS-342, which is corroborated by a reduction in the number of recorded 405-kyr cycles compared to 3-AB-92. This variation is most pronounced in unit S3, where a difference of nearly two cycles is observed (Fig. 6b). A maximum of 2.5 405-kyr cycles is recorded in unit S3 of well 3-AB-92 within this section.

5.2.3 Central strike line (3-AB-92, 1-RJS-305, and 3-AB-68)

This strike-oriented seismic section (Fig. 6b) includes three wells: 3-AB-92, 1-RJS-305, and 3-AB-68. Two of these wells (3-AB-92 and 3-AB-68) are also included in the two analyzed dip sections, thereby forming an integrated analysis grid. The central section extends for 10,939 m and lies approximately along the same bathymetry (see Fig. 1). In this section, the mapped seismic reflectors display a slight convex-upward geometry, with thickness variations between them, showing a progressive thickness increase southwards, toward well 3-AB-68. A notable thickening occurs in unit S4, where thickness increases from 277 m at well 1-RJS-305 to 370 m at well 3-AB-68. In the RGT model, a strong variation in RMS impedance is observed in the interval associated with SR4 in the southern portion of the area (Fig. 7), providing additional evidence for increased sediment supply.

The central section exhibits small changes (less than half a cycle) in the number of 405-kyr cycles recorded between reflectors across the three wells (see table in Fig. 6b). The limited extent of the section and its strike orientation explain the relatively uniform thickness of each unit and the number of cycles they record. As this line shares two wells with the dip sections, it is easy to perceive that the unit's thickness and number of recorded cycles are a result of the

visualized region (shelf, slope, or base of slope) of each high-frequency depositional sequence.

5.3 Understanding Depositional Variability Through Data Integration

The integration of the results obtained from the different methodologies applied to the three studied sections provided important insights into the processes controlling sedimentation and the preservation of the sedimentary record across a broad area of the basin. The seismic sections display reflectors with distinct geometries and variations in the number of long-eccentricity cycles between them, indicating distinct sedimentation rates across the investigated area.

A higher sedimentation rate is observed in the southern section compared to the northern section, as evidenced by: (i) a progressive increase in thickness between reflectors toward the south, identified in the central section (Fig. 6c); (ii) an enhancement of the RMS attribute in the RGT model in the central – southern portion of the area during the SR4 interval (Fig. 7); and (iii) seismic reflector geometries indicating higher progradation rates in the southern section relative to the northern section. These variations in sedimentation rates were not detected in the COCO and eCOCO analyses (Fig. 4) and became evident only through the integration of cyclostratigraphic results with seismic data and the RGT model.

Another important observation derived from this methodological integration is the variation in stratigraphic preservation. Some areas preserve a more complete geological record than others, as evidenced by differences in the number of long-eccentricity cycles present between mapped seismic reflectors (insert tables in Fig. 6). This observation led us to establish two main hypotheses to explain the absence of these cycles in certain intervals: (i) progradation and diachronous stratigraphic preservation; and (ii) depositional hiatuses associated with erosional events. It is important to emphasize that both hypotheses may occur concomitantly in the sedimentary record, as will be discussed as follows.

5.3.1 Progradation and the diachronous preservation of astronomical cycles

Seismic profiles display seaward migration of reflectors, indicating progradation, throughout both the southern and northern dip sections (Fig. 6a and 6c). Since sedimentary deposits migrate laterally through progradation, time lines are not preserved vertically but rather as oblique clinoforms controlled by the balance between sediment supply and accommodation space. As a direct consequence, the record of orbital forcing will not be complete in the vertical column of a single well. The most complete record can be recovered

through the stratigraphic stacking of laterally correlatable wells, whose partial and diachronous records, when combined, reconstruct the temporal succession of orbital cycles.

The study area encompasses continental shelf, slope, and base-of-slope regions, each characterized by specific environmental conditions directly related to sedimentary depositional processes. The southern section indicates that the most complete geological record systematically occurs in the mid-slope region, where a thicker sedimentary package between seismic reflectors is observed, with the highest preservation of long-eccentricity cycles (approximately three cycles).

The central section suggests the absence of significant erosional events between the five analyzed seismic reflectors in wells 3-AB-92, 1-RJS-305, and 3-AB-68. This observation allows us to infer that the absence of long-eccentricity cycles in the dip sections is more likely related to sediment bypass processes in the more proximal areas and to reduced or eventually absent sediment supply in the more distal regions.

To illustrate the partial absence of this record, Figure 8, based on seismic data of S2, was constructed to represent the sedimentary package (Fig. 8a) and the deposition of astronomical cycles (Fig. 8b) at a higher stratigraphic resolution. Figure 8b shows that the sedimentary record is most complete in the intermediate portion of the slope, associated with the steeper segment of the seismic reflector, where a greater thickness and the preservation of up to three long-eccentricity cycles are observed, totaling a period of ~1.2 Myr for the deposition of this unit. The geometry of the internal reflectors displays onlap stratal terminations in the intermediate slope, related to phases of relative base-level rise, followed by aggradation on the continental shelf and subsequent progradation across the slope and base-of-slope regions. This stratal arrangement prevents sedimentary preservation on the shelf during the early stages of base-level rise, with deposition occurring only after the onset of aggradation on it. Part of the progradational phase is also not preserved on the shelf due to sediment bypass. As a result, shelf deposits do not fully record the initial and final stages of deposition of the sedimentary package. Deposits located in more distal areas exhibit reduced thickness and preserve fewer astronomical cycles. In these regions, lower sediment supply combined with sediment trapping in more proximal areas likely explains the reduced stratigraphic record.

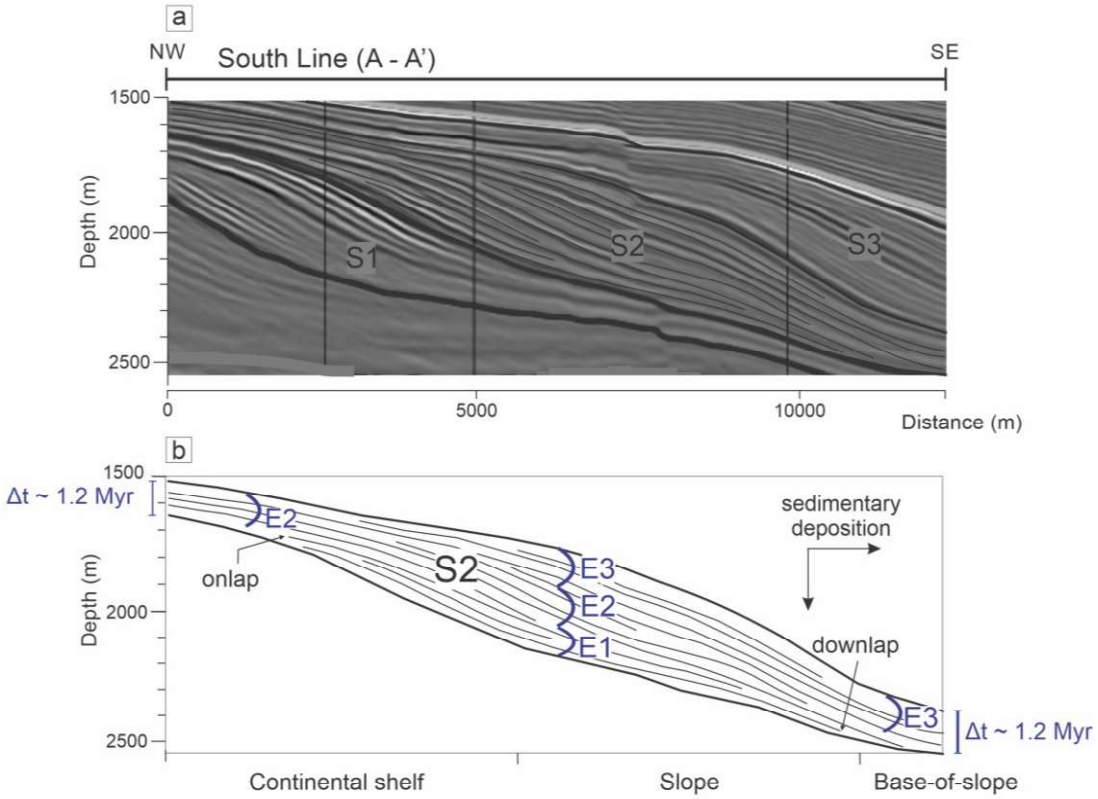


Figure 8: Depositional model illustrating sequences S1, S2, and S3 along the southern line. (a) Seismic expression of the sequences. (b) Detailed representation of depositional sequence S2, highlighting onlap and downlap terminations, the distribution of cycles across different sectors of the basin, and their corresponding temporal framework.

5.3.2 Depositional hiatuses associated with erosional events

Erosional processes may also have contributed to the removal of parts of the sedimentary record. Erosion and discontinuous sedimentation likely operate simultaneously within the depositional system. To evaluate their relative importance in controlling stratigraphic preservation within the study area, we examined potential evidence of erosional events in the seismic data and well GR records, integrating cyclostratigraphic results with INPEFA analyses.

In the seismic imaging, no significant erosional events are observed within the sedimentary packages bounded by the seismic reflectors. The dashed black reflector located at the base of the profiles (Fig. 6) exhibits clear evidence of erosion and was interpreted by Santos *et al.* (2023) as an unconformity.

The search for erosional events in the data analyses was based on the following criteria: (i) identification of variations in the number of long-eccentricity cycles between mapped seismic reflectors; (ii) quantification of the number of short-eccentricity cycles contained within each long-eccentricity cycle; (iii) recognition of erosional signatures in cycle tracking using EHA, as

defined by Meyers & Sageman (2004); and (iv) detection of inflection points in the INPEFA curve.

Based on these criteria, minor erosional events are interpreted to occur between the five mapped seismic reflectors, resulting in the partial loss of short-eccentricity cycles. In well 3-AB-92, between approximately 2400 and 2100 m depth, tracking of the long-eccentricity band in the EHA demonstrates reduced sedimentation rates relative to the remainder of the profile, expressed by four long-eccentricity cycles containing only 2.5 short-eccentricity cycles each (Fig. 3a). Likewise, in well 1-RJS-342, between ~1900 and 1500 m depth, four long-eccentricity cycles are preserved, each likely containing ~2 short-eccentricity cycles (Fig. 3b). This interpretation is reinforced by the presence of a bifurcation in the long-eccentricity cycle tracking in the EHA within the same interval, a feature described by Meyers & Sageman (2004) as diagnostic of partial cycle loss. In well 1-RJS-305, between depths of ~2200 and 1900 m, a clear deviation in long-eccentricity signal tracking in the EHA, with a bifurcation-like pattern, is observed (Fig. 3c). In addition, the presence of amalgamated long-eccentricity cycles associated with seven short-eccentricity cycles further supports the partial loss of short-eccentricity cycles within this interval.

The upper portion of the wells, corresponding to the mapped continuous black surface (Fig. 6), records a more pronounced erosional event associated with the loss of long-eccentricity cycle signals. This event is corroborated by an inflection in the INPEFA curve, consistently observed in all wells with available data and coincident with the same seismic surface (Fig. 2). In addition, the presence of an erosional signature (Meyers & Sageman, 2004) in the tracking of the long-eccentricity signal in the EHA in wells 4-RJS-330 (~1000 m depth), 1-RJS-297 (~1200 m depth), and 1RJS-342 (~1500 m depth) further supports the interpretation of a regionally correlated erosional episode at this stratigraphic level (Figs. 3 and 5). Figure 9 presents the indicators of minor depositional and erosional events in well 1-RJS-342, illustrating the application of the adopted criteria.

Based on this interpretation, the interval between the five mapped seismic reflectors shows no evidence of significant erosional events, with only minor losses observed, mainly associated with the removal of short-eccentricity cycles. Nevertheless, within the sedimentary packages, the preserved amount of time (astronomical cycles) varies as a consequence of discontinuous sedimentation.

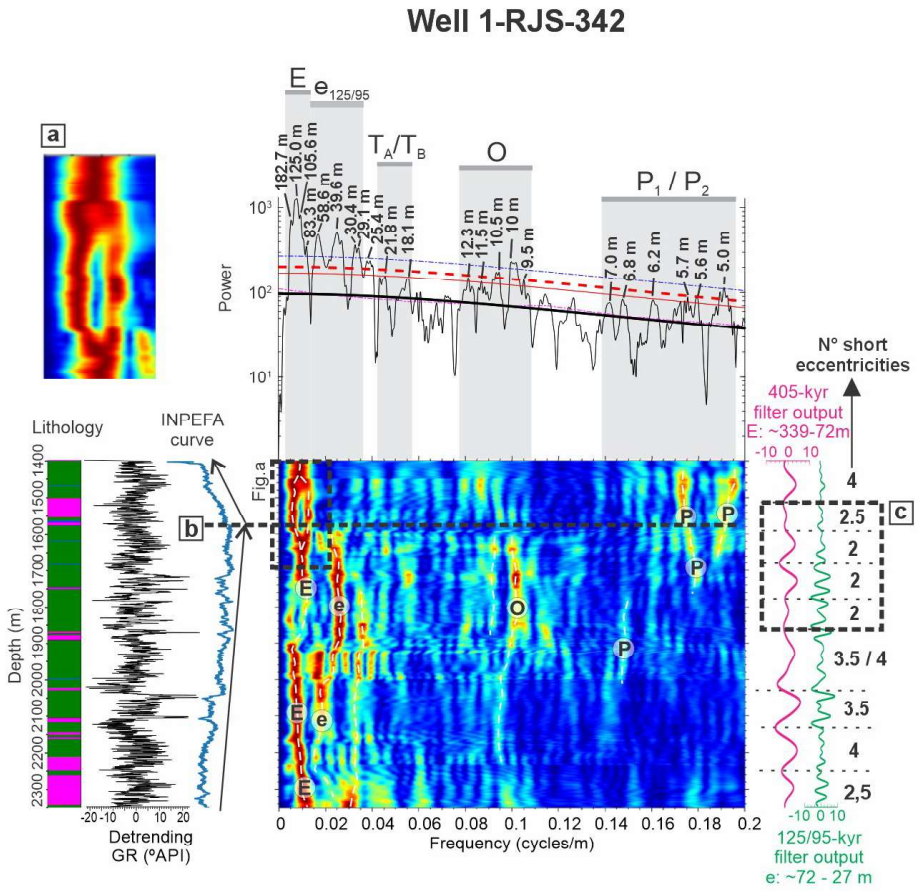


Figure 9: Indicators of depositional minor erosional events signals in well 1-RJS-342. (a) Depositional hiatuses signature between ~1500 and ~1650 m depth, following Meyers & Sageman (2004). (b) INPEFA inflection at ~1575 m. (c) Four preserved long-eccentricity cycles between 1500 and ~1900 m depth, each comprising ~2 short-eccentricity cycles.

5.4 Stratigraphic Completeness and the Preservation of Long-Eccentricity Cycles

As previously discussed, the thickest stratigraphic record and, consequently, the most expressive cyclostratigraphic record (in terms of the number of astronomical cycles) occurs in the mid-slope deposits (Fig. 6a), where approximately three long-eccentricity cycles are observed across successive depositional sequences. In some intervals, the presence of amalgamated long-eccentricity cycles can also be identified. The interpretation of these amalgamated cycles (E6 and E7 in well 4-RJS-330A and E9 and E10 in well 3-AB-68 – Figs. 3 and 6) is based on the occurrence of a greater number of short-eccentricity cycles than expected within a single long-eccentricity cycle. This suggests that more than one long-eccentricity cycle was originally present but was partially removed by erosion.

Considering the intervals with the best stratigraphic preservation, associated with mid-

slope deposits, the three wells that compose the southern line (1-RJS-297, 4-RJS-330A, and 3-AB-68) record the most complete portion of the succession. In these wells, between depths of 1500 and 2200 m, corresponding to sequences S2, S3, and S4, a record of approximately 9.5 long-eccentricity cycles is preserved (Fig. 6a). It is noteworthy that mid-slope deposits occur exclusively within these sequences; therefore, the estimation of the time involved can be more reliably constrained to this interval. In contrast, Santos *et al.* (2023) reported approximately 5.5 long-eccentricity cycles for the same stratigraphic interval. This corresponds to an increase of more than 1.6 Myr in the total depositional timespan. Although the effectiveness of the approach adopted in the previous study, our integrated analyses - particularly the interpretation of a new higher-resolution seismic volume - provide a more refined understanding of the progradational stacking patterns, as well as the variability in stratigraphic preservation across different depositional environments. These results bring into focus a central issue in the evaluation of sedimentary successions: the degree of completeness of the stratigraphic record and the impact of lateral variability within deposits.

In such context, cyclostratigraphic analyses requires a thorough understanding of both factors. As highlighted by Sinnesael *et al.* (2019), astronomical signals may remain detectable even in stratigraphic records that are not fully continuous, emphasizing that completeness must be carefully assessed rather than assumed. However, such an assessment is rarely achievable using isolated well-log data alone, since these provide only a point-based representation of the depositional system and do not capture its lateral variability associated with discontinuous deposition. As a result, key variations related to depositional stacking patterns, such as progradation, retrogradation, and aggradation, may not be properly resolved, nor can differences in stratigraphic preservation across depositional environments be fully constrained, as demonstrated in this study. Furthermore, lateral variability within sedimentary deposits may also be reflected in proxy values within a single layer, representing an important factor in both subsurface and outcrop-based analyses. In this context, Chen and Mitchell (2025) demonstrate that conducting lateral measurements along a single stratigraphic horizon tends to yield statistically more robust results in cyclostratigraphic analyses.

Based on the interpreted cycles preserved within units S2, S3, and S4 from wells along the southern line, the total duration of sediment deposition for these three units is estimated at approximately 3.85 Myr. In comparison, the age difference between the extinction datums of *Sphenolithus belemnos* and *Helicosphaera ampliaperta* in well 1-RJS-297 (located approximately half a cycle below SR1 and near SR4, respectively) is 3.05 Myr (Fig. 6a). Although the extinction depths are slightly offset relative to SR1 and SR4, the ages remain comparable. The taxon *Helicosphaera ampliaperta* is identified in wells 1-RJS-297, 1-RJS-305, and 1-RJS-342 at

comparable stratigraphic levels, supporting the interpretation that this surface (near SR4) corresponds to the 14.9 Ma temporal marker. The resulting difference of approximately 0.8 Myr between the biostratigraphic and cyclostratigraphic age estimates highlights the higher temporal resolution of cyclostratigraphy relative to biostratigraphy. This reflects the comparatively lower accuracy and precision of microfossil-based chronostratigraphic events, which typically provide coarser temporal constraints than cyclostratigraphic approaches based on the stable long-eccentricity (405-kyr) cycle (Hinnov, 2013; Meyers, 2019).

6. Conclusions

This study investigates the evolution of Miocene deposits in the Albacora Oilfield, Campos Basin, Brazil, through an integrated framework that combines cyclostratigraphy and seismic stratigraphy, extending and refining the study by Santos *et al.* (2023). The availability of modern, higher-resolution seismic data and new well-logs allowed the expansion of the previously investigated area to approximately 62 km². The broader spatial coverage, coupled with the incorporation of additional analytical tools (INPEFA and the RGT model), clearly provided enhanced constraints on the evolution of the depositional system and its associated geological time framework.

In agreement with the previous work, our results indicate a marked orbital control on sedimentation across the six analyzed well-logs. COCO-derived sedimentation rates (ranging from 30.0 to 45.4 cm/kyr) support the interpretation of spectral bands associated with orbital forcing. MTM spectral analyses reveal statistically significant peaks, commonly exceeding the 95-99% confidence thresholds, with spectral ratios closely matching those predicted for astronomical frequencies at ~14 Ma (405:125:95:40.5:23.6:19.1 ≈ 21.2:6.5:5.0:2.1:1.2:1.0; Laskar *et al.*, 2004).

Seismic stratigraphic analysis reveals a predominantly progradational stacking pattern, corroborated by the RGT model and highlights preferential stratigraphic preservation within mid-slope deposits. In this sector, greater sediment thickness and a more complete preservation of orbital cycles demonstrate that robust estimates of depositional duration rely on multi-well correlation, when focused on intervals of enhanced preservation. Compared to Santos *et al.* (2023), this integrated approach increases the total depositional timespan of more than 1.6 Myr between depths of 1500 and 2200 m.

The integration of cyclostratigraphy, seismic stratigraphy, the RGT model, and INPEFA further enabled the identification of key stratigraphic surfaces associated with depositional hiatuses and/or erosional events, recognized by the attenuation or loss of long-eccentricity

cyclicity, as evidenced by EHA patterns, inflections in INPEFA curves, and their correspondence with mapped seismic horizons. Moreover, seismic data and the RGT model suggest variations in sedimentation rates between the northern and southern sectors of the study area that are not clearly resolved by COCO and eCOCO analyses alone.

In the Albacora Oilfield, the integration of cyclostratigraphic results with seismic stratigraphy, the RGT model, and INPEFA increases the depositional timespan previously estimated for the same stratigraphic interval by more than 1.6 Myr – which is a consequence of accounting for the lateral variability of stratigraphic preservation across shelf, slope, and base-of-slope settings. This variability, which isolated well-log records systematically underrepresent due to progradation and sediment bypass, becomes tractable only through seismic-supported lateral correlation. The use of six wells distributed across these settings demonstrates that stratigraphic completeness can only be fully assessed through a multi-well framework. Seismic reflectors, when interpreted within an RGT framework and validated against cyclostratigraphic results, delimit stratigraphic intervals whose preserved orbital content is quantifiable (in this study, in terms of long-eccentricity cycles), providing a basis for correlating the depositional record with the astronomical time scale. To our knowledge, this constitutes the first systematic investigation of how astronomical cycles are laterally preserved within a seismic volume as a function of depositional architecture – and of how that preservation, when properly accounted for, reshapes estimates of geological time.

7. Acknowledgments

This study was financed in part by the Coordenação de Aperfeiçoamento de Pessoal de Nível Superior - Brasil (CAPES) - Finance Code 001. The authors gratefully acknowledge the Brazilian National Agency for Petroleum, Natural Gas and Biofuels (ANP) for providing the public well-log and seismic datasets, Petrobras S.A. for providing technical support and infrastructure for this work, and the Observatório Nacional – MCTI, where this research was conducted.

We also thank the financed support from National Council for Scientific and Technological Development (CNPq - 314462/2020-1 to D.R.F. and 313018/2022-7 to P.S.G.P.) and Foundation Carlos Chagas Filho Research Support of the State of Rio de Janeiro (FAPERJ - E-26/200.931/2022 to D.R.F. and 204.404/2021 to M.C.).

8. Declaration of generative AI and AI-assisted technologies in the manuscript preparation process.

During the preparation of this work, the author used Chat GPT for English language

editing and text refinement. The use of artificial intelligence was limited to text editing and did not involve any contribution to the scientific content, data analysis, interpretation, or conclusions of this study. All scientific work and intellectual content remain the full responsibility of the authors. After using this tool, the author reviewed and edited the content as needed and take full responsibility for the content of the published article.

9. References

ANP (Brazilian National Agency of Petroleum, Natural Gas and Biofuels), 2018. Albacora. https://www.gov.br/anp/pt-br/assuntos/exploracao-e-producao-de-oleo-e-gas/desenvolvimento-e-producao/pd/albacora.pdf.

Bashir, Y., Zahari, M.A.A.B., Karaman, A., Doğan, D., Döner, Z., Mohammadi, A. and Ali, S.H., 2024a. Artificial intelligence and 3D subsurface interpretation for bright spot and channel detections. *AIMS Geosciences*, 10(4), pp.662–683.

Bashir, Y., Siddiqui, N.A., Morib, D.L., Babasafari, A.A., Ali, S.H., Imran, Q.S. and Karaman, A., 2024b. Cohesive approach for determining porosity and P-impedance in carbonate rocks using seismic attributes and inversion analysis. *Journal of Petroleum Exploration and Production Technology*, 14(5), pp.1173–1187.

Bastos, G., Bastos, I.P., 2017. Bacia de Campos: Sumário geológico e setores em oferta. ANP, Rio de Janeiro. https://www.gov.br/anp/pt-br/rodadas-anp/rodadas-concluidas/concessao-de-blocos-exploratorios/14a-rodada-licitacoes-blocos/arquivos/areas-oferta/sumario-campos.pdf.

Berger, A., Mélice, J.L., Loutre, M.F., 2005. On the origin of the 100-kyr cycles in the astronomical forcing. Paleoceanography 20 (4), PA4019. https://doi.org/10.1029/2005PA001173.

Cândido, A., 1990. Desenvolvimento e estratégia de produção do campo de Albacora. Bol. Geociênc. Petrobras 4 (2), 175–181.

Castro, A.H.A., 2005. Estudo de ciclicidade orbital com base em dados sísmicos: exemplo para o Mioceno da Bacia de Campos. *Rev. Bras. Geociênc.* 35, 139–151.

Castro, R.D., Picolini, J.P., 2015. Principais aspectos da geologia regional da Bacia de Campos. In: *Geologia e Geomorfologia*, pp. 1–12. https://doi.org/10.1016/B978-85-352-6937-6.50008-2.

Chen, F., Mitchell, R.N., 2025. Is One Sample Enough? Testing the Importance of Lateral Sedimentary Variability in Cyclostratigraphy. *Geochem. Geophys. Geosyst.* 26, e2024GC012087. https://doi.org/10.1029/2024GC012087.

Chen, Q., Sidney, S., 1997. Advances in seismic attribute technology. In: *SEG Tech. Program Expanded Abstracts*, pp. 730–733. https://doi.org/10.1190/1.1886114.

de Almeida, A.G., Kowsmann, R.O., 2016. Geomorphology of the Continental Slope and São Paulo Plateau. In: *Geology and Geomorphology*. Elsevier, pp. 33–66. https://doi.org/10.1016/B978-85-352-8444-7.50010-X.

De Gasperi, A., Catuneanu, O., 2014. Sequence stratigraphy of the Eocene turbidite reservoirs in Albacora Field, Campos Basin, offshore Brazil. *AAPG Bull.* 98 (2), 279–313. https://doi.org/10.1306/07031312117.

de Souza Cruz, C.E., Barrocos, S.L.S., Appi, C.J., 1987. Modelo deposicional dos reservatórios turbidíticos oligocênicos/eomiocênicos do Campo de Albacora, Bacia de Campos, Brasil. *Bol. Geociênc. Petrobras* 1 (2), 215–223. https://bgp.petrobras.com.br/bgp/article/view/550.

Drury, A.J., John, C.M., Shevenell, A.E., 2016. Evaluating climatic response to external radiative forcing during the late Miocene to early Pliocene: New perspectives from eastern equatorial Pacific (IODP U1338) and North Atlantic (ODP 982) locations. Paleoceanography 31, 167–184. https://doi.org/10.1002/2015PA002881.

Figueiredo Jr., A.G., Pacheco, C.E.P., Vasconcelos, S.C., Silva, F.T., 2015. Geomorfologia e sedimentologia da plataforma continental. In: *Geologia e Geomorfologia*, pp. 13–32. https://doi.org/10.1016/B978-85-352-6937-6.50009-4.

Filho, N.C., Perlmutter, M.A., 2005. Cicloestratigrafia: Análise Quantitativa De Ciclos Sedimentares, Aplicações Na Seção Sedimentar De Idade Oligoceno-Mioceno Da Bacia De Campos. Revista Brasileira de Geociencias 35, 13e26. https://doi.org/10.25249/0375-7536.200535ete1326.

Gao, P., Nie, J., Yan, Q., Zhang, X., Liu, Q., Cao, B., Pan, B., 2021. Millennial resolution late Miocene northern China precipitation record spanning astronomical analogue interval to the future. Geophys. Res. Lett. 48, e2021GL093942. https://doi.org/10.1029/2021GL093942.

Geng, Z., Wu, X., Shi, Y., & Fomel, S. (2020). Deep learning for relative geologic time and seismic horizons. Geophysics, 85(4), WA87-WA100. https://doi.org/10.1190/geo2019-0252.1.

Gong, Z., 2021. Cyclostratigraphy of the Cryogenian Fiq Formation, Oman and its implications for the age of the Marinoan glaciation. Glob. Planet. Change 204, 103584. https://doi.org/10.1016/j.gloplacha.2021.103584.

Gradstein, F.M., Ogg, J.G., Schmitz, M.D., Ogg, G.M., 2018. Geologic Time Scale 2020.

Guardado, L.R., Gamboa, L.A.P., Lucchesi, C.F., 1989. Petroleum geology of the Campos Basin, Brazil, a model for a producing Atlantic-type basin. In: Edwards, J.D., Santogrossi, P.A. (Eds.), Divergent/Passive Margin Basins: AAPG Memoir 48. AAPG, Tulsa, Oklahoma, USA, pp. 3–79.

Hennebert, M., 2012. Hunting for the 405-kyr eccentricity cycle phase at the CretaceousePaleogene boundary in the Aïn Settara section (Kalaat Senan, central Tunisia). Carnets de Geologie [Notebooks on Geology], Brest, Article 2012/05 (CG2012_A05) 93 - 116. https://doi.org/10.4267/2042/47314.

Hinnov, L.A., 2000. New perspectives on orbitally forced stratigraphy. *Annu. Rev. Earth Planet. Sci.* 28, 419–475. https://doi.org/10.1146/annurev.earth.28.1.419.

Hinnov, L.A., 2013. Cyclostratigraphy and its revolutionizing applications in the Earth and planetary sciences. Geol. Soc. Am. Bull. 125 (11−12), 1703–1734.

Holbourn, A.E., Kuhnt, W., Clemens, S.C., Kochhann, K.G.D., Jöhnck, J., Lübbers, J., Andersen, N., 2018. Late Miocene climate cooling and intensification of southeast Asian winter monsoon. Nat. Commun. 9 (1), 1584. https://doi.org/10.1038/s41467-018-03950-1.

Huang, H., Gao, Y., Jones, M.M., Tao, H.F., Carroll, A.R., Ibarra, D.E., Wu, H.C., Wang, C. S., 2020. Astronomical forcing of Middle Permian terrestrial climate recorded in a large paleolake in northwestern China. Palaeogeogr. Palaeoclimatol. Palaeoecol. 550, 109735 https://doi.org/10.1016/j.palaeo.2020.109735.

Huybers, P., Wunsch, C., 2005. Obliquity pacing of the late Pleistocene glacial terminations. Nature 434 (7032), 491–494. https://doi.org/10.1038/nature03401.

Huybers, P., 2009. Pleistocene glacial variability as a chaotic response to obliquity forcing. Clim. Past 5 (3), 481–488. https://doi.org/10.5194/cp-5-481-2009.

Kodama, K.P., Hinnov, L., 2015. Rock Magnetic Cyclostratigraphy. Wiley-Blackwell (176 pp).

Laskar, J., Robutel, P., Joutel, F., Gastineau, M., Correia, A.C.M., Levrard, B., 2004. A long-term numerical solution for the insolation quantities of the Earth. Astron. Astrophys. 428, 261–285. https://doi.org/10.1051/0004-6361:20041335.

Leandro, C.G., Savian, J.F., Kochhann, M.V.L., Franco, D.R., Coccioni, R., Frontalini, F., Gardin, L.J., Figueiredo, M., Tedeschi, L.R., Janikian, L., Almeida, R.P., Trindade, R.I.F., 2022. Astronomical tuning of the Aptian stage and its implications for age recalibrations and paleoclimatic events. Nat. Commun. 13, 2941. https://doi.org/10.1038/s41467-022-30075-3.

Li, M., Kump, L.R., Hinnov, L.A., Mann, M.E., 2018. Tracking variable sedimentation rates and astronomical forcing in Phanerozoic paleoclimate proxy series with evolutionary correlation coefficients and hypothesis testing. Earth Planet. Sci. Lett. 501, 165–179. https://doi.org/10.1016/j.epsl.2018.08.041.

Li, M, Huang, C.J., Ogg, J., Zhang, Y., Hinnov, L., Wu, H.C., Chen, Z.Q., Zou, Z.Y., 2019a. Paleoclimate proxies for cyclostratigraphy: comparative analysis using a lower Triassic marine section in South China. Earth Sci. Rev. 189, 125–146. https://doi.org/10.1016/j.earscirev.2019.01.011.

Li, M., Hinnov, L., Kump, L., 2019b. Acycle: Time-series analysis software for paleoclimate research and education. Comput. Geosci. 127, 12–22. https://doi.org/10.1016/j.cageo.2019.02.011.

Li, M. Acycle: Enhanced time-series analysis software for geoscience research and education. Sci. China Earth Sci. 2026, 56, 1100–1105. https://doi.org/10.1007/s11430-025-1848-7.

Li, W., Zhang, J., Xie, J., Xia, Y., He, Y., 2023. Application of the wavelet transform and INPEFA in sequence stratigraphy. ACS Omega 8, 3441–3451.

Liner, C., Li, C.-F., Gersztenkorn, A., Smythe, J., 2004. SPICE: A new general seismic attribute. In: 72nd Annual International Meeting, SEG Expanded Abstracts, pp. 433–436.

Marshall, N., Morley, R.J., Petronotis, K.E., Backe, G., Holmes, N.A., 2017. Milankovitch cycles in an equatorial delta from the Miocene of Borneo. Earth Planet. Sci. Lett. 472, 229–240. https://doi.org/10.1016/j.epsl.2017.04.015.

McKenzie, D., 1978. Some remarks on the development of sedimentary basins. Earth Planet. Sci. Lett. 40 (1), 25–32. https://doi.org/10.1016/0012-821X(78)90071-7.

Meyers, S.R., 2019. Cyclostratigraphy and the problem of astrochronologic testing. Earth-Sci. Rev. 190, 190–223. https://doi.org/10.1016/j.earscirev.2018.11.015.

Meyers, S.R., Sageman, B.B., Hinnov, L.A., 2001. Integrated quantitative stratigraphy of the Cenomanian-Turonian Bridge Creek Limestone Member using evolutive harmonic analysis and stratigraphic modeling. J. Sediment. Res. 71 (4), 628–644. https://doi.org/10.1306/012401710628.

Meyers, S.R., Sageman, B.B., 2004. Detection, quantification, and significance of hiatuses in pelagic and hemipelagic strata. Earth Planet. Sci. Lett. 224 (1–2), 55–72. https://doi.org/10.1016/j.epsl.2004.05.003.

Meyers, S.R., Sageman, B.B., 2007. Quantification of deep-time orbital forcing by average spectral misfit. Am. J. Sci. 307 (5), 773–792. https://doi.org/10.2475/05.2007.01.

Mitsui, T., Ditlevsen, P., Boers, N., Crucifix, M., 2025. 100 kyr ice age cycles as a timescale-matching problem. Earth Syst. Dynam. 16, 1569–1584. https://doi.org/10.5194/esd-16-1569-2025.

Mutti, E., Carminatti, M., 2012. Deep-water sands of the Brazilian Offshore Basins. In: Search and Discovery Article #30219, 42 pp.

Nainggolan, H.B., Winardhi, S., 2019. Geophysical approach to improve well correlation and stratigraphy package in the frontier area: example case of Upper Jurassic Fm. Semai Basin, Eastern Indonesia. Earth and Environmental Science 311, 012054. Newman, P.A., Coy, L., Pawson, S., Lait, L.R., 2016. QBO anomaly. *Geophys. Res. Lett.* 43, 8791–8797. https://doi.org/10.1088/1755-1315/311/1/012054.

Nio, S.D., Brouwer, J., Smith, D., De, J.M., Bohm, A., 2005. Spectral trend attribut analysis: Applications in the stratigraphic analysis of wireline logs. First Break 23 (4), 71–75. https://doi.org/10.3997/1365-2397.23.4.26503

Nobes, D.C., Bloomer, S.F., Mienert, J., Westall, F., 1991. Milankovitch cycles and nonlinear response in the Quaternary record in the Atlantic sector of the South oceans. Proceedings ODP, Scientic Results, Vol. 114, pp. 551-576.

Okada, H. and Bukry, D., 1980. Supplementary modification and introduction of code numbers to the low-latitude coccolith biostratigraphic zonation (Bukry, 1973; 1975). Marine Micropaleontology, 5, pp.321–325.

Pandolpho, B.T., Klein, A.H., Dutra, I., Mahiques, M.M., Viana, A.R., Bueno, G.V., Machado, A.A., Camargo, Y.L., Hercos, C.M., Lima, Y., Filho, A.F., Theodoro, C.E., 2021. Seismic record of a cyclic turbidite-contourite system in the Northern Campos Basin, SE Brazil. Mar. Geol. 434, 106422 https://doi.org/10.1016/j.margeo.2021.106422.

Qayyum, F., Smith, D., 2014. Integrated sequence stratigraphy using trend logs and densely mapped seismic data. First Break 32. https://doi.org/10.3997/1365-2397.32.12.78856.

Qayyum, F., Betzler, C., Catuneanu, O., 2017. The Wheeler diagram, flattening theory, and time. Marine and Petroleum Geology 86, 1417–1430. https://doi.org/10.1016/j.marpetgeo.2017.07.034.

Rial, J.A., Anaclerio, C.A., 2000. Understanding nonlinear responses of the climate system to orbital forcing. Quat. Sci. Rev. 19 (17–18), 1709–1722. https://doi.org/10.1016/S0277-3791(00)00087-1.

Royden, L., Keen, C.E., 1980. Rifting process and thermal evolution of the continental margin of eastern Canada determined from subsidence curves. Earth Planet. Sci. Lett. 51, 343 – 361. https://doi.org/10.1016/0012-821X(80)90216-2.

Santos, B.N., Rodrigues, C.C., Franco, D.R., Li, M., Fernandes, M.A., Candido, M., Rocha, R.M., Santos, T.P., Gasperi, A., Fragoso, D.G.C., Fazio, G., Rodrigues, A.N.G., 2023. Integration of seismic stratigraphy and cyclostratigraphy for high resolution chronostratigraphic correlation: the Albacora Field, Campos Basin, Brazil. Marine and Petroleum Geology 158, 106541. https://doi.org/10.1016/j.marpetgeo.2023.106541.

Sinnesael, M., De Vleeschouwer, D., Zeeden, C., Batenburg, S.J., Da Silva, A.-C., de Winter, N.J., Dinarès-Turell, J., Drury, A.J., Gambacorta, G., Hilgen, F.J., Hinnov, L.A., Hudson, A.J.L., Kemp, D.B., Lantink, M.L., Laurin, J., Li, M., Liebrand, D., Ma, C., Meyers, S.R., Monkenbusch, J., Montanari, A., Nohl, T., Pälike, H., Pas, D., Ruhl, M., Thibault, N., Vahlenkamp, M., Valero, L., Wouters, S., Wu, H., Claeys, P., 2019. The Cyclostratigraphy Intercomparison Project (CIP): consistency, merits and pitfalls. Earth Sci. Rev. 199, 102965. https://doi.org/10.1016/j.earscirev.2019.102965.

Stark, T.J., 2003. Unwrapping instantaneous phase to generate a relative geologic time volume. In: 73rd SEG Annual International Meeting Expanded Abstracts, pp. 1707–1710.

Stark, T.J., 2004. Relative geologic time (age) volumes - relating every seismic sample to a geologically reasonable horizon. Lead. Edge 23, 928–932. https://doi.org/10.1190/1.1803505.

Stark, Tracy J., 2005a. Generation of a 3d seismic “wheeler diagram” from a high resolution age volume. In: SEG Technical Program Expanded Abstracts 2005. Society of Exploration Geophysicists, pp. 782–785. https://doi.org/10.1190/1.2148275.

Stark, T. J., 2005b. System for multi-dimensional data analysis. Google Patents. (US Patent 6,850,845).

Stark, T.J., 2006. Visualization techniques for enhancing stratigraphic inferences from 3D seismic data volumes. First Break 24, 75–85. https://doi.org/10.3997/1365-2397.24.1094.26926

Thomson, D.J., 1982. Spectrum estimation and harmonic analysis. Proc. IEEE 70, 1055–1096.

Vail, P.R., Mitchum, R.M., Thompson, S.I., 1977. Seismic Stratigraphy and Global Changes of Sea Level: Part 4. Global Cycles of Relative Changes of Sea Level Vol. 165, pp. 83–97. https://doi.org/10.1306/M26490C6.

Widess, M.B., 1973. How thin is a thin bed? Geophysics 38 (6), 1176–1180. https://doi.org/10.1190/1.1440403.

Winter, W.R., Jahnert, R.J., França, A.B., 2007. Bacia de Campos. Bol. Geociencias Petrobras 15, 511–529.

Wu, H., Zhang, S., Jiang, G., Huang, Q., 2009. The floating astronomical time scale for the terrestrial Late Cretaceous Qingshankou Formation from the Songliao Basin of Northeast China and its stratigraphic and paleoclimate implications. Earth Planet. Sci. Lett. 10, 308–323. https://doi.org/10.1016/j.epsl.2008.12.016.

Wu, H., Zhang, S., Hinnov, L.A., Jiang, G., Feng, Q., Li, H., Yang, T., 2013. Time-calibrated Milankovitch cycles for the late Permian. Nat. Commun. 4, 2452. https://doi.org/10.1038/ncomms3452.

SUPPLEMENTARY MATERIAL

ARCHITECTURE-DRIVEN ORBITAL RECORDS IN A CONTINENTAL MARGIN: CYCLOSTRATIGRAPHIC–SEISMIC INSIGHTS FROM THE MIOCENE ALBACORA OILFIELD (CAMPOS BASIN, BRAZIL)

Mariana Aragão Fernandes*, Natália Braun dos Santos, Daniel Ribeiro Franco, Ciro Climaco Rodrigues, Mateus Fontana Michelon, Mingsong Li, Daniel Galvão Carnier Fragoso, Paulo Sérgio Gomes Paim, Mariane Candido, Carolina Gonçalves Leandro, Gabriella Fazio, Raysa de Magalhães Rocha, Lucio Riogi Tokutake, Ana Natalia Gomes Rodrigues

*Corresponding author.

E-mail address: marianafernandes@on.br

This section includes:

Methods supplementary texts.

Text S1: INPEFA implementation and script

S1.1 Software, packages, and reproducibility

All INPEFA analyses were conducted in Python 3 (v.3.13.x) within a Jupyter Notebook environment. The workflow is based on the open-source PyNPEFA package (https://github.com/daeIy/PyNPEFA), with minor adaptations related to data input procedures and detrending settings. The analysis requires the following packages: numpy (van der Walt et al., 2011), pandas (McKinney, 2010), scipy (Virtanen et al., 2020), matplotlib (Hunter, 2007), statsmodels (Seabold and Perktold, 2010), spectrum (Cokelaer, 2017), and cvxopt (Andersen et al., 2013). The complete annotated notebook can be obtained from the corresponding author upon request.

S1.2 Annotated Python script

For transparency and reproducibility, the full script is provided below. The path variables (diretorio, arquivo) correspond to the authors' local directory structure and should be modified by users according to their own environment. Well names and file identifiers have been removed from the reproduced script.

```
# # INPEFA
# From: "https://github.com/daeIy/PyNPEFA" with small modifications

%matplotlib inline
```

```
import matplotlib.pyplot as plt
import numpy as np
import pandas as pd
from scipy import signal as sig
from cvxopt import matrix
from spectrum.burg import _arburg2
import statsmodels.api as sm

############ INPUT PARAMETERS ###############
filtersize_meter=10                #size of the model filter (model prediction) in meters.
default=10
filename='1RJS297_802-3059.txt'   #data file (txt file with 2 columns separated by a blank
space)
dg = pd.read_table(filename,sep='\s+',header=None)

header_profundidade='DEPT'
header_GR='HGR'
dg.columns = [header_profundidade, header_GR]
dg

############ FUNCTION DEFINITIONS ###########
def INPEFA(df,ordem):
   dg = pd.DataFrame([np.array(df['GR'])],columns=[df['MD']])  #reorganize data to fit in
"matrix" shape below
   y= dg.iloc[0]                                #reorganize data to fit in "matrix" shape below

   y=matrix(y)
   bffy = _arburg2(y,ordem)[0].real
   pffy = sig.convolve(y, np.reshape(bffy,(len(bffy), 1)),  mode='same')   # PEFA
   iipfy = np.cumsum(pffy[::-1])[::-1]     # INPEFA
   ipfy = iipfy / max(abs(iipfy))         # Normalized to -1 <= INPEFA <= 1
   ipfy = np.roll(ipfy, int(ordem/2))      # to set curves at the correct detph
   return ipfy
```

```
def filtersize_sample(df,filtersize_meter):  #Filter order calculation
   first_row_value =df['MD'].iloc[0]
   last_row_value= df['MD'].iloc[-1]
   amostragem = (last_row_value-first_row_value)/(len(df)-1)
   ordem = int(filtersize_meter / amostragem )
   return ordem

df = dg[[header_profundidade,header_GR]]
df = df.set_axis(['MD', 'GR'], axis=1, inplace=False)
filtersize=filtersize_sample(df,filtersize_meter)

x=np.array(df['MD'])
original = np.array(df['GR'])

################ INPEFA calculation from original data (no detrending) ############
inpefa_original = INPEFA(df,filtersize)

############### INPEFA calculation from mean-detrended data and displays the plots
#############

coefficients = np.polyfit(x, original, 0)
media_model = np.poly1d(coefficients)
media_trend = media_model(x)

media_detrended = original - media_trend


dk = pd.DataFrame(data=media_detrended,columns=['GR'])
dk['MD']=df['MD']
inpefa_dmedia = INPEFA(dk,filtersize)

#*****************************

%matplotlib inline
plt.figure(figsize=(10,4.5), facecolor='w', edgecolor='k')
```

```
plt.subplot(141)
plt.plot(original,-x,label='original')
plt.plot(media_trend,-x,label='average trend')
plt.grid(True)
plt.minorticks_on()
plt.legend()
plt.title('GR original')

plt.subplot(142)
plt.plot(media_trend,-x)
plt.grid(True)
plt.minorticks_on()
plt.title('average trend')

plt.subplot(143)
plt.plot(media_detrended,-x)
plt.grid(True)
plt.minorticks_on()
plt.title('average detrended')

plt.subplot(144)
plt.plot(inpefa_dmedia,-x)
plt.grid(True)
plt.minorticks_on()
plt.title('inpefa dmedia')

plt.subplots_adjust(wspace=0.5, hspace=0.5)

plt.show()

############### INPEFA calculation from linearly detrended data and displays the plots
##############

coefficients = np.polyfit(x, original, 1)
```

```
linear_model = np.poly1d(coefficients)
linear_trend = linear_model(x)

linear_detrended = original - linear_trend


dk = pd.DataFrame(data=linear_detrended,columns=['GR'])
dk['MD']=df['MD']
inpefa_dlinear = INPEFA(dk,filtersize)

#*****************************

%matplotlib inline
plt.figure(figsize=(10,4.5), facecolor='w', edgecolor='k')

plt.subplot(141)
plt.plot(original,-x,label='original')
plt.plot(linear_trend,-x,label='linear trend')
plt.grid(True)
plt.minorticks_on()
plt.legend()
plt.title('GR original')

plt.subplot(142)
plt.plot(linear_trend,-x)
plt.grid(True)
plt.minorticks_on()
plt.title('linear trend')

plt.subplot(143)
plt.plot(linear_detrended,-x)
plt.grid(True)
plt.minorticks_on()
plt.title('linear detrended')
```

```
plt.subplot(144)
plt.plot(inpefa_dlinear,-x)
plt.grid(True)
plt.minorticks_on()
plt.title('inpefa dlinear')

plt.subplots_adjust(wspace=0.5, hspace=0.5)

plt.show()

############### INPEFA calculation from LOWESS (35%) detrended data and displays the
plots #############

lowess = sm.nonparametric.lowess
lowess_trend = lowess(original, x, frac=0.35,it=0)
lowess_detrended=original-lowess_trend[:,1]

dl = pd.DataFrame(data=lowess_detrended,columns=['GR'])
dl['MD']=df['MD']

inpefa_dlowess_35pc = INPEFA(dl,filtersize)

#####################################################
%matplotlib inline
plt.figure(figsize=(10,4.5), facecolor='w', edgecolor='k')

plt.subplot(141)
plt.plot(original,-x,label='original')
plt.plot(lowess_trend[:,1],-x,label='loewss trend')
plt.grid(True)
plt.minorticks_on()
plt.legend()
plt.title('GR original')

plt.subplot(142)
```

```
plt.plot(lowess_trend[:,1],-x)
plt.grid(True)
plt.minorticks_on()
plt.title('lowess trend 35%')

plt.subplot(143)
plt.plot(lowess_detrended,-x)
plt.grid(True)
plt.minorticks_on()
plt.title('lowess detrended 35%')

plt.subplot(144)
plt.plot(inpefa_dlowess_35pc,-x)
plt.grid(True)
plt.minorticks_on()
plt.title('inpefa dlowess 35%')

plt.subplots_adjust(wspace=0.5, hspace=0.5)

plt.show()

############### INPEFA calculation from LOWESS (5%) detrended data and displays the plots
##############
lowess = sm.nonparametric.lowess
lowess_trend = lowess(original, x, frac=0.05,it=0)
lowess_detrended=original-lowess_trend[:,1]

dl = pd.DataFrame(data=lowess_detrended,columns=['GR'])
dl['MD']=df['MD']

inpefa_dlowess_5pc = INPEFA(dl,filtersize)

##############################################3
%matplotlib inline
plt.figure(figsize=(10,4.5), facecolor='w', edgecolor='k')
```

```
plt.subplot(141)
plt.plot(original,-x,label='original')
plt.plot(lowess_trend[:,1],-x,label='loewss trend')
plt.grid(True)
plt.minorticks_on()
plt.legend()
plt.title('GR original')

plt.subplot(142)
plt.plot(lowess_trend[:,1],-x)
plt.grid(True)
plt.minorticks_on()
plt.title('lowess trend 5%')

plt.subplot(143)
plt.plot(lowess_detrended,-x)
plt.grid(True)
plt.minorticks_on()
plt.title('lowess detrended 5%')

plt.subplot(144)
plt.plot(inpefa_dlowess_5pc,-x)
plt.grid(True)
plt.minorticks_on()
plt.title('inpefa dlowess 5%')

plt.subplots_adjust(wspace=0.5, hspace=0.5)

plt.show()

############### Displays plots of INPEFA curves generated from input data using different
detrending methods ##############

%matplotlib inline
```

```
plt.figure(figsize=(10,4.5), facecolor='w', edgecolor='k')

plt.subplot(161)
plt.plot(original,-x,label='original')
plt.grid(True)
plt.minorticks_on()
plt.legend()
plt.title('GR original')

plt.subplot(162)
plt.plot(inpefa_original,-x)
plt.grid(True)
plt.minorticks_on()
plt.title('IPF original')

plt.subplot(163)
plt.plot(inpefa_dmedia,-x)
plt.grid(True)
plt.minorticks_on()
plt.title('IPF dmedia')

plt.subplot(164)
plt.plot(inpefa_dlinear,-x)
plt.grid(True)
plt.minorticks_on()
plt.title('IPF dlinear')

plt.subplot(165)
plt.plot(inpefa_dlowess_35pc,-x)
plt.grid(True)
plt.minorticks_on()
plt.title('IPF dlowess 35%')

plt.subplot(166)
plt.plot(inpefa_dlowess_5pc,-x)
```

```
plt.grid(True)
plt.minorticks_on()
plt.title('IPF dlowess 5%')

plt.subplots_adjust(wspace=0.5, hspace=0.5)

plt.savefig(diretorio+'3CRT4_inpefa.pdf', format='pdf')

plt.show()
```

Chapter 7

Concluding Remarks

This study applies an integrated framework combining cyclostratigraphy and seismic stratigraphy to investigate the evolution of Miocene deposits in the Albacora Oilfield, Campos Basin, Brazil, building upon the work of Santos *et al.* (2023). The incorporation of newly available high-resolution seismic data, additional well-logs, and complementary analytical tools, including INPEFA and the RGT model, enabled the expansion of the investigated area to approximately 62 km² and provided improved constraints on depositional system evolution and its associated chronostratigraphic framework.

MTM spectral analysis identified statistically robust peaks, generally above the 95-99% confidence levels, with frequency ratios that closely correspond to the expected astronomical periodicities for ~14 Ma (405:125:40.6:23.5:18.8 ≈ 21.5:6.6:5.0:2.2:1.2:1.0). Analysis of sediment accumulation rates indicated values ranging from 30.0 cm/kyr to 45.4 cm/kyr, consistent with the findings of Santos *et al.* (2023) and previous studies in the Albacora Oilfield. These results support the interpretation of spectral bands associated with orbital forcing and indicate a clear orbital control on sedimentation across the six analyzed well-logs.

Seismic stratigraphic analysis, supported by the RGT model, indicates a predominantly progradational stacking pattern, with enhanced preservation concentrated in the mid-slope domain. This is evidenced by the greater number of long-eccentricity cycles recorded in mid-slope deposits relative to shelf and more basinward settings. This revised interpretation substantially updates the temporal framework proposed by Santos *et al.* (2023), suggesting an increase of more than 1.6 Myr in the estimated total depositional duration. The results demonstrate that reliable estimates of depositional timescales depend on multi-well correlations focused on intervals with higher stratigraphic preservation.

Key stratigraphic surfaces were identified by the integration of cyclostratigraphy, seismic stratigraphy, the RGT model, and INPEFA and are recognized by the attenuation or loss of long-eccentricity cyclicity, as evidenced by EHA, inflections in INPEFA curves, and their correspondence with mapped seismic horizons. These surfaces are fundamental for understanding the evolution of depositional systems, as they are associated with depositional hiatuses and/or erosional events.

Progressive thickness increase southwards in seismic data suggests variations in

sedimentation rates between the northern and southern sectors of the study area, which are not expressed by cyclostratigraphic analyses (COCO and eCOCO) or by variations in orbital cycle thickness. In addition, a pronounced increase in RMS amplitude within the RGT framework, particularly in the interval associated with SR4 in the southern sector, suggests enhanced sediment supply in this portion of the basin.

A clear understanding of depositional architecture and stratigraphic completeness is fundamental for the effectiveness of cyclostratigraphy as a powerful tool for high-resolution geological time reconstruction. For robust interpretations of astronomical signals, the integration of multi-well datasets with seismic data is important to properly constrain depositional patterns. The study further demonstrates that isolated well-log records are insufficient for evaluating stratigraphic completeness, as they may only capture part of the depositional stacking history, including progradational, retrogradational, and aggradational trends. Furthermore, the integration of cyclostratigraphy and seismic stratigraphy reinforces the possibility of defining isochronous surfaces at orbital resolution, highlighting how both methodologies provide complementary information for the analysis of the depositional record and the refinement of geological time.

Chapter 8

References

ANP (Brazilian National Agency of Petroleum, Natural Gas and Biofuels), 2018. *Albacora*. Available at: https://www.gov.br/anp/pt-br/assuntos/exploracao-e-producao-de-oleo-e-gas/desenvolvimento-e-producao/pd/albacora.pdf.

Bastos, G., Bastos, I.P., 2017. *Bacia de Campos: Sumário geológico e setores em oferta*. ANP, Rio de Janeiro. Available at: https://www.gov.br/anp/pt-br/rodadas-anp/rodadas-concluidas/concessao-de-blocos-exploratorios/14a-rodada-licitacoes-blocos/arquivos/areas-oferta/sumario-campos.pdf.

Agnini, C., Monechi, S., Raffi, I., 2017. Calcareous nannofossil biostratigraphy: historical background and application in Cenozoic chronostratigraphy. *Lethaia* 50 (3), 447-463.

Almeida, A.G., Kowsmann, R.O., 2014. Geomorfologia do talude continental e do Platô de São Paulo. In: Kowsmann, R.O. (Ed.), *Geologia e Geomorfologia*. Elsevier, Rio de Janeiro, Habitats, v. 1, pp. 33-66.

Azevedo, R.L. (Coord.), Shimabukuro, S., Arai, M., Uesugui, N., Telles, A.S., 1992. Bacia de Campos. In: Beurlen, G. (Coord., Ed.), Richter, A.J., Cunha, A.S., Telles, A.S., Martinis, E., Pedrao, E., Moura, J.A., Gomide, J., Viviers, M.E., Arai, M., Uesugui, N., Nascimento, N.L. do, Azevedo, R.L., Dino, R., Antunes, R.L., Shimabukuro, S., Abreu, W.S. de (Eds.), *Bioestratigrafia das Bacias Mesozoicas-Cenozoicas Brasileiras. Texto Explicativo das Cartas Bioestratigraficas, Volume I: Bacias de Pelotas a Sergipe-Alagoas*. PETROBRAS/CENPES/SUPEP/DIVEX/SEBIPE, Relatório Interno, pp. 79-137.

Backman, J., Raffi, I., Rio, D., Fornaciari, E., Pälike, H., 2012. Biozonation and biochronology of Miocene through Pleistocene calcareous nannofossils from low and middle latitudes. *Newsletters on Stratigraphy* 45 (3), 221-244.

Bashir, Y., Zahari, M.A.A.B., Karaman, A., Doğan, D., Döner, Z., Mohammadi, A., Ali, S.H., 2024a. Artificial intelligence and 3D subsurface interpretation for bright spot and channel detections. *AIMS Geosciences* 10 (4), 662-683.

Bashir, Y., Siddiqui, N.A., Morib, D.L., Babasafari, A.A., Ali, S.H., Imran, Q.S., Karaman, A., 2024b. Cohesive approach for determining porosity and P-impedance in carbonate rocks using seismic attributes and inversion analysis. *Journal of Petroleum Exploration and Production Technology* 14 (5), 1173-1187.

Batiston, D.A., Antunes, R.L., Dias-Brito, D., 2016. Nanofósseis calcários e a bioestratigrafia do oligoceno-plioceno da margem continental brasileira. *Geociências* 35 (3), 359-371.

Berger, A., 1977a. Long-term variations of the earth's orbital elements. *Celestial Mechanics* 15 (1), 53-74.

Berger, A.L., 1977b. Support for the astronomical theory of climatic change. *Nature* 269 (5623), 44-45.

Berger, A., 1979. Spectrum of climatic variations and their causal mechanisms. *Geophysical Surveys* 3 (4), 351-402.

Berger, A., 1980. The Milankovitch astronomical theory of paleoclimates: a modern review. *Vistas in Astronomy* 24, 103-122.

Berger, A., Loutre, M.F., Laskar, J., 1992. Stability of the astronomical frequencies over the Earth's history for paleoclimate studies. *Science* 255, 560-566.

Berger, A., Loutre, M.F., Tricot, C., 1993. Insolation and Earth's orbital periods. *Journal of Geophysical Research: Atmospheres* 98 (D6), 10341-10362.

Berger, A., Loutre, M.F., 1994. Astronomical forcing through geologic time. In: de Boer, P.L., Smith, D.G. (Eds.), *Orbital Forcing and Cyclic Sequences*. IAS Special Publication 19, pp. 15-24.

Berger, A., Loutre, M.F., 2004. Astronomical theory of climate change. *Journal de Physique IV (Proceedings)* 121, 1-35.

Berger, A., 2012. A brief history of the astronomical theories of paleoclimates. In: *Climate Change: Inferences from Paleoclimate and Regional Aspects*. Springer Vienna, Vienna, pp. 107-129.

Bolli, H.M., Saunders, J.B., Perch-Nielsen, K. (Eds.), 1989. *Plankton Stratigraphy: Volume 1, Planktic Foraminifera, Calcareous Nannofossils and Calpionellids*. CUP Archive, Cambridge.

Borges, R.G., Lima, A.C. de, Kowsmann, R.O., 2015. ÁREAS PROPENSAS A ESCORREGAMENTOS NO TALUDE CONTINENTAL. In: *Geologia e Geomorfologia*. Campos, pp. 99-136.

Bown, P.R., Young, J.R., 1998. Introduction. In: Bown, P.R. (Ed.), *Calcareous Nannofossil Biostratigraphy*. British Micropalaeontology Society Series, Chapman & Hall, London, pp. 1-15.

Bramlette, M.N., Wilcoxon, J.A., 1967. Middle Tertiary calcareous nannoplankton of the Cipero section, Trinidad, WI. *Tulane Studies in Geology and Paleontology* 5 (3).

Castro, A.H.A., 2005. Estudo de ciclicidade orbital com base em dados sísmicos - exemplo para o Mioceno da Bacia de Campos. *Revista Brasileira de Geociências* 35, 139-151

Castro, D.D., 1993. Morfologia da margem continental sudeste-sul e estratigrafia sísmica do sopé continental. *Anuário do Instituto de Geociências* 16, 141-141.

Castro, R.D., Picolini, J.P., 2015. Principais aspectos da geologia regional da Bacia de Habitats, v. 1, pp. 1-12.Campos. In: Kowsmann, R.O. (Ed.), *Geologia e Geomorfologia*. Elsevier, Rio de Janeiro, Habitats, v. 1, pp. 1-12.

Chen, Q., Sidney, S., 1997. Advances in seismic attribute technology. *SEG Technical Program Expanded Abstracts 1997*. Society of Exploration Geophysicists, pp. 730-733.

Crucifix, M., Loutre, M.F., Berger, A., 2006. The climate response to the astronomical forcing. *Space Science Reviews* 125 (1-4), 213-226.

De Gasperi, A. and Catuneanu, O., 2014. Sequence stratigraphy of the Eocene turbidite reservoirs in Albacora field, Campos Basin, offshore Brazil. *AAPG Bulletin* 98 (2), 279-313.

Delworth, T.L. and Mann, M.E., 2000. Observed and simulated multidecadal variability in the Northern Hemisphere. *Climate Dynamics* 16 (9), 661-676.

Dias, J.L., Scarton, J.C., Esteves, F.R., Carminatti, M. and Guardado, L.R., 1990. Aspectos da evolução tectono-sedimentar e a ocorrência de hidrocarbonetos na Bacia de Campos. In: *Origem e evolução de bacias sedimentares*. Rio de Janeiro: PETROBRÁS, 2, 333-360.

Dinarès-Turell, J., Westerhold, T., Pujalte, V., Röhl, U. and Kroon, D., 2014. Astronomical calibration of the Danian stage (Early Paleocene) revisited: Settling chronologies of sedimentary records across the Atlantic and Pacific Oceans. *Earth and Planetary Science Letters* 405, 119-131.

Ernesto, M. and Pacca, I.G., 1981. Spectral analysis of Permocarboniferous geomagnetic variation data from glacial rhythmites. *Geophysical Journal International* 67 (3), 641-647.

Figueiredo Jr., A.G., Pacheco, C.E.P., Vasconcelos, S.C. and Silva, F.T., 2014. Geomorfologia e sedimentologia da plataforma continental. In: Kowsmann, R.O. (ed.), *Geologia e Geomorfologia*. Rio de Janeiro: Elsevier. Habitats, v. 1, pp. 13-32.

Figueiredo Jr., A.G., Pacheco, C.E.P., de Vasconcelos, S.C., da Silva, F.T., 2015. Geomorfologia e sedimentologia da plataforma continental. In: *Geologia e Geomorfologia*. Campos, pp. 13-32.

Fragoso, D.G.C., Kuchenbecker, M., Magalhães, A.J.C., Scherer, C.M.D.S., Gabaglia, G.P.R. and Strasser, A., 2022. Cyclicity in Earth sciences, quo vadis? Essay on cycle concepts in geological thinking and their historical influence on stratigraphic practices. *History of Geo- and Space Sciences* 13 (1), 39-69.

Franco, D.R., 2007. *Magnetoestratigrafia e análise espectral de ritmitos permocarboníferos da Bacia do Paraná: influências dos ciclos orbitais no regime deposicional*. Doctoral dissertation, Universidade de São Paulo.

Geng, Z., Wu, X., Shi, Y. and Fomel, S., 2020. Deep learning for relative geologic time and seismic horizons. *Geophysics* 85 (4), WA87-WA100.

Gilbert, G.K., 1895. Sedimentary measurement of Cretaceous time. *The Journal of Geology* 3 (2), 121-127.

Gong, Z., 2021. Cyclostratigraphy of the Cryogenian Fiq Formation, Oman and its implications for the age of the Marinoan glaciation. *Global and Planetary Change* 204, 103584.

Gradstein, F.M., Ogg, J.G., Schmitz, M.D. and Ogg, G.M., 2018. *Geologic Time Scale 2020*.

Guardado, L.R., Peres, W.E. and Souza Cruz, C.E., 1986. Depositional model and seismic expression of turbidites in Campos Basin, offshore Brazil. *American Association of Petroleum Geologists Bulletin* 70, 597 (abstract).

Guardado, L.R., Gamboa, L.A.P., Lucchesi, C.F., 1989. Petroleum geology of the Campos Basin, Brazil, a model for a producing Atlantic-type basin. In: Edwards, J.D., Santogrossi, P.A. (Eds.), Divergent/Passive Margin Basins: AAPG Memoir 48. AAPG, Tulsa, Oklahoma, USA, pp. 3-79.1.

Hilgen, F., Schwarzacher, W. and Strasser, A., 2004. Concept and Definitions in Cyclostratigraphy (Second Report of the Cyclostratigraphy Working Group): International Subcommission on Stratigraphic Nomenclature of the IUGS Commission on Stratigraphy.

Hilgen, F.J., Hinnov, L.A., Abdul Aziz, H., Abels, H.A., Batenburg, S., Bosmans, J.H.C., de Boer, B., Hüsing, S.K., Kuiper, K.F., Lourens, L.J., Rivera, T., Tuenter, E., Van de Wal, R.S.W., Wotzlaw, J.-F. and Zeeden, C., 2015. Stratigraphic continuity and fragmentary sedimentation: the success of cyclostratigraphy as part of integrated stratigraphy. *Geological Society, London, Special Publications* 404 (1), 157-197.

Hinnov, L.A., 2013. Cyclostratigraphy and its revolutionizing applications in the earth and planetary sciences. *Geological Society of America Bulletin* 125 (11-12), 1703-1734.

Hinnov, L.A., 2018. Cyclostratigraphy and astrochronology in 2018. In: *Stratigraphy & Timescales*, Vol. 3, pp. 1-80. Academic Press.

Hinnov, L.A., 2000. New perspectives on orbitally forced stratigraphy. *Annual Review of Earth and Planetary Sciences* 28 (1), 419-475.

Hinnov, L.A. and Hilgen, F.J., 2012. Cyclostratigraphy and Astrochronology. In: *The Geological Time Scale*, pp. 63-83.

Huang, H., Gao, Y., Jones, M.M., Tao, H., Carroll, A.R., Ibarra, D.E., Wu, H. and Wang, C., 2020. Astronomical forcing of Middle Permian terrestrial climate recorded in a large paleolake in northwestern China. *Palaeogeography, Palaeoclimatology, Palaeoecology* 550, 109735.

Kodama, K.P. and Hinnov, L., 2015. *Rock Magnetic Cyclostratigraphy*. Wiley-Blackwell, 166 p.

Kruiver, P.P., Dekkers, M.J. and Langereis, C.G., 2000. Secular variation in Permian red beds from Dôme de Barrot, SE France. *Earth and Planetary Science Letters* 179 (1), 205-217.

Kushnir, Y., 1994. Interdecadal variations in North Atlantic sea surface temperature and associated atmospheric conditions. *Journal of Climate* 7 (1), 141-157.

Laskar, J., 2008. Chaotic diffusion in the Solar System. *Icarus* 196 (1), 1-15.

Laskar, J., Fienga, A., Gastineau, M. and Manche, H., 2011. La2010: a new orbital solution for the long-term motion of the Earth. *Astronomy & Astrophysics* 532.

Li, M., Kump, L.R., Hinnov, L.A. and Mann, M.E., 2018. Tracking variable sedimentation rates and astronomical forcing in Phanerozoic paleoclimate proxy series with evolutionary correlation coefficients and hypothesis testing. *Earth and Planetary Science Letters* 501, 165-179.

Li, M., Huang, C., Ogg, J., Zhang, Y., Hinnov, L.A., Wu, H., Chen, Z.Q. and Zou, Z., 2019a. Paleoclimate proxies for cyclostratigraphy: comparative analysis using a Lower Triassic marine section in South China. *Earth-Science Reviews* 189, 125-146.

Li, M., Hinnov, L. and Kump, L., 2019b. Acycle: Time-series analysis software for paleoclimate research and education. *Computers & Geosciences* 127, 12-22. ISSN 0098-3004.

Linhares, O.A.G., Stohler, R.C., Correa, S.N., Ida, M. and Coelho, F.M., 2018. Otimização da estratégia de drenagem com base no mapeamento sísmico de barreiras hidráulicas relacionadas à elementos arquiteturais em um campo da Bacia de Campos. In: *Anais do 49º Congresso Brasileiro de Geologia*.

Lisiecki, L.E., 2010. Links between eccentricity forcing and the 100,000-year glacial cycle. *Nature Geoscience* 3 (5), 349-352.

Li, W., Zhang, J., Xie, J., Xia, Y. and He, Y., 2023. Application of the wavelet transform and INPEFA in sequence stratigraphy. *ACS Omega* 8 (3), 3441-3451.

Luna Osorio, J.S. (2017). *3D Geological Modeling of the Oligocene-Miocene Turbidite System in the Eastern Marlim Oilfield, Campos Basin, Brazil = Modelagem Geológica 3D do Sistema Turbidítico Oligoceno-Mioceno no Campo Marlim Leste, Bacia de Campos, Brasil*. PhD thesis, Universidade Estadual de Campinas (UNICAMP), Campinas.

Liner, C., Li, C.-F., Gersztenkorn, A. and Smythe, J., 2004. SPICE: A new general seismic attribute. In: *72nd Annual International Meeting, SEG, Expanded Abstracts*, pp. 433-436.

Mantua, N.J. and Hare, S.R., 2002. The Pacific decadal oscillation. *Journal of Oceanography* 58 (1), 35-44.

McKenzie, D., 1978. Some remarks on the development of sedimentary basins. *Earth and Planetary Science Letters* 40 (1), 25-32.

Meyers, S.R., Sageman, B.B. and Hinnov, L.A., 2001. Integrated quantitative stratigraphy of the Cenomanian-Turonian Bridge Creek Limestone Member using evolutive harmonic analysis and stratigraphic modeling. *Journal of Sedimentary Research* 71 (4), 628-644.

Meyers, S.R., 2019. Cyclostratigraphy and the problem of astrochronologic testing. *Earth-Science Reviews* 190, 190-223.

Mitchell, J.M., 1976. An overview of climatic variability and its causal mechanisms. *Quaternary Research* 6 (4), 481-493.

North American Commission on Stratigraphic Nomenclature, 2005. North American stratigraphic code. *AAPG Bulletin* 89 (11), 1547-1591.

Nainggolan, H.B. and Winardhi, S., 2019. Geophysical approach to improve well correlation and stratigraphy package in the frontier area: example case of Upper Jurassic Fm. Semai Basin, Eastern Indonesia. In: *IOP Conference Series: Earth and Environmental Science* 311 (1), 012054. IOP Publishing.

Newman, P.A., Coy, L., Pawson, S. and Lait, L.R., 2016. The anomalous change in the QBO in 2015-2016. *Geophysical Research Letters* 43 (16), 8791-8797.

Nio, S.D., Brouwer, J.H., Smith, D., de Jong, M. and Böhm, A.R., 2005. Spectral trend attribute analysis: applications in the stratigraphic analysis of wireline logs. *First Break* 23 (4).

Okada, H. and Bukry, D., 1980. Supplementary modification and introduction of code numbers to the low-latitude coccolith biostratigraphic zonation (Bukry, 1973; 1975). *Marine Micropaleontology* 5, 321-325.

Paillard, D., 2001. Glacial cycles: toward a new paradigm. *Reviews of Geophysics* 39 (3), 325-346.

Pearson, P.N., 1998. Evolutionary concepts in biostratigraphy. In: *Unlocking the Stratigraphic Record*, pp. 123-144.

Petersen, S.V., Schrag, D.P. and Clark, P.U., 2013. A new mechanism for Dansgaard-Oeschger cycles. *Paleoceanography* 28 (1), 24-30.

Philander, S.G.H., 1990. *El Niño, La Niña, and the Southern Oscillation*. Academic Press, London, 289 pp.

Pisias, N.G., Dauphin, J.P. and Sancetta, C., 1973. Spectral analysis of late Pleistocene-Holocene sediments. *Quaternary Research* 3 (1), 3-9.

Qayyum, F. and Smith, D., 2014. Integrated sequence stratigraphy using trend logs and densely mapped seismic data. *First Break* 32 (12).

Qayyum, F., Betzler, C. and Catuneanu, O., 2017. The Wheeler diagram, flattening theory, and time. *Marine and Petroleum Geology* 86, 1417-1430.

Royden, L. and Keen, C.E., 1980. Rifting process and thermal evolution of the continental margin of eastern Canada determined from subsidence curves. *Earth and Planetary Science Letters* 51 (2), 343-361.

Ruddiman, W.F., 2001. *Earth's Climate: Past and Future*. W.H. Freeman and Company, New York, NY, 465 pp.

Santos, B.N., Rodrigues, C.C., Franco, D.R., Li, M., Fernandes, M.A., Candido, M., Rocha, R.M., Santos, T.P., Gasperi, A., Fragoso, D.G.C., Fazio, G. and Rodrigues, A.N.G., 2023. Integration of seismic stratigraphy and cyclostratigraphy for high resolution chronostratigraphic correlation: the Albacora Field, Campos Basin, Brazil. *Marine and Petroleum Geology* 158, 106541.

Schlesinger, M.E. and Ramankutty, N., 1994. An oscillation in the global climate system of period 65-70 years. *Nature* 367 (6465), 723-726.

Schreiner, S., Souza, M.B.F.M., Robalo, J. and Figueiredo Jr., A.G., 2016. Bathymetric map of the Campos Basin. In: *Geology and Geomorphology*, pp. 67-70.

Schwarzacher, W., 1975. *Sedimentation Models and Quantitative Stratigraphy*, Vol. 19. Elsevier.

Schwarzacher, W., 1993. *Cyclostratigraphy and the Milankovitch Theory*. Elsevier.

Sinito, A.M., Valencio, D.A., Ernesto, M. and Pacca, I.G., 1981. Palaeomagnetic study of Permocarboniferous glacial varves from the Itararé Subgroup, southern Brazil. *Geophysical Journal International* 67 (3), 635-640.

Souza Cruz, C.E., Barrocos, S.L.S., Appi, C.J., 1987. Modelo deposicional dos reservatórios turbidíticos oligocênicos/eomiocênicos do Campo de Albacora, Bacia de Campos, Brasil. *Boletim de Geociências da Petrobras* 1 (2), 215-223.

Stark, T.J., 2003. Unwrapping instantaneous phase to generate a relative geologic time volume. In: *73rd SEG Annual International Meeting Expanded Abstracts*, pp. 1707-1710.

Stark, T.J., 2004. Relative geologic time (age) volumes - relating every seismic sample to a geologically reasonable horizon. *The Leading Edge* 23, 928-932.

Stark, T.J., 2005a. Generation of a 3D seismic "Wheeler diagram" from a high resolution age volume. In: *SEG Technical Program Expanded Abstracts 2005*. Society of Exploration Geophysicists, pp. 782-785.

Stark, T.J., 2005b. *System for multi-dimensional data analysis*. Google Patents (US Patent 6,850,845).

Stark, T.J., 2006. Visualization techniques for enhancing stratigraphic inferences from 3D seismic data volumes. *First Break* 24, 75-85.

Strasser, A., Hilgen, F.J. and Heckel, P.H., 2006. Cyclostratigraphy-concepts, definitions, and applications. *Newsletters on Stratigraphy* 42 (2), 75-114.

Thomson, D.J., 1982. Spectrum estimation and harmonic analysis. *Proceedings of the IEEE* 70, 1055-1096.

Ting, M., Kushnir, Y., Seager, R. and Li, C., 2011. Robust features of Atlantic multi-decadal variability and its climate impacts. *Geophysical Research Letters* 38 (17).

Vail, P.R., Mitchum Jr., R.M. and Thompson III, S., 1977. Seismic Stratigraphy and global changes of sea-level. In: Clayton, C.E. (ed.), *Seismic Stratigraphy Applications to Hydrocarbon Exploration*. Tulsa, Okla: AAPG, pp. 83-97 (AAPG Memoir 26).

von der Heydt, A.S., Ashwin, P., Camp, C.D., Crucifix, M., Dijkstra, H.A., Ditlevsen, P. and Lenton, T.M., 2021. Quantification and interpretation of the climate variability record. *Global and Planetary Change* 197, 103399.

Wallace, J.M., 1973. General circulation of the tropical lower stratosphere. *Reviews of Geophysics* 11 (2), 191-222.

Weedon, G.P., 2003. *Time-series Analysis and Cyclostratigraphy: Examining Stratigraphic Records of Environmental Cycles*. Cambridge University Press.

Widess, M.B., 1973. How thin is a thin bed? *Geophysics* 38 (6), 1176-1180.

Winter, W.R., Jahnert, R.J. and França, A.B., 2007. Bacia de Campos. *Boletim de Geociências da PETROBRAS* 15 (2), 511-529.

Wu, H., Zhang, S., Jiang, G. and Huang, Q., 2009. The floating astronomical time scale for the terrestrial Late Cretaceous Qingshankou Formation from the Songliao Basin of Northeast China

and its stratigraphic and paleoclimate implications. *Earth and Planetary Science Letters* 278 (3-4), 308-323.

Wu, H., Zhang, S., Feng, Q., Jiang, G., Li, H. and Yang, T., 2012. Milankovitch and sub-Milankovitch cycles of the early Triassic Daye Formation, South China and their geochronological and paleoclimatic implications. *Gondwana Research* 22 (2), 748-759.

Wu, H., Zhang, S., Hinnov, L.A., Jiang,G., Feng, Q., Li, H. and Yang, T., 2013. Time-calibrated Milankovitch cycles for the late Permian. *Nature Communications* 4 (1), 1-8.

Yuan, R., Zhu, R., Qu, J., Wu, J., You, X., Sun, Y. and Zhou, Y., 2018. Utilizing Integrated Prediction Error Filter Analysis (INPEFA) to divide base-level cycle of fan-deltas: a case study of the Triassic Baikouquan Formation in Mabei slope area, Mahu Depression, Junggar Basin, China. *Open Geosciences* 10 (1), 79-86.

Zachos, J., Pagani, M., Sloan, L., Thomas, E. and Billups, K., 2001. Trends, rhythms, and aberrations in global climate 65 Ma to present. *Science* 292 (5517), 686-693.

Zembruscki, S.G., 1979. Geomorfologia da margem continental sul brasileira e das bacias oceânicas adjacentes. In: Chaves, H.A.F. (ed.), *Geomorfologia da margem continental brasileira e das áreas oceânicas adjacentes: relatório final*. Rio de Janeiro: Petrobras, Cenpes, Dintep. Série Projeto REMAC 7, pp. 129-177.